Check for updates

The route for applied interfacial solar vapor generation: fundamental principles, device design, and practical application

Bowen Liu, Yawei Yang, [iD] * Qi Zhao, Yihong Liu, Yuyao Shen, Yong Ma and Wenxiu Que*

Interfacial solar vapor generation (ISVG) has emerged as a promising technology for sustainable water purification, desalination, and source extraction under solar energy. In fact, the underlying scientific principles and fundamental physical processes governing ISVG remain inadequately understood. In this review, we aim to provide a comprehensive and in-depth exploration of the scientific mechanisms and physical principles behind ISVG technology, including strategies to optimize mass and energy transfer, vapor generation and diffusion, as well as anti-fouling techniques. Furthermore, we systematically summarize the advancements and engineering applications of ISVG technologies, offering practical guidelines for their implementation in real-world scenarios. This review seeks to bridge the gap between fundamental science and engineering practice, providing insights to accelerate the development of efficient and scalable ISVG systems.

Broader context

Interfacial solar vapor generation (ISVG) has emerged as a sustainable and energy-efficient approach for water purification and salt extraction, offering a promising alternative to conventional desalination technologies. However, the fundamental physical processes governing ISVG efficiency remain poorly understood, limiting its scalability and practical deployment. This review timely elucidates that gap by systematically analyzing the key physical mechanisms—mass and energy transfer, interfacial heat management, and anti-fouling design—essential to advancing ISVG performance. By connecting fundamental science with engineering design, it offers a unified framework that can guide the development of robust, high-efficiency ISVG devices. These insights are critical for accelerating ISVG adoption in real-world applications, contributing to global efforts in clean water production and sustainable energy conversion.

Electronic Materials Research Laboratory, Key Laboratory of the Ministry of Education, International Center for Dielectric Research, Shaanxi Engineering Research Center of Advanced Energy Materials and Devices, School of Electronic Science and Engineering, Xi'an Jiaotong University, Xi'an 710049, P. R. China. E-mail: ywyang@xjtu.edu.cn, wxque@xjtu.edu.cn

Bowen Liu is currently a PhD candidate under the supervision of Prof. Wenxiu Que and Dr Yawei Yang at Xi'an Jiaotong University. He received his BS and MS degrees at North China Electric Power University. His present research interests focus on the interfacial solar desalination and lithium ion extraction.

Bowen Liu

Yawei Yang is an Associate Professor at Xi'an Jiaotong University. He received his PhD degree at Xi'an Jiaotong University in 2019. He worked as a visiting scholar at Emory University under the supervision of Prof. Tianquan Tim Lian from 2017 to 2019. His present research interests focus on semiconductor materials and their ultrafast spectroscopy dynamics for solar energy conversion, including photocatalysis and solar desalination.

Yawei Yang

1. Introduction

Water scarcity, driven by drought, over-extraction, and climate change, is currently impacting nearly 20% of the global population.[1–6] Water scarcity, exacerbated by drought, over-extraction, and climate change, currently affects nearly 20% of the global population.[7–9] Desalination of seawater and brackish groundwater is a key strategy to augment water supplies while minimizing the impact on freshwater ecosystems. However, nearly all desalination plants (99%) rely on fossil fuels for energy production, leading to significant carbon emissions.[10] If this trend continues, carbon dioxide (CO_2) emissions from desalination processes could reach 400 million tons annually by 2050.[11] In response, interfacial solar vapor generation (ISVG) has emerged as a sustainable and energy-efficient alternative, utilizing solar energy to achieve high evaporation rates with minimal environmental impact.[12–14]

While ISVG has gained substantial attention for its potential, existing reviews have predominantly focused on material advancements,[15–17] device architectures,[18–23] and optimization strategies.[24–27] In 2019, Hu's group first highlighted recent developments in photothermal materials and their photothermal conversion mechanisms, which are central to the technology's performance.[28] Yu's group provided a comprehensive summary of the material design principles for solar evaporation, emphasizing the relationship between material properties and evaporation efficiency.[29] More recently, Yamauchi and co-workers made significant contributions by uncovering the mechanism of water activation during solar evaporation, a discovery that reshapes our understanding of energy dynamics in the process.[30] Building on this, Xu and co-workers expanded the scope to include the development of ISVG technology, along with key design principles aimed at enhancing solar evaporation rates and energy conversion efficiency.[31] Zhu and co-workers discussed various promising applications of solar evaporation, demonstrating its versatility across different scenarios.[32] Furthermore, Xu's team focused on the industrial design of desalination systems, introducing hybrid-driven solutions to overcome limitations related to weather, salt accumulation, and system response time. Despite these advancements, a comprehensive understanding of the underlying scientific mechanisms and physical processes governing ISVG remains limited.[33]

The process of solar vapor generation is inherently complex, involving an interplay of solar irradiation absorption,[34–37] heat transfer,[38–40] and vapor diffusion.[41,42] These processes are influenced by factors such as thermal conductivity,[43,44] localized heat management,[24,45–47] and water transport pathways.[48–50] Challenges such as energy losses from thermal resistance and the accumulation of salts and biofouling can undermine the long-term stability and energy efficiency (*i.e.* solar-to-water conversion efficiency) of ISVG systems.[51–53] Although advances in photothermal materials and device designs have contributed to performance improvements,[54–60] much of the research has been carried out without fully elucidating the fundamental physical processes that drive ISVG performance.[61–64] To unlock the full potential of ISVG, a deeper understanding of these coupled mechanisms is crucial for optimizing energy efficiency and system stability.

In this review, we first provide a comprehensive analysis of the fundamental scientific principles and physical processes underlying ISVG. We examine key aspects such as mass and energy transport optimization, vapor generation enhancement, and the development of anti-fouling strategies through innovative materials and system designs. Additionally, we also present a summary of recent technological advancements and engineering applications, offering insights into the practical implementation and scalability of ISVG systems (Fig. 1). By bridging the gap between fundamental science and engineering, this review aims to establish a robust framework for accelerating the development of ISVG systems, ultimately addressing critical challenges in water scarcity and energy sustainability.

2. Fundamentals of mass and energy transfer for increased ISVG system efficiency

To significantly improve the energy efficiency of ISVG systems, it is essential to optimize both mass and energy transport mechanisms. This section delves into the core aspects of enhancing solar irradiation absorption, managing heat effectively, optimizing water and salt transportation and improving vapor generation and diffusion. Each of these elements is critical for maximizing the performance and sustainability of ISVG systems (Fig. 2). We first elucidate the fundamental physical processes of mass and energy transport, followed by an exploration of the underlying scientific principles. By comprehensively considering and optimizing these factors, the overall energy efficiency of ISVG systems can be significantly enhanced, providing effective solutions for addressing water scarcity and improving energy utilization.

2.1 Phase transition mechanism

The phase transition of water from liquid to vapor involves complex heat and mass transfer processes at the interface,

Wenxiu Que is currently a full professor at Xi'an Jiaotong University. He received his PhD degree at Xi'an Jiaotong University in 1995. He worked as a post-doctoral fellow at the National University of Singapore from 1996 to 1998, and was then employed as a research scientist at Nanyang Technological University in Singapore from 1998 to 2005. His present research interests focus on nanocomposites materials for energy conversion and storage application, including electrocatalysis, supercapacitors, perovskite solar cells, photocatalysis, and solar desalination.
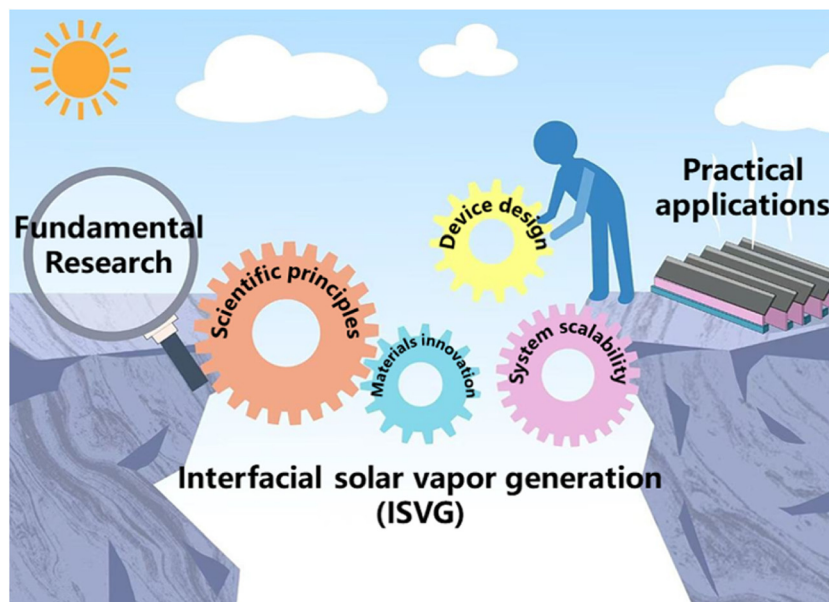
Wenxiu Que

This journal is © The Royal Society of Chemistry 2025

Energy Environ. Sci., 2025, **18**, 6366–6437 | **6367**

Fig. 1 Pathway of ISVG technology: From fundamental research to practical applications.
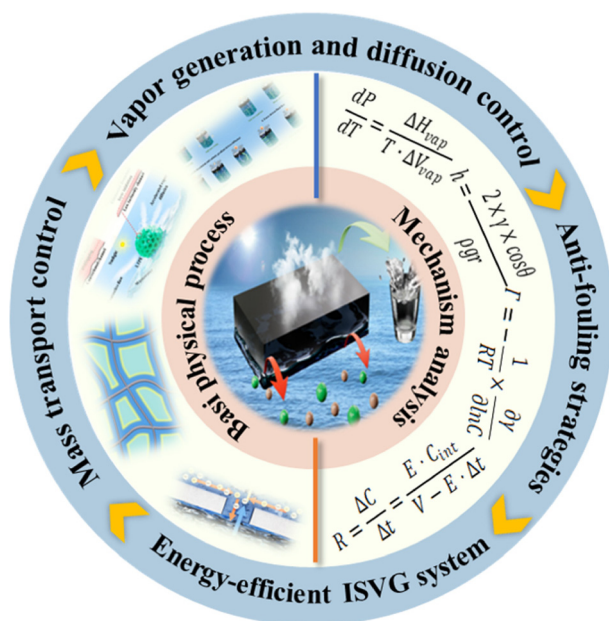

Fig. 2 Schematic diagram of improving the energy efficiency of ISVG systems through mass/energy transportation optimization.

where energy is converted into vaporization and molecular diffusion. These processes govern the efficiency of evaporation by dictating the rate of energy input, the transport of vapor away from the interface, and the interactions between thermal and mass fluxes. In this section, we present a detailed examination of the thermodynamic and transport mechanisms underlying phase transitions, with a focus on how manipulating these factors can optimize evaporation efficiency. This foundational understanding serves as the basis for developing advanced evaporation systems with improved performance.

Water's unique molecular structure imparts crucial properties related to phase transitions and energy transfer, which are vital in both natural and engineered systems. The fundamental principles of the liquid-to-vapor phase transition describing the changes in internal energy, entropy, and volume during evaporation using the Gibbs free energy equations (eqn (1) and (2)). The latent heat and entropy variations during this process are key to optimizing evaporation efficiency. In subsequent sections, we will explore in detail how reducing the latent heat can enhance evaporation rates.

$$\Delta G = \Delta H_{vap} - T\Delta S_{vap} \tag{1}$$

where ΔG represents the change in free energy, ΔH is the latent heat of evaporation, ΔS is the change in entropy during evaporation, and T is the absolute temperature. At phase equilibrium, $\Delta G = 0$, which leads to the following relationship:

$$\Delta H_{vap} = T\Delta S_{vap} \tag{2}$$

This equation indicates a direct connection between the latent heat, temperature, and entropy change during the phase transition. By measuring the latent heat of evaporation, the entropy change of the system at different temperatures can be determined, which is crucial for optimizing the evaporation process. To better illustrate this energy transfer process during phase transition, Fig. 3 depicts how solar irradiation at the interface leads to the generation of both sensible and latent heat, which drives water vapor generation. Specifically, solar energy absorbed at the interface generates both sensible and latent heat. Sensible heat increases the liquid temperature, while latent heat drives the phase transition from liquid to vapor. A portion of the absorbed energy is utilized for vapor generation, while some is lost as heat to the surroundings. The efficiency of this process is determined by two key factors: the
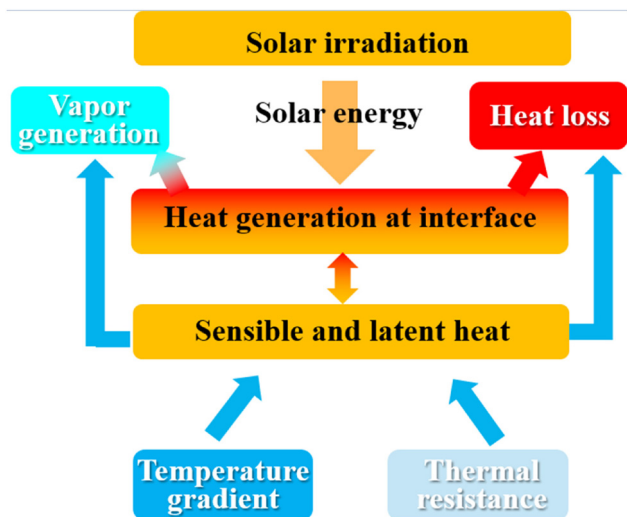
6368 | *Energy Environ. Sci.*, 2025, **18**, 6366–6437

This journal is © The Royal Society of Chemistry 2025

Fig. 3 Fundamental principles behind phase transition and the energy/mass transfer process.

temperature gradient, which enhances heat transfer toward the interface, and thermal resistance, which impedes heat flow and increases energy loss. Optimizing these factors is critical for maximizing vapor generation efficiency and minimizing heat dissipation, providing a foundation for designing advanced water evaporation systems. In section 2.4.2, we will discuss in detail how to enhance the water evaporation rate by reducing the latent heat of evaporation.

2.2 Framework of energy efficiency in ISVG systems

In order to comprehensively assess the performance of ISVG systems, it is crucial to evaluate the key efficiency metrics across several stages of energy transformation and utilization. Notably, a meaningful evaluation of energy efficiency in ISVG systems must be grounded in the overall solar-to-water efficiency, which encapsulates both the solar-to-vapor conversion and the subsequent vapor-to-water condensation processes. This comprehensive metric is essential for capturing the full thermodynamic pathway from solar input to freshwater output. This framework provides a detailed approach to analyzing ISVG systems, starting from the solar-to-vapor conversion efficiency, followed by thermal utilization efficiency, and culminating in the evaluation of condensate water yield. Each of these stages offers unique insights into how energy is converted and utilized, and provides a basis for improving the system's overall efficiency. Meanwhile, key metrics for evaluating energy efficiency in ISVG systems will also be outlined in advance within this section. A more in-depth analysis of these sub-processes will be presented in the following sections.

2.2.1 Key metrics for evaluating energy efficiency in ISVG systems

Latent heat of evaporation (h_{fg}). Latent heat of evaporation (h_{fg}) is a fundamental thermodynamic property that quantifies the amount of energy required to vaporize a given mass of water.[65] Accurate characterization of evaporation efficiency

requires careful consideration of this property, particularly when dealing with systems that have enhanced evaporation surfaces, such as interfacial solar evaporators. As demonstrated in a recent study,[62] the typical approach of using dark environment evaporation tests to infer reduced vaporization enthalpy may lead to misleading results. The assumption of equal energy input, which is common in these tests, does not hold for systems with enlarged evaporation areas due to the resulting temperature differences between the evaporator and the surrounding environment. Meanwhile, many existing reports suffer from systematic overestimation of performance due to unaccounted convective heat flows, recessed liquid levels, and unstated thermal gradients, leading to flawed interpretations of latent heat reduction. However, Chen's group showed that this perceived reduction often stems from experimental artifacts, such as water surfaces recessed below the container lip, which introduce additional mass transfer resistance and distort baseline rates.[66] This discrepancy, in turn, impacts the accuracy of the calculated vaporization enthalpy. We therefore recommend that differential scanning calorimetry (DSC) be used to measure the latent heat of evaporation, as this method provides more accurate results by accounting for these temperature variations and environmental energy inputs. This ensures that enthalpy measurements reflect true energy requirements rather than overestimating evaporation efficiencies caused by energy discrepancies. The relationship governing the evaporation process can be expressed as follows:

$$q_{\text{evap}} = \dot{m} h_{\text{fg}} \tag{3}$$

where q_{evap} is the rate of heat transfer to the system due to evaporation (W), $\dot{m}$ is the mass evaporation rate (kg s^{-1}), and h_{fg} is the latent heat of evaporation (J kg^{-1}). This equation provides a direct link between energy input and evaporation efficiency, ensuring that results are comparable across different experimental setups.

Effective light-exposed evaporation surface area. The solar-exposed evaporation area (A_{evap}) is another critical parameter that influences the overall energy efficiency of ISVG systems. The evaporation rate is directly proportional to the area exposed to solar radiation, and modern systems often utilize porous structures that significantly increase the effective surface area for evaporation due to capillary effects and the meniscus curvature within pores. The increase in surface area results in enhanced evaporation without changing the intrinsic vaporization enthalpy of water. To accurately quantify this parameter, we propose the use of radiometric instruments (*e.g.*, pyranometers or solar radiometers) to measure the solar radiation intensity on the evaporation surface. The following expression can be used to calculate the evaporation rate based on absorbed solar energy:

$$\dot{m} = \frac{I_{\text{sol}} \cdot A_{\text{evap}}}{h_{\text{fg}}} \tag{4}$$

where I_{sol} is the solar radiation intensity (W m^{-2}), and A_{evap} is the effective evaporation surface area (m^2). This metric enables

researchers to account for differences in system designs and environmental conditions by standardizing the way in which evaporation surface areas are measured.

2.2.2 Solar-to-vapor conversion efficiency analysis. Typically, solar-to-vapor conversion efficiency (η) is defined as the ratio of the thermal energy contained in the steam to the total solar energy absorbed. This efficiency can be represented mathematically by the following equation:

$$\eta = \frac{m \cdot h_{lv}}{C_{opt} \cdot q_0} \qquad (5)$$

where m represents the mass flux of water evaporated by solar irradiation, normalized to unit area and time; h_{lv} denotes the total enthalpy of vaporization, which encompasses both sensible and latent heat in ISVG systems. The optical concentration of sunlight is represented by C_{opt} while q_0 refers to the solar power incident per unit area, commonly accepted as 1 kW m^{-2}. However, achieving high solar-to-vapor conversion efficiency alone does not guarantee optimal system performance, as it only reflects the final outcome of evaporation. A critical intermediate factor influencing this efficiency is how effectively the absorbed solar energy is retained and utilized within the system before vapor generation occurs. In practical ISVG operations, a portion of the absorbed solar energy is inevitably dissipated through various loss pathways, including conduction, convection, and thermal radiation. Therefore, a thorough assessment of thermal utilization efficiency is essential for understanding how much of the absorbed heat is actually converted into useful thermal energy that drives the phase transition. Specifically, thermal energy is subject to inevitable losses through conduction (Q_{cond}), convection (Q_{conv}), and radiation (Q_{rad}) (detailed analysis in section 2.3.3). To quantify these losses, we define thermal utilization efficiency ($\eta_{thermal}$) as the ratio of useful heat utilized ($Q_{thermal}$) and the total absorbed heat in eqn (6) and (7). These equations quantify the proportion of thermal energy effectively used by the system and provides insight into the system's thermal management performance.

$$\eta_{thermal} = \frac{Q_{useful}}{Q_{thermal}} = 1 - \frac{Q_{loss}}{Q_{thermal}} \qquad (6)$$

$$Q_{loss} = Q_{thermal} - Q_{cond} - Q_{conv} - Q_{rad} \qquad (7)$$

2.2.3 Vapor-to-water condensation efficiency analysis. The ultimate goal of ISVG technology is to produce freshwater through evaporation and condensation (detailed analysis in section 2.4.4). The theoretical condensate water yield $m_{theoretical}$ is calculated based on the available useful heat and the latent heat of vaporization ΔH_{vap}. The latent heat ΔH_{vap} can be derived as:

$$\Delta H_{vap} = \int_{T_0}^{T_{evap}} Cp(T)dT + \Delta H_{latent} \qquad (8)$$

where $Cp(T)$ is the specific heat of water, and ΔH_{latent} is the latent heat of phase change. The theoretical condensate ($m_{theoretical}$) yield is then given by eqn (9). Meanwhile, the actual

condensate water yield $m_{condensed}$ represents the amount of freshwater produced, which is usually lower than the theoretical yield due to system inefficiencies. The efficiency of water generation η_{water} is defined as the ratio of actual condensate to the theoretical maximum in eqn (10). This ratio captures the system's performance in terms of actual water production relative to its theoretical potential.

$$m_{theoretical} = \frac{Q_{useful}}{\Delta H_{vap}} \qquad (9)$$

$$\eta_{water} = \frac{m_{condensed}}{m_{theoretical}} = \frac{m_{condensed} \times \Delta H_{vap}}{Q_{useful}} \qquad (10)$$

2.2.4 Comprehensive performance metric. To provide a holistic assessment of an ISVG system's performance, we can combine the solar-to-vapor conversion efficiency and vapor-to-water conversion efficiency into a single overall efficiency metric η_{total}:

$$\eta_{total} = \eta_{solar-to-vapor} \times \eta_{vapor-to-water} \qquad (11)$$

In summary, this comprehensive efficiency metric combines both the effective use of thermal energy and the water generation performance, offering a complete picture of the system's effectiveness in real-world applications. By optimizing η_{total}, we can identify areas for improving ISVG technology and enhance its potential for sustainable desalination and water purification applications. In fact, any reported evaporation efficiency that exceeds 100% without accounting for all thermal and optical losses violates fundamental energy conservation principles and should be considered methodologically flawed.[1] To some extent, the result of not scientifically or accurately considering the true evaporation enthalpy, the effective evaporation area, and the inclusion of non-contributory low-temperature evaporation areas.

2.3 Optimization of energy transfer

2.3.1 Energy transfer mechanism. Energy and heat transfer at the interface are primarily governed by heat conduction and latent heat exchange during phase changes. The efficiency of heat transfer is influenced by factors such as temperature gradients, interfacial thermal resistance, and the characteristics of evaporation. A temperature gradient is essential to drive heat transfer, while thermal resistance at material interfaces can significantly reduce efficiency. Solar energy is converted into latent heat, enabling water evaporation, but traditional models may fail at the nanoscale, where non-equilibrium thermodynamics become necessary. Specifically, in ISVG systems, the temperature gradient is a key factor driving heat transfer and evaporation. According to the heat conduction equation, the temperature gradient can be described by the following formula:

$$\frac{\partial T}{\partial x} = \frac{q}{k} \qquad (12)$$

where $\frac{\partial T}{\partial x}$ is the spatial temperature gradient (K m^{-1}), q is the heat flux per unit area (W m^{-2}), and k is the thermal conductivity

6370 | *Energy Environ. Sci.*, 2025, **18**, 6366–6437

This journal is © The Royal Society of Chemistry 2025

of the material (W m^{-1} K^{-1}). This equation indicates that heat transfer is directly proportional to the temperature gradient and the material's thermal conductivity. In ISVG systems, enhancing the temperature gradient is key to improving heat transfer efficiency. Through surface modifications or the use of nanostructures, the material can be engineered to have higher thermal conductivity, thus promoting a larger temperature differential across the system, which accelerates the evaporation of water. Such modifications ensure that the thermal energy provided by sunlight is effectively utilized, minimizing thermal losses and maximizing evaporation rates. Meanwhile, during the phase transition from liquid to vapor, the system undergoes a process that inherently generates entropy. The entropy change (ΔS) during evaporation is given by:

$$\Delta S = \frac{Q_{latent}}{T_{evap}} \tag{13}$$

where ΔS is the change in entropy (J K^{-1}), Q_{latent} is the latent heat of evaporation (J), representing the energy absorbed during the phase change, and T_{evap} is the temperature at which evaporation occurs (K). The second law of thermodynamics stipulates that any real process generates entropy, and in the case of ISVG, the irreversible energy conversion from heat to latent heat during evaporation results in entropy production. This process is particularly critical in the context of energy efficiency. Efficient ISVG systems aim to minimize entropy production to reduce waste heat and increase the fraction of energy utilized for the phase change. By enhancing the material properties and optimizing the system's design, entropy generation can be controlled, leading to improved thermodynamic efficiency and, consequently, a higher rate of evaporation for the given energy input. Furthermore, at the nanoscale, ISVG systems often operate under non-equilibrium conditions, where the classical description of heat transfer through Fourier's law becomes insufficient to describe the complexity of heat transport. Non-equilibrium heat transfer is particularly relevant at the liquid–vapor interface in ISVG systems, where sharp temperature gradients and high thermal fluxes prevail. Under such conditions, heat conduction is strongly coupled with molecular diffusion and convective transport. The Gibbs free energy equation can be employed to analyze the heat and mass transfer at the nanoscale:

$$dG = Vdp - SdT \tag{14}$$

where dG is the change in Gibbs free energy of the system (J); V is the system's volume (m^3); dp is the pressure differential (Pa); S is the entropy (J K^{-1}), and dT is the temperature change (K). This equation demonstrates how the system's energy state evolves due to changes in temperature and pressure, and highlights the non-equilibrium nature of processes such as evaporation. The coupling of thermal gradients with mass transport results in localized heating and cooling effects that influence the phase change rate and efficiency.

Additionally, interfacial heat transfer is also affected by molecular interactions and surface phenomena like surface tension. Effective heat management and minimizing heat loss are critical for improving evaporation efficiency. Section 2.3.3

will address these strategies in detail. In addition, temperature and concentration gradients at the interface significantly affect evaporation rates, with phenomena such as the Marangoni effect driving localized fluid motion and altering heat and mass transfer. Evaporation is governed not only by thermal conduction but also by vapor diffusion, making mass transfer behavior complex and dynamic. Optimizing these interfacial effects is essential for improving evaporation efficiency. Section 2.4.4 will discuss strategies to enhance vapor diffusion. Subsequently, to maximize interfacial evaporation efficiency, a deep understanding of thermodynamics and mass transfer mechanisms is required. Material selection is critical for improving energy absorption and thermal management at the interface. Additionally, designing interfaces to facilitate water molecule migration and rapid vapor diffusion is key. Finally, controlling salt deposition and biofouling is necessary to maintain efficient mass and heat transfer, which are central challenges in practical applications. These strategies are further elaborated in section 2.5.

2.3.2 Enhancing solar irradiation absorption.
Solar energy is a crucial source in the solar vapor generation process, where the evaporator converts absorbed solar energy into internal energy, raising its surface temperature. The surface temperature of the solar evaporator is a key factor influencing the liquid-to-gas phase transition properties of water. The vapor pressure of water increases with temperature due to the rise in kinetic energy of water molecules, allowing more molecules to overcome the surface tension of liquid water and escape into a gaseous state. This relationship is described by the Clausius–Clapeyron equation:

$$\frac{dP}{dT} = \frac{\Delta H_{vap}}{T \cdot \Delta V_{vap}} \tag{15}$$

where $\frac{dP}{dT}$ represents the rate of change of saturation vapor pressure with temperature; ΔH_{vap} represents the latent heat of the phase transition, specifically the heat required for water evaporation. T is the absolute temperature (K); ΔV_{vap} is the difference in specific volume between the gas and liquid phases per unit mass. As temperature rises, the vapor pressure of water also increases, facilitating the phase transition from liquid to gas. Therefore, it is vital to develop materials with excellent solar absorption performance. Wang and his group designed a 3D cup-shaped photothermal structure for the first time. The 3D cup photothermal structure utilizes its walls to recover energy lost through diffuse reflectance and thermal radiation from the 2D base, as shown in Fig. 4a. This design significantly enhances energy efficiency, achieving an exceptionally high vapor generation rate of 2.04 kg m^{-2} h^{-1} under one-sun illumination, thanks to the cup walls' ability to recapture diffuse reflectance.[67] This work has prompted further investigations into the use of 3D photothermal structures to address the energy efficiency constraints associated with 2D photothermal materials. In 2019, Fan et al. design an array of PPy origami structures with designed folding to manage optical absorption (Fig. 4b).[68] The rose-shaped origami structure effectively

This journal is © The Royal Society of Chemistry 2025

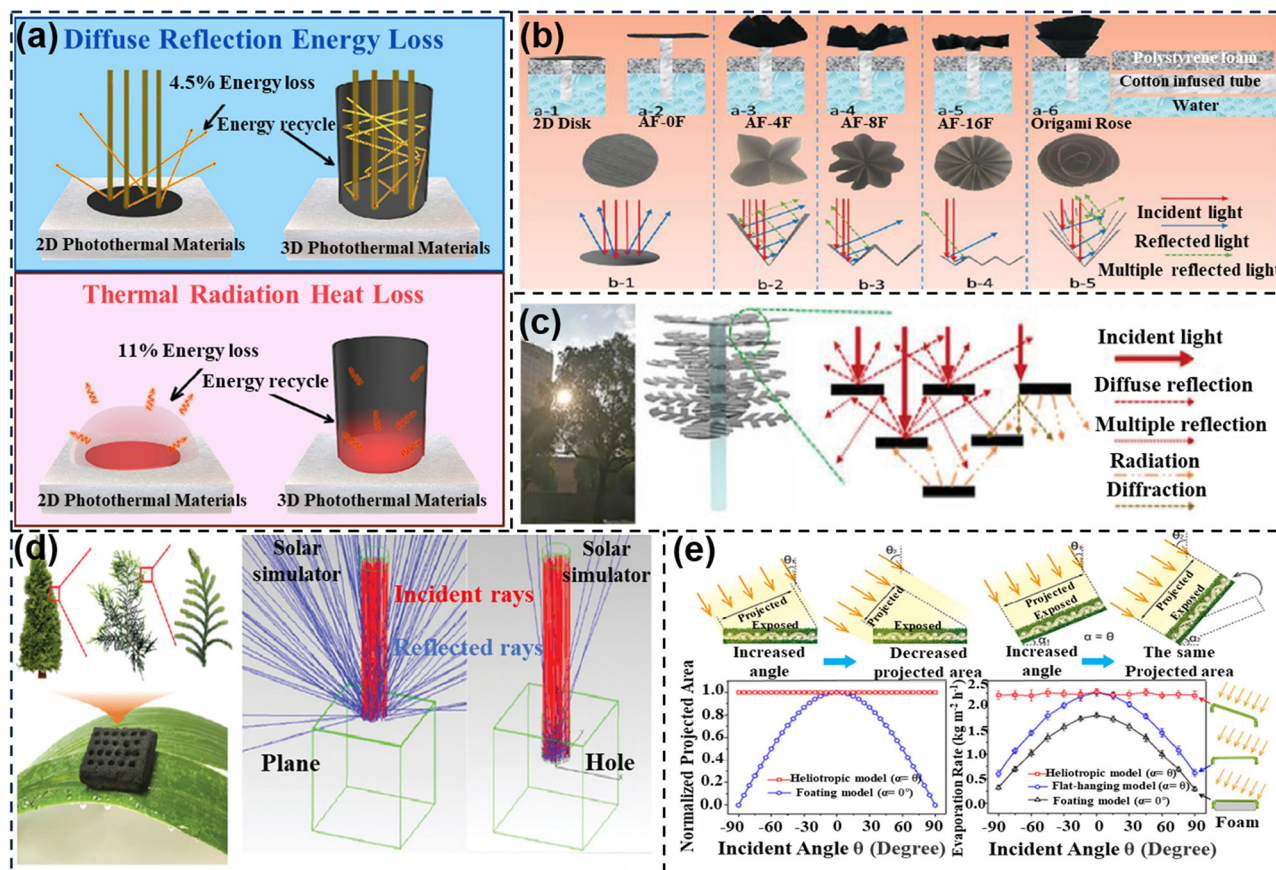Energy Environ. Sci., 2025, **18**, 6366–6437 | **6371**

Fig. 4 Strategies of solar-irradiation absorption enhancement in the ISVG process. (a) Schematic diagrams of the cup-walls shaped solar evaporator for recycling diffuse reflected light. Reprinted with permission.[67] Copyright 2018, Elsevier; (b) digital images of origami-structures based solar evaporator for capture of the irradiation reflection. Reprinted with permission.[68] Copyright 2019, Wiley-VCH; (c) schematic illustration of the multiple reflections, absorption, and diffraction of solar light at the artificial tree. Reprinted with permission.[69] Copyright 2020, Wiley-VCH; (d) schematic illustration of fractal structure for solar irradiation absorption. Reprinted with permission.[70] Copyright 2021, Wiley-VCH; (e) schematic illustrations of a sunflower-inspired evaporator for effective solar irradiation absorption. Reprinted with permission.[71] Copyright 2021, American Chemical Society.

captures incident light, enhancing solar energy utilization and achieving a water evaporation rate of 2.12 kg m^{-2} h^{-1} with 91.5% energy conversion efficiency under 1 sun irradiation. Similarly, drawing inspiration from the 3D hierarchical structure and leaf fenestration of Monstera and the intricate patterns of Chinese paper cutting, Du *et al.* developed a Monstera-inspired 3D artificial tree that demonstrates excellent ISVG performance (Fig. 4c).[69] The ultra-black leaves of these artificial trees effectively capture incident light through a series of reflections, diffractions, and thermal radiations between the leaves. The studies discussed above demonstrate that capturing solar irradiation effectively through multiple reflections and diffractions presents a promising approach. Besides, inspired by the aforementioned fractal structures and light absorption structures in nature, Li and co-workers presented a novel pomelo peel (PP)-derived solar-thermal material with simulation-informed biomimetic fractal designs for the first time (Fig. 4d).[70] The macroscopic hole patterns that allow for enhanced light trapping, which is capable of localizing more solar energy and converting to heat. In fact, most existing solar-to-vapor systems are static, with fixed optical and thermal

properties after fabrication. However, the angle and intensity of solar irradiation vary throughout the day and across seasons, creating a dynamic demand for adaptive performance. To address this issue, Chen and his group reported a sunflower-inspired hierarchical polyacrylonitrile copper sulfide (PAN@-CuS) fabric equipped in a heliotropic evaporation model (Fig. 4e).[71] In this model, the fabric adjusts its tilt angle (α) to stay perpendicular to the slanted sunlight, ensuring that the projected area matches the exposed surface area for optimal sunlight use. This design maintains efficiency under sunlight angles ranging from $-90°$ to $+90°$, the evaporation rate of the heliotropic model maintains stable (2.27 kg m^{-2} h^{-1}), while the conventional floating model shows a significant reduction in evaporation (83.9%). This study offers a strategy for maximizing solar energy utilization in the vapor generation process.

In fact, the effective evaporative surface area varies with changes in the angle of solar radiation. Conventional flat-structured evaporators have a limited operational time, lasting only a few hours each day due to their fixed orientation. Three-dimensional structures such as conical evaporators with larger surface areas offer greater practical value (practical engineering

application). However, real-time monitoring of the evaporation status is one of the challenges faced in the engineering application. Coupling interface evaporation systems with maximum power point tracking (MPPT) control technology commonly used in renewable energy systems, such as solar panels and wind turbines, is a promising approach. This integration not only enhances the overall operational efficiency of interface evaporation systems but also enables dynamic adaptation to changing environmental conditions, thereby optimizing energy conversion and water vapor generation. However, the coupling mechanisms need to be further explored, as currently, few studies focus on this aspect.

2.3.3 Heat management. In solar-driven interfacial evaporation, solar energy absorbed by the evaporator surface is converted into thermal energy, which drives vapor generation. Effective heat management is crucial for maximizing energy efficiency. Heat transfer at the liquid–vapor interface is controlled by conduction and latent heat exchange, both of which are influenced by temperature gradients and interfacial thermal resistance. Heat conduction at the interface is governed by Fourier's Law:

$$q_{\text{cond}} = -k\nabla T \tag{16}$$

where q_{cond} represents the heat flux, k is the thermal conductivity of the material, and ∇T is the temperature gradient. A steep temperature gradient facilitates efficient heat transfer from the liquid to vapor phase, providing the necessary energy for water molecules to overcome intermolecular forces.

The latent heat of vaporization is another key factor influencing phase transitions. The energy needed to convert water molecules from the liquid state to the vapor state is described by:

$$q_{\text{latent}} = m \cdot L \tag{17}$$

where q_{latent} is the total energy needed for vaporization, m is the mass of water evaporated, and L is the latent heat of vaporization (approximately 2260 kJ kg^{-1} for water). Reducing the latent heat through surface engineering, such as using hydrophilic materials, can lower the energy barrier for phase transition, improving the efficiency of the evaporation process. Meanwhile, interfacial thermal resistance, also known as Kapitza resistance, is a significant challenge that can hinder effective heat transfer across the liquid–vapor interface. This resistance arises due to differences in the thermal properties of water and solid surfaces, impeding the efficient conduction of heat. The thermal resistance is given by:

$$R_{\text{th}} = \frac{\Delta T}{q} \tag{18}$$

where R_{th} is the thermal resistance, ΔT is the temperature difference across the interface, and q is the heat flux. Reducing this interfacial thermal resistance is critical to improving heat transfer efficiency, particularly in nanostructured systems where the large surface-area-to-volume ratio amplifies the impact of thermal resistance. Surface modifications, such as using materials with closely matched thermal properties or nanostructure to increase heat transfer pathways, can help minimize thermal resistance.

In nanostructured systems or extreme conditions, classical thermodynamic models may fail. Non-equilibrium thermodynamics better captures heat transfer at the nanoscale, where localized temperature gradients and rapid phase changes dominate. The heat flux under non-equilibrium conditions is expressed as:

$$q_{\text{non-eq}} = \kappa\nabla T + \Pi \tag{19}$$

where κ represents the generalized thermal conductivity, and Π accounts for non-equilibrium effects. Appropriately accounting for these effects is crucial when utilizing nanostructures to enhance evaporation efficiency.

Additionally, in the broader context of ISVG systems, effective heat management strategies are essential to maximize energy utilization. Energy losses through radiation, convection, and conduction to the bulk water and the environment can reduce overall system efficiency. In general, radiation loss (Q_{rad}) occurs as heat is emitted from the evaporating surface to the cooler surrounding environment. Convection loss (Q_{conv}) refers to the heat transfer from the evaporator surface to the surrounding air, while conduction loss (Q_{cond}) describes the heat transferred downward into the bulk water. The losses due to radiation (Q_{rad}), convection (Q_{conv}) to the surrounding environment, and conduction (Q_{cond}) into the bulk water can be quantified using the equations outlined below:

$$Q_{\text{rad}} = \varepsilon A\sigma(T^4 - T_{\text{amb}}^4) \tag{20}$$

$$Q_{\text{conv}} = Ah(T - T_{\text{amb}}) \tag{21}$$

The variables in these equations include A, which represents the surface area of the solar absorber; α indicates the solar absorptance, ε is the emittance of the absorbing surface, σ stands for the Stefan–Boltzmann constant, h refers to the convection heat transfer coefficient, T is the temperature of the solar absorber, and T_{amb} is the ambient temperature. The heat loss to the underlying water combining conduction (Q_{cond}) and radiation ($Q_{\text{rad-water}}$) can be defined as:[72]

$$Q_{\text{cond}} + Q_{\text{rad-water}} = A\left(\frac{l}{k_{\text{insulation}}} + h_{\text{r-water}}^{-1}\right)(T - T_\infty) \tag{22}$$

where k_{foam} is the thermal conductivity of the foam, l is the thickness of the foam, and $h_{\text{r-water}}$ represents the linearized radiation heat transfer coefficient, which is generally low when radiating into water. Based on eqn (20)–(22), the net heat energy absorbed during the solar evaporation process can be defined as follows:[20]

$$m_{\text{eva}}h_{\text{fg}} = A\alpha q_{\text{solar}} - A\varepsilon\sigma(T^4 - T_\infty^4) - Ah(T - T_\infty) - Aq_{\text{water}} \tag{23}$$

where h_{fg} is the latent heat, q_{solar} is the solar flux, m_{eva} represents the net evaporation rate, and q_{water} represents the heat flux delivered to the water beneath, which consists of both conductive and radiative heat transfer. Based on the above equation, we will first introduce the recent developments of strategies for heat management (*i.e.* reduce or recycle the heat

This journal is © The Royal Society of Chemistry 2025

Energy Environ. Sci., 2025, **18**, 6366–6437 | **6373**

energy during the ISVG process), as well as discussing how to reduce the heat loss in this process.

In 2016, Chen's group developed a novel solar evaporator featuring a spectrally selective absorber, a bubble wrap insulation layer on top, and a polystyrene foam base. This design efficiently reduces radiation and convection losses to the surrounding air, while also minimizing conductive heat loss to the water beneath (Fig. 5a).[72] By maximizing solar absorption ($A\alpha q_{solar}$) through the use of spectrally selective materials and enhanced thermal localization, the system ensures efficient energy capture while minimizing reflection losses. Additionally, insulating layers and low-emissivity materials mitigate radiative heat loss, while the incorporation of thermal barriers suppresses both convective and conductive losses, maintaining high localized temperatures at the evaporation interface. This design ensures that the majority of the absorbed energy is directed toward meeting the latent heat of vaporization (h_{fg}), significantly enhancing the evaporation rate (m_{eva}). By strategically addressing and optimizing the terms in the equation, the floating structure achieves exceptional thermal efficiency, offering a robust model for future developments in solar-driven evaporation systems. Thus, high temperature can be achieved by using heat concentration and thermal localization, which both reduced heat losses from convection, conduction, and radiation. Additionally, an isothermal model was developed to assess the performance potential of a large-scale solar evaporator, assuming minimal heat loss from the sidewalls (Fig. 5b). This design featured repeated evaporation slots, creating an isothermal absorber. Experimental results indicated that the system could generate steam at 100 °C under ambient conditions, due to thermal concentration and heat localization that minimize losses from convection, conduction, and radiation. This affordable and scalable solar vapor generator shows considerable promise in broadening the range of applications and reducing the costs associated with solar thermal technologies. Inspired by the natural transpiration process in plants, Zhu's group created a 3D artificial transpiration device designed to minimize all three types of heat loss (Fig. 5c).[73] The device incorporates a 3D cone absorber with a 1D water path, effectively reducing radiation and convection losses to the surrounding air while minimizing conduction losses to the bulk water. This 3D structure limits conduction losses to the bulk water and enhances light absorption over a wide range of solar angles, thus optimizing the use of latent heat ($m_{eva}h_{fg}$). In an
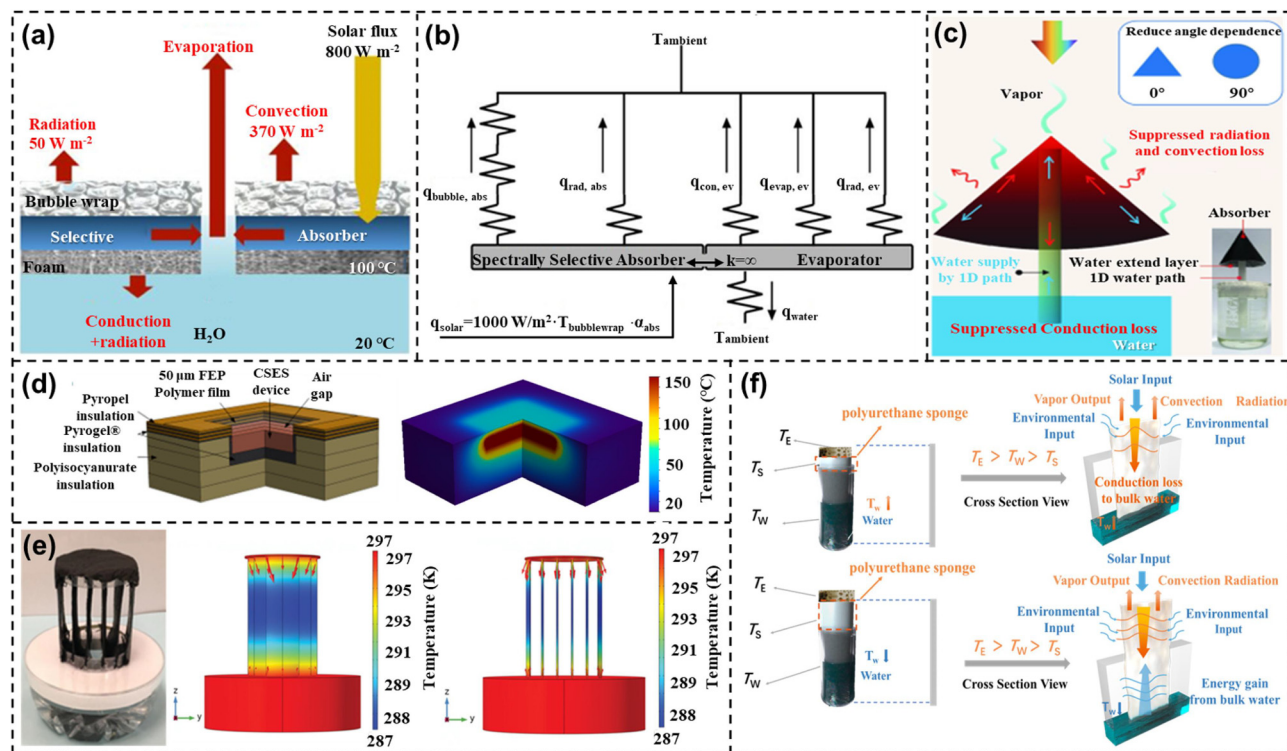

Fig. 5 Strategies of heat management in the ISVG process. (a) A solar evaporator featuring top and bottom insulation layers designed to minimize both downward conductive heat loss, and upward convective and radiative heat losses; (b) schematic representation of heat transfer in the ideal conduction model. (a) and (b) Reprinted with permission.[72] Copyright 2016, Springer Nature; (c) a typical 3D artificial transpiration evaporator effectively suppressed heat loss. The straight red arrows symbolize the direction of heat conduction, while the crooked red arrows depict both heat convection and radiation. Reprinted with permission.[73] Copyright 2017, Oxford University Press; (d) the thermal-separation based contactless solar evaporator eliminates the thermal leakage via both downward conduction loss and upward convection and radiation loss. Reprinted with permission.[74] Copyright 2018, Springer Nature; (e) a novel heatsink-like evaporator (HSE) fully eliminated the radiation, convection, and conduction heat losses. Reprinted with permission.[75] Copyright 2018, Wiley-VCH; (f) upcycled adsorbents-based evaporator to reduce heat conduction. Reprinted with permission.[76] Copyright 2018, Wiley-VCH.

improved design, a contactless solar evaporator was introduced by positioning the spectrally selective absorber away from the bulk water. The absorber captured incoming solar energy, converting it into heat, which was then re-emitted as thermal energy towards the water, exhibiting near-blackbody behavior at thermal wavelengths (Fig. 5d).[74] Due to its excellent infrared absorption characteristics, water effectively absorbed the emitted radiation within a thin sub-100 μm surface layer, allowing the water to function as the absorber. This radiative heat transfer mechanism creates steep temperature gradients at the interface, effectively governing heat conduction. Moreover, the lack of direct interaction between the absorber and the water reduces the interfacial thermal resistance, allowing the system to overcome temperature pinning at the boiling point. As a result, the contactless solar evaporator was able to reach vapor temperatures as high as 133 °C. These studies demonstrate that heat loss during the evaporation process can be effectively mitigated. However, directly reducing heat loss in the vapor generation process through specific structural designs presents a significant challenge. Xu and co-workers have proposed a novel approach to harness energy from both bulk water and the surrounding environment to boost water evaporation.[46] A cold evaporation surface (CES) was placed between the solar evaporator and bulk water, where it absorbs the conduction losses from the evaporator and uses them for cold evaporation before they reach the bulk water. Similarly, a heatsink-like photothermal evaporation system has been developed (Fig. 5e).[75] Vertical fin structures are placed below the upper evaporation surface, linking the bulk water to the evaporation area. Adjusting the number of fins contributes to a reduction in the temperature of the upper evaporation surface, lowering it below the surrounding ambient temperature. This effectively mitigates both radiation and convection heat losses. The fin surfaces undergo cold evaporation, where the heat from the upper evaporation surface is not dissipated to the surroundings but is instead rapidly utilized to enhance water evaporation on the fins. This process induces substantial energy harvesting from the surrounding environment, significantly enhancing overall solar evaporation efficiency. Distinctly, James and co-workers proposed a novel strategy in which exhausted heavy metal ion adsorbents were upcycled as solar evaporators. By incorporating a cold evaporation surface between the evaporator and bulk water, they significantly reduce heat conduction losses during evaporation and improve the overall solar-to-vapor efficiency, as well as preventing the leakage of heavy metal ions from the adsorbents (Fig. 5f).[76] This "waste-to-resource" strategy embodies excellent sustainability and environmental friendliness, making it highly applicable for the remediation of contaminated water.

2.4 Optimization of mass transfer

In contrast to the solar-to-vapor conversion process, mass transport plays a vital role within the evaporator structure, constituting a key phase in solar evaporation. This process comprises four primary stages: (1) water is transported to the evaporation surface *via* capillary action, facilitating continuous

evaporation. (2) Salt ions ascend through the water channels from the bulk water to the evaporation surface. (3) Water molecules are activated within the internal framework of the evaporator. (4) Vapor forms at the air–water interface and diffuses into the surrounding environment, driven by the concentration gradient. Since vapor primarily forms on one side of the interface, while water and salt ions move on the other, and considering the much faster diffusion rate of salt compared to water flow, these transport processes can be divided into three distinct mechanisms: water transport, vapor transport, and salt transport processes. In this section, we will discuss the first three processes while the process of vapor transport will be discussed separately in section 2.4.4.

2.4.1 Water transport. During the evaporation process, water molecules enter the interior of the evaporator through capillary action, forming liquid columns.[77] The height of the column can be defined by Jurin's law for capillary effects:

$$h = \frac{2 \times \gamma \times \cos\theta}{\rho g r} \quad (24)$$

where γ represents the liquid–air surface tension, θ is the contact angle, ρ is the liquid density, g denotes the acceleration due to gravity, and r is the radius of the nanochannel. This equation highlights the factors influencing water transport in solar evaporators. For the hydrophobic solar evaporator with $\theta > 90°$, water and dissolved salts are effectively repelled, explaining their superior anti-fouling properties (detailed in Section 2.5.1). Conversely, in a hydrophilic evaporator, a smaller radius r, higher surface tension γ, lower density ρ, and smaller contact angle θ enhance capillary rise, resulting in a greater height h and increased capacity for water transportation. However, it is important to note that a faster water supply does not necessarily translate to an improved evaporation rate. In general, maintaining a balance between water supply and demand at the evaporation surface facilitates the acceleration of water evaporation. When the evaporation surface is excessively wetted, it tends to form a water membrane.[78] This membrane acts as a barrier, requiring the heat absorbed by the illuminated surface to first traverse through it before reaching the evaporation surface. In contrast, when wettability is inadequate, some heat is absorbed by the dry area of the solar absorber before transferring to the dry–wet interface. The increased heat and mass transfer resistances lead to a reduction in the evaporation rate.[79] Therefore, the wetting management of the evaporator surface is vital to promote the evaporation rate. In this section, we will first introduce the necessity of wetting management to promote the water evaporation rate, and then summarize different types of water transportation methods including capillary-driven water supply and water injection technology, as well as critically discussing each of the methods.

In 2020, Guo *et al.* introduced a hydrophilic hydrogel evaporator featuring hydrophobic island-shaped patches (PSHs). This design traps a significant amount of water within the hydrophilic regions, creating a thin water film that promotes the rapid escape of water molecules (Fig. 6a).[80] A substantial number of water molecules diffuse across the contact

This journal is © The Royal Society of Chemistry 2025

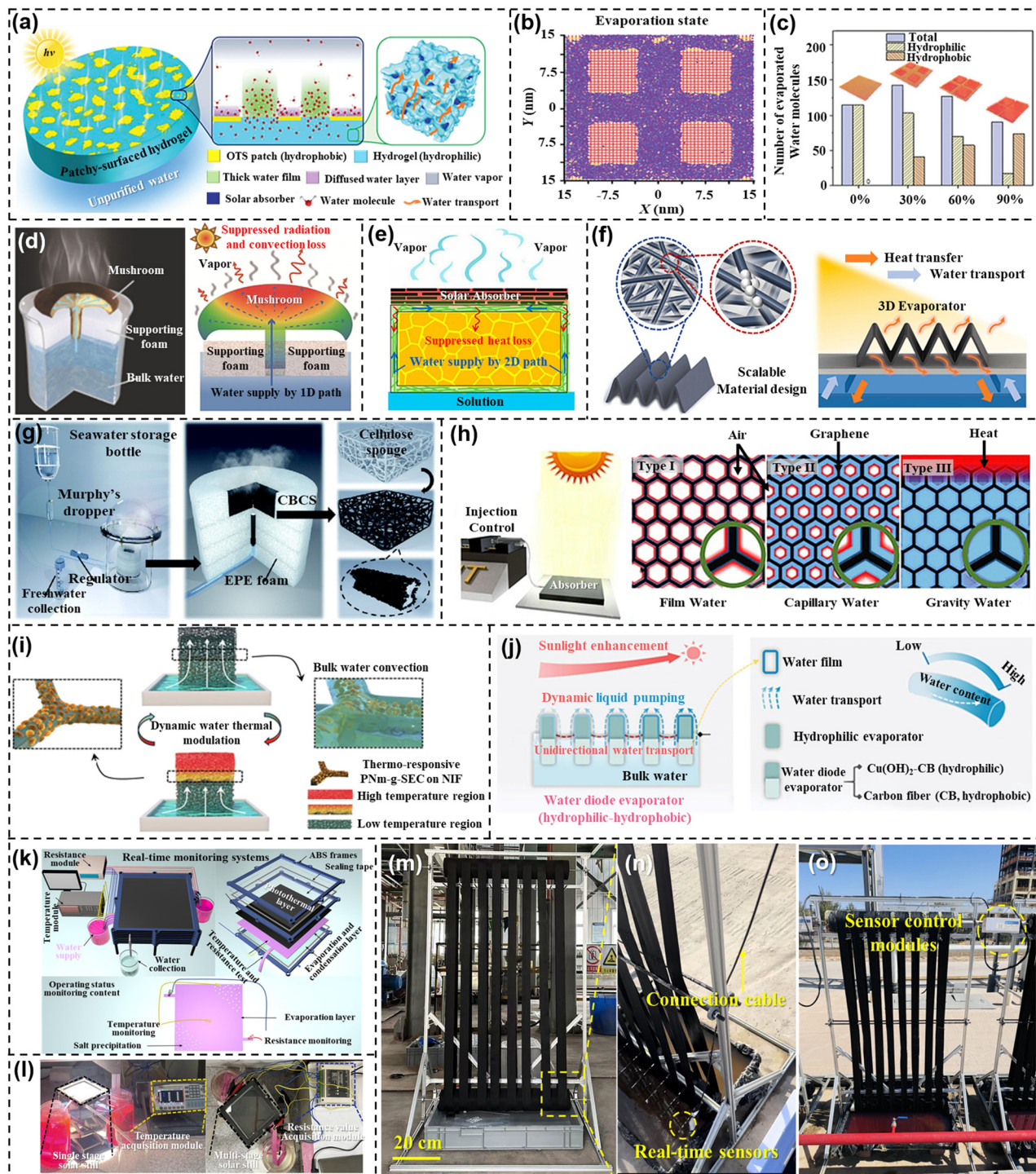*Energy Environ. Sci.*, 2025, **18**, 6366–6437 | **6375**

Fig. 6 Dynamic regulation strategies for balancing water transport and evaporation rates. (a) Diagram of patchy-surface hydrogels (PSHs) designed for improved solar-driven evaporation, illustrating the distribution of water molecules between the hydrophilic and hydrophobic regions; (b) MD simulation showing the water evaporation process on the surface of the PSHs; (c) number of evaporated water molecules for different OTS surface coverages. (a)–(c) Reprinted with permission.[80] Copyright 2020, Royal Society of Chemistry. (d) Typical one-dimensional water supply in the ISVG process. Reprinted with permission.[81] Copyright 2017, Wiley-VCH; (e) typical two-dimensional water supply in the ISVG process. Reprinted with permission.[82] Copyright 2016, National Academy of Science; (f) schematic diagram of the preparation of 3DVG and its heat and mass transfer process in a 3D evaporator. Reprinted with permission.[83] Copyright 2023, Elsevier; (g) schematic diagram of the water injection device and process system. Reprinted with permission.[84] Copyright 2019, Royal Society of Chemistry; (h) schematic of the injection control technique (ICT) for capillary water formation and vapor diffusion during the ISVG process. Reprinted with permission.[85] Copyright 2019, Wiley-VCH; (i) dynamic water-thermal management principles of SDWEs. Reprinted with permission.[86] Copyright 2024, Springer Nature; (j) mechanism of the dynamic water transport process of the WD-CFC evaporator. Reprinted with permission.[87] Copyright 2024, Wiley-VCH; (k) schematic diagram of the operating status monitoring system;[23] (l) experimental setup of the resistance and temperature value acquisition modules;[23] (m) overview of the solar-wind complementary system; (n) close-up of the connection cables and real-time sensors integrated into the solar-wind complementary system; (o) field test and feedback of the solar-wind complementary system equipped with real-time sensors for environmental conditions (i.e., temperature, wettability, wind speed and solar intensity). (m)–(o) Our group work, Product Copyright@Xi'an Qinshengfeng Tech. Co. Ltd, Photo copyright @ author Yawei Yang, All rights reserved.

6376 | Energy Environ. Sci., 2025, 18, 6366–6437

This journal is © The Royal Society of Chemistry 2025

lines into the hydrophobic zone, creating a thinner water vapor layer while preserving a heat-localized region that enhances evaporation. The interaction between these two wetting regions works in harmony to markedly increase the water evaporation rate, achieving an outstanding value of approximately 4.0 kg m^{-2} h^{-1} with 93% efficiency under standard solar conditions. Molecular dynamics (MD) simulations were performed to explore the water evaporation process on the PSH surface (Fig. 6b). In the course of evaporation, water molecules first spread across the hydrophilic region made of polyvinyl alcohol (PVA). At the same time, many water molecules moved from the contact lines into the hydrophobic zone, which is functionalized with trichloro(octadecyl)silane (OTS), where they subsequently underwent evaporation. An increase in the coverage of OTS resulted in the formation of a thicker average water film and a decrease in the average total interaction energy of the outermost water molecules in the PVA region. This observation suggests a reduction in the energy barrier associated with the evaporation process. However, additional increases in OTS coverage improved evaporation from the hydrophobic region but also led to a notable reduction in the hydrophilic area, which in turn lowered the overall evaporation rate (Fig. 6c). In summary, hydrophilic surfaces play a key role in directing water to the heat-localized interface, facilitating rapid evaporation. However, achieving an optimal balance between water retention on the evaporation surface and fine-tuning the evaporation rate through surface wettability still requires further exploration. By engineering super hydrophilic surfaces, the contact angle is reduced to near zero, maximizing $\cos\theta$ and significantly boosting capillary forces for water transport. This reduction allows the water to rise efficiently through the material, ensuring a continuous and uniform supply to the evaporation interface. Other parameters, such as surface tension (γ) and pore radius (r), are optimized to complement this effect, maintaining sufficient capillary action while balancing heat transfer and transport efficiency. Therefore, such ultrafast evaporation rates with remarkable energy efficiency can only be achieved.

Two key factors—high hydrophilicity and a porous structure that supports efficient water transport—are vital for improving capillary pumping performance at a macroscale. To achieve this, 1D and 2D water pathways with sealed pores are engineered to provide effective water delivery while reducing heat loss. For example, a mushroom-inspired solar evaporator featuring a 1D water path for ISVG (Fig. 6d).[81] Both efficient water supply and minimized heat loss can be achieved simultaneously. In fact, 1D water supply benefits from a smaller cross-sectional area for water transport, significantly reducing heat loss during the evaporation process. However, this design may lead to water depletion along the edges of the evaporation surface, which can reduce the overall evaporation rate. To solve this issue, channel-array configurations have been proposed. These structures help minimize conductive heat loss between the evaporation area and bulk water, while also preventing water depletion at the surface edges. Additionally, thin materials such as paper and cloth, with 2D-like transport paths and 3D porous structures, are commonly used to enhance water

supply. Evaporators incorporating 2D-like transport paths typically exhibit improved evaporation efficiency due to the reduced conductive heat loss, in comparison to those lacking such pathways. Zhu's group has introduced a hydrophilic cellulose layer encasing the polystyrene foam surface, forming a 2D water pathway for solar-driven vapor generation. (Fig. 6e).[82] This design facilitates efficient water delivery while concurrently minimizing heat loss. The energy conversion efficiency with the 2D water pathway achieves 80%, representing a notable enhancement compared to the 50% efficiency seen with direct water contact under one-sun irradiation. In addition, Xu and colleagues designed an affordable, origami-inspired 3D vapor generator (3DVG) made from activated carbon fiber felts, capable of absorbing a wide range of sunlight (Fig. 6f).[83] The 3DVG design features a double-sided 3D evaporation structure, enabling vapor to escape through its peak and valley formations, which enhances solar energy absorption from different angles. Thermodynamic simulations showed that this double-sided structure boosts vapor diffusion, prevents stagnation, and reduces heat loss, resulting in higher evaporation rates and improved energy efficiency. 3D structures offer superior evaporation performance compared to thin, water-absorbing materials. The height and cross-sectional area of 3D pathways are key factors in optimizing evaporation efficiency, as they affect both heat conduction and water supply. Increasing the height of the 3D water pathway reduces conductive heat loss but may also constrain the water supply capacity. Conversely, the cross-sectional area impacts water supply and heat conduction in opposing directions. Therefore, careful optimization of both the height and cross-sectional area of the 3D path is essential for maximizing evaporation performance. However, passive water transport *via* capillary action may lead to surplus water on the evaporation surface, causing heat loss to the surrounding air. To minimize heat loss and ensure continuous operation, it is crucial to align the water transport rate with the evaporation rate, as controlled water transport is key to achieving high solar-to-vapor conversion efficiency. Huang's team developed a novel carbon black-cellulose sponge system in which water is injected, as opposed to being absorbed from a bulk source (Fig. 6g).[84] This system demonstrated an evaporation efficiency of about 91.5%, surpassing traditional systems by roughly 10% under one-sun irradiation. This improved efficiency results from minimized energy losses, achieved by accurately matching the injected water mass with the incoming solar energy. In a similar approach, Qu's team has developed an injection control method to efficiently manage water transport within 3D graphene foam, optimizing performance for solar evaporation (Fig. 6h).[85] Through precise control of the water supply rate and leveraging the balance between the water supply and evaporation rates, the graphene foam maintains a state of partial water absorption. This approach prevents the complete blockage of micro-sized pore channels by water, ensuring that the evaporation surface remains maximized and preventing solar energy from being wasted on heating excess water. As a result, the solar vapor generation rate can reach up to 2.40 kg m^{-2} h^{-1}. In contrast to approaches that balance evaporation and water supply rates

This journal is © The Royal Society of Chemistry 2025

Energy Environ. Sci., 2025, **18**, 6366–6437 | **6377**

through the introduction of external systems, Narayan's group explored a dynamically responsive surface with switchable wettability for efficient evaporation and self-cleaning abilities.[88] The key principle behind this dynamic wettability is the use of aminosilane-functionalized surfaces, where the surface's contact angle can be tuned from $155°$ to nearly $0°$ depending on the environmental conditions. This shift in wettability results in drastic changes in the evaporation kinetics, with substantial improvements in heat dissipation and surface cooling. Such surfaces could enable real-time control by adjusting the wettability to optimize evaporation rates under different operational conditions. Recently, Tam and his team introduced a bilayer-structured solar evaporator (SDWE) featuring a dynamic water-thermal control system that automatically alternates between efficient thin water evaporation and salt washing (Fig. 6i).[86] The SDWE is constructed using nickel foam as the base material, featuring two primary layers: a polydopamine nanosphere-assembled interfacial layer (PDA) and a thermo-responsive sporopollenin-engineered layer (PNm-g-SEC). The PDA layer serves as the photothermal interface, while the PNm-g-SEC layer functions as a switchable gating mechanism. At high temperatures, the PNm-g-SEC layer becomes superhydrophobic, guiding water through specific channels and optimizing evaporation. At lower temperatures, it turns hydrophilic, facilitating bulk water backflow to prevent salt buildup. Similarly, Wang's group reported the concept of a photothermal water diode (WD–CFC) evaporator (Fig. 6j).[87] This evaporator integrates a Janus structure with hydrophilic and hydrophobic properties to enable unidirectional water transport. The design ensured that water is dynamically transported to the evaporation surface in response to varying solar intensities, adjusting the water supply to maintain energy efficiency. Actually, the core mechanism of the water diode relies on the Janus structure (hydrophilic/hydrophobic surfaces) that facilitates unidirectional water flow. The hydrophilic top layer (HL) and hydrophobic bottom layer (HP) create a wettability gradient that drives water upward from the HP side to the HL side with no backflow. The flow rate Q_{flow} was driven by capillary action is described by the following equation:

$$Q_{flow} = \frac{\Delta P \cdot r^4}{8 \mu L} \tag{25}$$

where ΔP is the pressure difference caused by evaporation-induced capillary pressure; r is the radius of the capillaries; μ is the dynamic viscosity of water; L is the length of the capillary. The pressure difference ΔP can be defined by the capillary pressure due to the surface tension, given by:

$$\Delta P = \gamma \left(\frac{1}{r_1} + \frac{1}{r_2} \right) \tag{26}$$

where γ is the surface tension of water; r_1 and r_2 are the radii of curvature of the capillaries. Thus, the flow rate Q_{flow} depends on the evaporation-induced pressure difference ΔP_{evap}, which increases with higher solar radiation intensity I_{solar}, resulting in an increased water supply rate:

$$Q_{flow} \propto \Delta P_{evap} I_{solar} \tag{27}$$

This equation shows that the water flow rate Q_{flow} adjusts dynamically in response to the solar radiation intensity. Specifically, if water supply exceeds the evaporation capacity, energy waste occurs; if water supply is insufficient, evaporation cannot be sustained. Therefore, the system must dynamically adjust the water supply based on the solar radiation intensity to ensure a balance between energy input and evaporation rate.

While the theoretical framework for water diode systems highlights the importance of tuning the wettability gradient to balance water supply and evaporation rate, the practical implementation in engineering applications requires careful attention to the dynamic equilibrium between these two factors. In real-world systems, maintaining this balance is crucial for optimizing operational efficiency and ensuring the sustained performance of the system. Our group developed a real-time monitoring system that tracks resistivity and temperature to assess the operational status of multistage solar stills (Fig. 6k).[23] This system allows for the monitoring of crucial parameters, including water supply status, irradiance intensity, and salinity, through changes in resistivity at the water inlet, as well as the salt precipitation status in the evaporation dead zones (Fig. 6l). This research provides a theoretical foundation for the engineering application of real-time monitoring systems. Building on the detection system developed in this study, our team has integrated real-time sensors for temperature, humidity, and light intensity into the solar-wind complementary desalination system. Based on the acquired data, the water supply rate and operational speed of the system can be dynamically adjusted (Fig. 6m–o), ensuring optimal performance under varying operational conditions. These advancements not only offer valuable insights into system performance but also pave the way for future improvements in the design and operational efficiency of solar stills, making them more adaptive and reliable for real-world applications. In alignment with the principle of regulating water transport, optimizing the balance between the water supply rate to the evaporation surface and the heat loss within the solar vapor generation system is crucial for achieving high-efficiency solar-driven water evaporation.

2.4.2 Water activation. In the above analysis of water phase transitions and water transport mechanisms, we focus on optimizing the water evaporation process by reducing latent heat and enhancing water–interface interactions. In fact, during the water and salt transportation process, water molecules are forced into the internal structure of solar evaporators by the capillary effect. In hydrophilic evaporators, water molecules are activated by reducing the energy required for evaporation through enhanced interactions with the hydrophilic surfaces, promoting efficient phase change. Unlike methods that harness external energy (i.e., solar irradiation and environment energy) to enhance the evaporation rate, the activation of water molecules facilitates evaporation by lowering the energy barrier necessary for water molecules to vaporize. This section begins with an introduction to the three forms of water found in nature: free water (FW), bound water (BW), and intermediate water (IW). It will then provide a summary of the water

6378 | *Energy Environ. Sci.*, 2025, **18**, 6366–6437

This journal is © The Royal Society of Chemistry 2025

activation mechanism in the ISVG process, highlighting the reduction in evaporation enthalpy due to liquid water clusters, as explained by thermodynamic principles. Lastly, three methods of water activation will be discussed, followed by a critical evaluation of each approach.

Water activation is a physical process that occurs within the solar evaporator during the mass transportation. Water molecules can form weaker hydrogen bonds or non-hydrogen bonds with the polar functional groups of hydrophilic materials (such as polymer materials or porous materials). These weaker bonds are easier to break compared to ordinary hydrogen bonds, thus requiring less energy for evaporation. Specifically, the energy required to evaporate water, termed the enthalpy of evaporation, is around 2260 kJ kg^{-1} at 100 °C, primarily due to the robust hydrogen bonds among water molecules. Breaking these bonds, which facilitate the transition from liquid to vapor, demands substantial energy. Although prior studies have explored methods to reduce the equivalent evaporation enthalpy and enhance solar evaporation rates, a comprehensive theoretical framework that elucidates the mechanisms behind enthalpy reduction remains absent. This section explores the theoretical foundations of water activation, focusing on enthalpy reduction and water cluster formation through thermodynamic theory and analytical derivation. Finally, we will propose three key mechanisms of water activation associated with these water states, enhancing our understanding of their contributions to improved solar evaporation rates. The solar-to-vapor conversion efficiency (η) is mentioned in section 2.2.2. Actually, in ISVG systems, the total heat required (h_{lv}) for the transition of water to the vapor state comprises both sensible and latent heat components.[89] Sensible heat (ΔH_{sen}) which raises or lowers the water's temperature without causing a phase change, can be quantified using the equation below:[89]

$$\Delta H_{sen} = C \times (T - T_0) \quad (28)$$

where C denotes the specific heat of water (4.18 J g^{-1} K^{-1}); T_0 represents the initial temperature of the water (K); and T indicates the stable surface temperature of the sample, measured using an infrared camera (K). The latent heat of phase change (ΔH_{hlv}) refers to the heat absorbed or released per unit mass of a substance during a phase transition at constant temperature and pressure. This is also known as enthalpy of vaporization (ΔH_{vap}), which is the energy required for water to vaporize at a constant evaporation temperature. This energy is largely consumed in breaking the intermolecular hydrogen bonds between water molecules, which will be further explored in the following section.

Since sensible heat plays a smaller role than latent heat, reducing overall energy requirements involves lowering the enthalpy of evaporation. This enthalpy depends not only on the material properties, such as the matrix and absorber materials, but also on the temperature of the heated surface (T), which affects the substance's vapor pressure. These factors are crucial when adjusting the state of water in a solar vapor generation (ISVG) system to achieve a lower evaporation enthalpy. Enthalpy (H) combines internal energy (E) with the

product of pressure (p) multiply volume (V). Based on thermodynamic principles, the latent heat of water evaporation (ΔH_{vap}) is determined by the difference in enthalpy between the gaseous phase (H_{gas}) and liquid phase (H_{l-w}):

$$\Delta H_{vap} = H_{gas} - H_{l-w} = (E_{gas} - E_{l-w} + (pV_{gas} - pV_{l-w}) \quad (29)$$

Internal energy (E) includes both kinetic energy (K) and intermolecular potential energy (U). The latter can be further divided into intermolecular potential (U_{inter}), representing the energy between water molecules, and intramolecular potential (U_{intra}), associated with the energy within molecular bonds. The expressions for internal energy in both gas and liquid phases are as follows:

$$E_{gas} = K_{gas} + U_{gas}^{inter} + U_{gas}^{intra} \quad (30)$$

$$E_{l-w} = K_{l-w} + U_{l-w}^{inter} + U_{l-w}^{intra} \quad (31)$$

Substituting eqn (30) and (31) into eqn (29), the vaporization enthalpy is therefore as follows:

$$\Delta H_{vap} = (K_{gas} - K_{l-w}) + (U_{gas}^{intra} - U_{l-w}^{inter} - U_{l-w}^{intra}) + (pV_{gas} - pV_{l-w}) \quad (32)$$

At room temperature and 1 atm, the intermolecular potential of water vapor is negligible ($U_{gas}^{inter} = 0$), allowing us to treat the water vapor as an ideal gas:[90]

$$pV_{gas} = Nk_bT \quad (33)$$

where N represents the number of water molecules, k_B is the Boltzmann constant, and T is the temperature. At the same temperature, the kinetic energy of water molecules is the same in both the liquid and gas phases, so $K_{gas} = K_{l-w}$. Similarly, the vibrational energy of bonds in each water molecule remains consistent across phases, meaning $U_{gas}^{intra} = U_{l-w}^{intra}$. For a given number of molecules, the volume of liquid water is smaller than that of water vapor, so $pV_{gas} \gg pV_{l-w}$, eqn (32) can therefore be simplified to yield the final formula, as shown below:

$$\Delta H_{vap} = pV_{gas} - U_{l-w}^{inter} = -U_{l-w}^{inter} + Nk_bT \quad (34)$$

Taking into account the additional pressure due to surface tension on the enthalpy of evaporation, the pressure driven by surface tension (ΔP) is given by the following equation:[91]

$$\Delta P = 8\sigma \frac{\cos \theta}{d} \quad (35)$$

where σ denotes the surface tension between water and the gas–liquid interface; θ is the contact angle and d represents the pore diameter. Based on eqn (33) and (34) it can be expressed as follows:

$$\Delta H_{vap} = Nk_bT - U_{l-w}^{inter} - \left(P + 8\sigma \frac{\cos \theta}{d}\right)V_{l-w} \quad (36)$$

Eqn (32) and (36) theoretically show that the enthalpy of evaporation is linked to the intermolecular potential energy (PE) of water and the gas–liquid surface tension (σ) of water. By reducing the binding potential energy between water molecules,

This journal is © The Royal Society of Chemistry 2025

Energy Environ. Sci., 2025, **18**, 6366–6437 | **6379**

the evaporation enthalpy can be effectively lowered. This approach promotes the formation of weaker hydrogen or non-hydrogen bonds, which can be easily broken, either partially or entirely, during the evaporation process. Furthermore, when water molecules are confined within a hydrogel matrix, they are more likely to escape as small clusters rather than large ones. The evaporation enthalpy for both pure water ($\Delta H_{\text{p-water}}$) and water trapped in hydrogels ($\Delta H_{\text{cluster}}$) can be determined using the equation below:[92]

$$\Delta H_{\text{p-water}} = -U_{\text{l-w}}^{\text{inter}} + Nk_{\text{b}}T \tag{37}$$

$$\Delta H_{\text{cluster}} = -[xU_{\text{l-w}}^{\text{inter}} + (1-x)U_{\text{cluster-water}}] + Nk_{\text{b}}T \tag{38}$$

where $U_{\text{l-water}}^{\text{inter}}$ represents the bond energy of liquid water while $U_{\text{cluster-water}}$ denotes the energy required for the evaporation of water clusters. N is the number of water molecules, T is the temperature, k is the Boltzmann constant, and x indicates the fraction of a gas phase. Smaller water clusters, such as intermediate water (IW), require fewer hydrogen bonds to be broken for evaporation compared to larger clusters like free water (FW). Therefore, the energy ($-U_{\text{cluster-water}}$) required to vaporize small clusters is lower than the bond energy of liquid water ($U_{\text{l-water}}^{\text{inter}}$), indicating that $\Delta H_{\text{cluster}}$ is smaller than $\Delta H_{\text{p-water}}$. This suggests that the presence of smaller water clusters can reduce the enthalpy of evaporation. Actually, water activation refers to a physical process that lowers the energy required for water molecules to transition from the liquid phase to the vapor phase. This reduction in vaporization enthalpy can be understood by considering how water molecules interact with surfaces and each other at the molecular level. Two primary factors contribute to this phenomenon: (1) modification of hydrogen bonding networks: Water molecules in bulk liquid water are held together by strong hydrogen bonds, which contribute significantly to the latent heat of vaporization. When water interacts with hydrophilic materials (Fig. 7a), these interactions

often result in the disruption of the water's hydrogen-bonding network. This is because the material itself can form weaker hydrogen bonds or even non-hydrogen bonds (e.g., electrostatic interactions) with water molecules. These weaker interactions reduce the energy required to break the bonds between water molecules, thus lowering the vaporization enthalpy (Fig. 7b). Meanwhile, the molecular interaction can be understood through the concept of water structure disruption. When water molecules are in close contact with hydrophilic surfaces (such as polymeric materials or porous structures), the bond strength between water molecules decreases, allowing for easier evaporation. This effect is often enhanced by the surface characteristics of the material, such as polarity, porosity, and the presence of functional groups like hydroxyl (–OH) or sulfonate (–SO₃) groups. (2) Formation of water clusters: Water molecules in a liquid state do not always exist as isolated entities (Fig. 7c) but rather tend to form clusters or networks. These water clusters vary in size, and their formation is governed by the intermolecular forces acting within the liquid. Smaller water clusters (often referred to as IW) require less energy to vaporize than individual water molecules or larger clusters (Fig. 7d). This is because fewer hydrogen bonds need to be broken to allow a cluster to transition into the gas phase. Meanwhile, the concept of water clustering is important in the context of vaporization enthalpy reduction. For instance, water trapped in porous media or confined within nanostructures can form clusters of varying sizes. These smaller clusters, because of their reduced number of bonds, vaporize more easily and require less energy to break free from the liquid state.

The mechanisms for reducing vaporization enthalpy through water activation are highly generalizable across various ISVG systems.[66,86,93–100] This generalization arises from the fundamental nature of the interactions between water molecules and surfaces, which can be applied to a broad range of hydrophilic materials, porous structures, and photothermal materials. For example, hydrogels, such as polyvinyl alcohol (PVA) and chitosan, are polymers with high hydrophilicity. When integrated with hydrophilic functional groups (e.g., hydroxyl (–OH) or sulfonate (–SO₃) groups), these hydrogels significantly enhance the formation of IW. Meanwhile, hydrogels are particularly effective because their structure can be engineered to control the proportions of FW, BW, and IW, which directly influences the vaporization enthalpy.[101–103] The water activation mechanism in hydrogels involves the weakening of hydrogen bonds and the optimization of water clustering. By controlling the degree of crosslinking or adjusting the material's chemical functionality, hydrogels can modify the state of water, reducing the energy required for evaporation. The formation of IW is particularly important in this process, as IW requires significantly less energy to evaporate than either free or bound water, thereby lowering the overall vaporization enthalpy. Meanwhile, other porous photothermal materials, such as reduced graphene oxide (rGO) and carbon nanotubes (CNTs), have high surface areas and excellent light-absorbing properties, which also enable them to interact strongly with water molecules.[104–106] The high surface area and polarity of
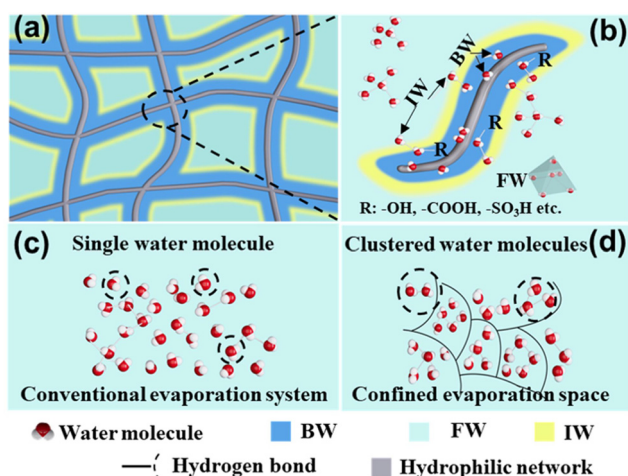

Fig. 7 Molecular-scale mechanisms for water activation. (a) Schematic diagram of a hydrophilic network in evaporator systems; (b) modification of water's hydrogen bonding network; (c) single water molecule in conventional evaporation systems; (d) clustered water molecules in confined evaporation space.

6380 | *Energy Environ. Sci.*, 2025, **18**, 6366–6437

This journal is © The Royal Society of Chemistry 2025

these materials allow for the activation of water through both physical adsorption and photothermal effects. As these materials absorb solar energy and convert it into heat, they further enhance the activation of water molecules, making them easier to vaporize. This process reduces the energy barrier for evaporation and consequently lowers the vaporization enthalpy. In addition, nanostructured materials, such as metal–organic frameworks (MOFs), also facilitate water activation due to their high surface area and tunable surface chemistry.[107–109] Specifically, pore size and surface characteristics can be precisely tailored to optimize the interaction with water molecules. This leads to the formation of water clusters, which require less energy to evaporate compared to individual water molecules. By controlling the pore size and surface properties, nanostructured materials enable the formation of a high proportion of intermediate water, further lowering the energy required for evaporation and improving the efficiency of the evaporation process.

Overall, the mechanisms of water activation that reduce vaporization enthalpy are widely applicable to various ISVG systems, particularly in hydrophilic materials, photothermal materials, and nanostructured materials. These materials facilitate water activation through different mechanisms, such as modifying hydrogen bonding networks, promoting water clustering, and optimizing pore structure. The generalizability of these mechanisms makes them suitable for a wide range of applications, enhancing the scalability and practical implementation of ISVG technology in diverse environments. Building on this theoretical framework, we propose three strategies to activate water in solar evaporators: (1) increase the concentration of IW within the evaporator network, (2) promote the formation of water clusters to reduce the vaporization enthalpy, and (3) enhance the effective evaporation surface by boosting capillary water formation, as depicted in Fig. 8.

Intermediate water content increasement. Approaches for activating water have been designed to lower the energy needed for evaporation and boost vapor generation. Materials with strong interactions with water molecules can influence the state and phase-transition behavior of water. Yu's team pioneered the investigation into the connection between the energy needed

for water evaporation and the different states of water within hydrogels.[91,110] They found that the polar groups in naturally hydrophilic hydrogels or photothermal materials are capable of forming weak hydrogen bonds with nearby water molecules. The sulfonate ($-SO_3H$) and hydroxyl ($-OH$) groups in hydrophilic polymer gels can disrupt the hydrogen bonding network among water molecules (Fig. 9a).[111] In addition, groups such as amine ($-NH_2$), carboxylic acid ($-COOH$), epoxy ($-CH(O)CH-$), aldehyde ($-CHO$), and carbonyl ($C=O$) can enhance the hydrophilicity of surfaces. For instance, chitosan containing $-NH_2$ groups has been suggested to create highly hydratable polymer networks, thereby regulating water–polymer interactions in a light-absorbing hydrogel. In this design, the water state was modified by raising the chitosan/PVA weight ratio, which reduced the energy needed for water vaporization and greatly enhanced the solar water evaporation rate to 3.6 kg m^{-2} h^{-1}.[92] Water generally exists in three forms: free water (FW), bound water (BW), and intermediate water (IW), each characterized by the strength of its interactions with surrounding materials and the intensity of intermolecular forces (Fig. 9b).[112] BW denotes the water molecules that are strongly attached to the functional groups in polymer chains as a result of the hydration effect. In contrast, FW is similar to bulk water, having negligible interactions with the materials. IW exists as an intermediate state between bound water and free water. Certain materials interact strongly with water to form BW, which weakens the hydrogen bonds in the surrounding water network. This disruption results in the formation of a substantial amount of IW, altering the water's state and phase-transition behavior. Breaking these additional hydrogen bonds requires extra energy, thereby increasing the latent heat of vaporization. However, the presence of IW, characterized by its weaker hydrogen bonds, reduces the energy needed for evaporation, thus accelerating the process. Furthermore, during the ISVG process, IW is typically confined near the surface of nanoporous light absorbers, which receives a steady supply of thermal energy, experiences higher localized temperatures, and offers a larger evaporation surface area. As a result, the evaporation of IW requires significantly less energy, establishing a fundamental principle for enhancing solar evaporation rates through increased IW content. Yu and co-workers incorporated polystyrene sulfonate (PSS) into a polyvinyl alcohol (PVA) matrix
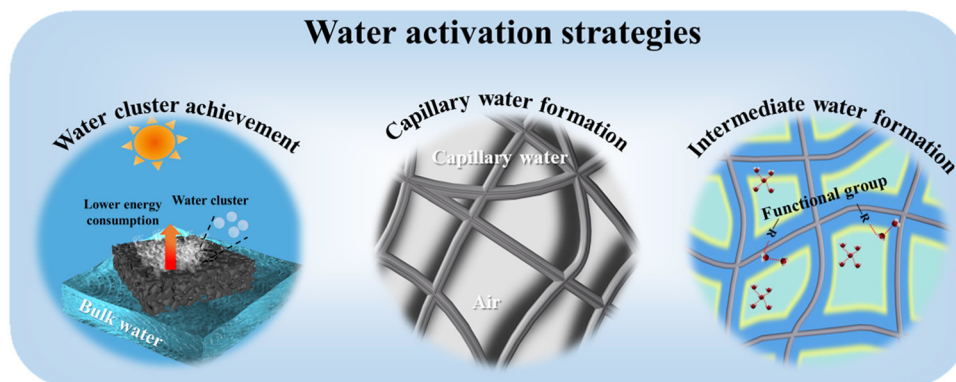

Water activation strategies

Fig. 8 Schematic diagram of water activation strategies.

This journal is © The Royal Society of Chemistry 2025

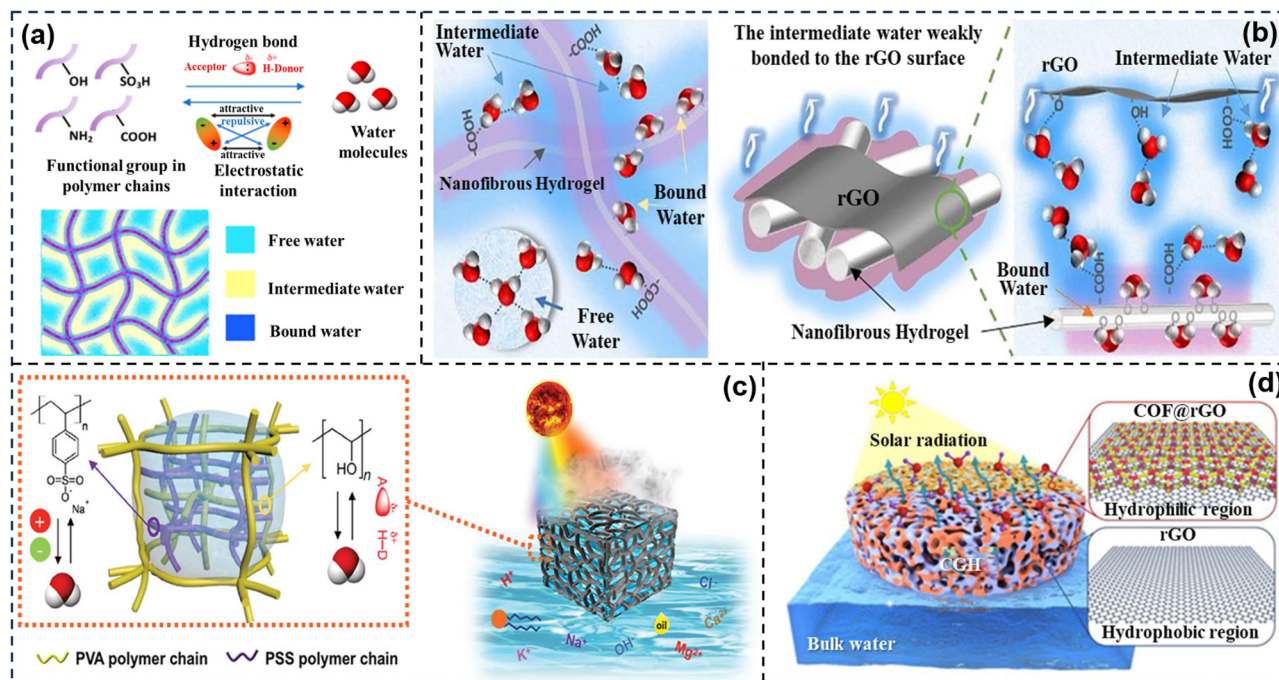*Energy Environ. Sci.*, 2025, **18**, 6366–6437 | **6381**

Fig. 9 Intermediate water increasement for water activation. (a) Different water states led by interaction between materials and water. Reprinted with permission.[111] Copyright 2019, American Chemical Society; (b) schematic diagram of three different water forms during the solar evaporation process from the hydrogel-reduced graphene oxide (NHrG) membrane. Reprinted with permission.[112] Copyright 2021, Elsevier; (c) schematic illustration of different water forms in the PVA/PSS hydrogel. Reprinted with permission.[113] Copyright 2021, Wiley-VCH; (d) diagram of the COF@rGO hydrogel enhancing hydrophilicity to produce more intermediate water. Reprinted with permission.[114] Copyright 2022, American Chemical Society.

to modify water state and phase transition behaviors. The PSS promotes the formation of intermediate water (IW) by interacting with water molecules through electrostatic forces and hydrogen bonding, thereby lowering the evaporation enthalpy (Fig. 9c).[113] The highly crosslinked polyvinyl alcohol restricts water saturation within the hydrogel, reducing energy loss and improving the solar vapor generation rate to 3.9 kg m^{-2} h^{-1}, with an energy efficiency of 92% under one-sun irradiation. Recently, Thomas' team introduced a dual-region hydrogel evaporator that incorporates covalent organic frameworks (COF) and graphene through an *in situ* growth method (Fig. 9d).[114] This hydrogel consists of a hydrophilic COF-loaded reduced graphene oxide (COF@rGO) region and a hydrophobic pure rGO region. The –SO$_3$H/–SO$_3^-$ groups in the COF within the dual-region hydrogel network help regulate water content. Increasing the COF@rGO proportion improves hydrophilicity, generating more intermediate water, while also increasing the macropore size, which results in more free water. By systematically optimizing the proportions of these two regions, the hydrogel's capillary channel size and wettability can be adjusted. This allows precise control over water content and its state, leading to reduced energy consumption for water evaporation, measured at 1043 J g^{-1} in the dark evaporation test. These examples demonstrate that well-designed materials and structures can enhance weak interactions with nearby water molecules, increasing intermediate water. The IW mechanism is widely used for activating water and serves as the basis for many subsequent studies. It highlights the synthesis and preparation of materials, which can be analyzed qualitatively and

quantitatively using advanced techniques such as Raman spectroscopy and Fourier transform infrared spectroscopy (FTIR).

Water cluster formation. In nature, water exists in ice or liquid form as clusters, which are assemblies of several molecules bonded together by hydrogen bonds. Water can evaporate as individual molecules or as clusters ranging from a few to tens of molecules. Water clusters have a dynamic structure, with molecules continuously forming and breaking apart, leading to fluctuating cluster sizes. During evaporation, a water cluster only needs to break the hydrogen bonds with the surface, while individual molecules must disrupt all their hydrogen bonds, requiring more energy. Additionally, smaller water clusters move faster than larger ones, indicating that transforming liquid water into individual water vapor molecules demands more energy than converting it into vapor clusters. Yu and colleagues were the first to show that integrating polypyrrole (PPy) into a polyvinyl alcohol (PVA) gel network could efficiently regulate the various water clusters within the gel (Fig. 10a).[115] This hierarchically nanostructured polymer gel, featuring a hydrogel molecular mesh, exhibited a solar evaporation rate of 3.2 kg m^{-2} h^{-1}. This rate surpasses the theoretical evaporation limit of conventional evaporators, highlighting the significant impact of their innovative design. By optimizing the interaction between PPy and PVA, the team successfully enhanced the efficiency of solar-driven water evaporation, marking a notable advancement in the field. Building on the formulas derived by Yu and colleagues, Liu's group assessed
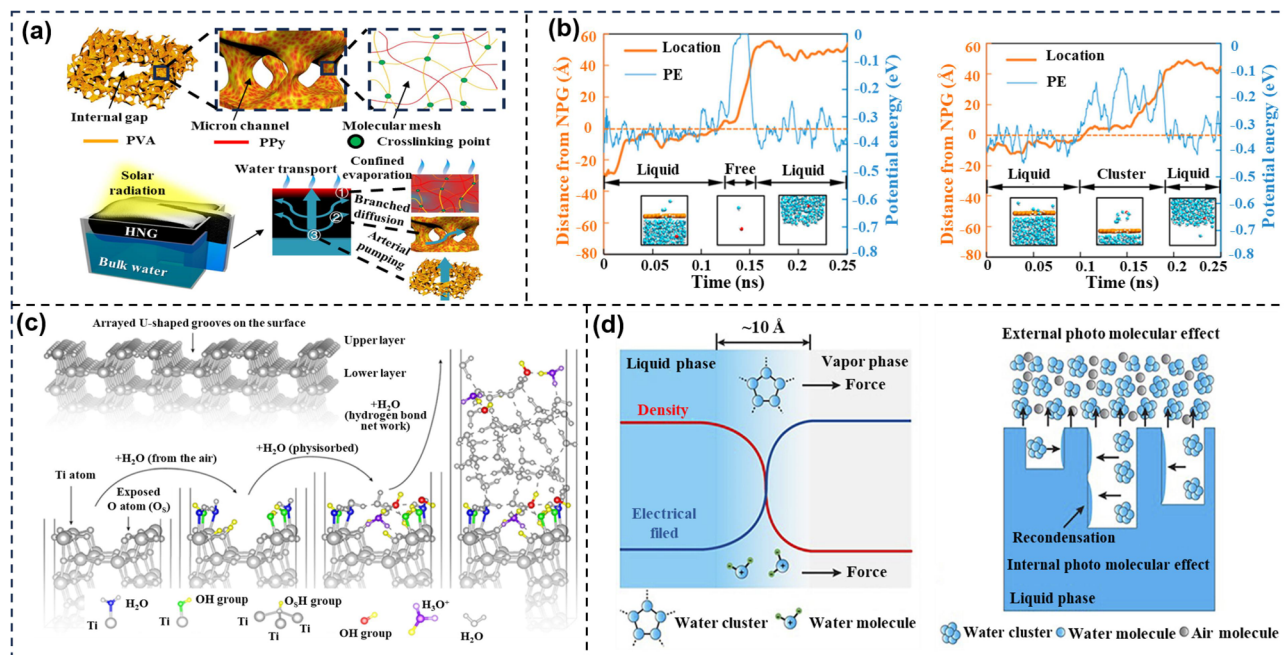
Fig. 10 Water cluster formation in the ISVG process. (a) Water cluster escaped from the network of the HNG gel for efficient solar vapor generation. Reprinted with permission.[115] Copyright 2018, Springer Nature; (b) evaluation of the position and potential energy of water molecules during movement.[116] Reprinted with permission. Copyright 2020, American Chemical Society; (c) water cluster on the surface of λ-Ti$_3$O$_5$ for effective solar evaporation. Reprinted with permission.[117] Copyright 2023, Springer Nature; (d) schematic diagram of a novel photo molecular effect facilitating the escape of small water clusters. Reprinted with permission.[118] Copyright 2023, National Academy of Science.

the potential energy (PE) and spatial arrangement of water clusters in a reverse thermo-osmosis system, along with a quantitative analysis of their unstable state (Fig. 10b).[116] Their findings indicated that the potential energy (PE) of water clusters is lower than that of individual water molecules. As a result, the evaporation of clusters demands less heat energy than that of single molecules with the same mass, leading to a decrease in the enthalpy of evaporation. Recently, Zuo's group reported novel metallic λ-Ti$_3$O$_5$ powders, which exhibit a remarkable mean solar absorptivity of 96.4%, and their integration into 3D porous PVA hydrogel evaporators with a conical cavity, resulted in an exceptionally high-water evaporation rate of 6.09 ± 0.07 kg m^{-2} h^{-1} under 1 sun of irradiation without salt precipitation (Fig. 10c).[117] To reveal the evaporation mechanism, DFT simulations demonstrated that the Ti–Ti dimers on the most stable surface of λ-Ti$_3$O$_5$ can decompose initially chemisorbed water molecules into hydroxyl (–OH) and hydrogen (H), which then bind to Ti and O atoms on the λ-Ti$_3$O$_5$ surface, respectively, resulting in surface hydroxylation. Furthermore, the unique U-shaped groove structure on this surface facilitates rapid proton exchange, enabling the formation of metastable H$_3$O* units within the physically adsorbed water layer on the hydroxylated surface. These H$_3$O* units weaken the hydrogen bonding interactions between water clusters containing H$_3$O* and the surrounding water molecules. This mechanism fundamentally reveals that water molecules on the λ-Ti$_3$O$_5$ surface evaporate as clusters under illumination, revolutionizing the traditional understanding of water evaporation as involving individual molecules. Distinctly, Chen's group proposed and

demonstrated a novel photo molecular effect (Fig. 10d).[118] They found that the difference in dielectric constants between air and water creates a significant electric field at the water–air interface. This electric field drives the photo molecular process, cleaving small water clusters from the remaining liquid. These tiny clusters, made up of just a few water molecules, can quickly escape into the air without going through the photothermal process. This mechanism contributes to an evaporation rate of 2.4 kg m^{-2} h^{-1}, which surpasses the thermal evaporation limit of approximately 1.45 kg m^{-2} h^{-1}.

Capillary water formation. In an evaporation system, water can be categorized into hygroscopic, film, capillary, and gravitational types. At low water levels, the system is rich in capillary water with minimal hygroscopic or film water, and lacks gravitational water. Hygroscopic water is strongly adsorbed to the material's surface, whereas film water creates a low-interaction layer around it. As water content approaches or surpasses saturation, capillary and film water decrease, and gravitational water becomes noticeable, filling pore channels and impeding water permeability and evaporation. Moreover, excessive water not only leads to thermal energy loss but also cools the surface, hindering rapid evaporation. Conversely, a well-managed balance of water types enhances capillary water presence, which keeps micropores open for better surface exposure and efficient evaporation. The energy needed to evaporate capillary water is lower than that for pure water, which reduces the vaporization enthalpy. Therefore, regulating the capillary water content within the channels is crucial, as it

decreases latent heat and increases the effective evaporation area. Qu's team has proposed an effective water regulation method, ICT (as discussed in Section 2.4.1), to enhance water evaporation efficiency.[85] By controlling the injection rate *via* the ICT method, they regulated the water content within the rGO foam, achieving a balance between water supply and evaporation. Their system generated a substantial amount of capillary water inside the rGO foam, preventing blockages and expanding the evaporation area, with an evaporation rate of 2.4 kg m^{-2} h^{-1} and a low enthalpy (below 1750 J g^{-1}). Capillary water, commonly found in 3D evaporators, can be managed by adjusting the position of the sunlight-absorbing layer relative to the liquid surface in the 3D structure. Xue and colleagues developed a 3D evaporator made from balsa wood. They found that aligning the light-absorbing layer with the bulk water surface led to complete saturation of the pores with gravitational water (Fig. 11a).[119] Conversely, when the evaporating surface was positioned above the bulk water level, capillary water formed without restriction. This configuration enabled the water within the wood to remain in the capillary state, preventing pore channel blockage and expanding the evaporation area, while also improving the pathways for water vapor to escape. In a similar approach, Wang and his team applied carbonization and freeze-casting methods to create multiple hollow fibers with a capillary structure (Fig. 11b).[120] This design promoted the generation of significant capillary water through the liquid surface film effect, thereby boosting water evaporation and lowering energy consumption. Recently, Chen and colleagues introduced a 3D skeleton-supported hydrogel evaporator engineered to resist shape deformation. By dividing the bulk hydrogel into confined microspaces, they established an interconnected porous structure (Fig. 11c).[121] This novel design utilizes dual capillary-osmosis water supply mechanisms to address the slow osmotic hydration issue commonly found in traditional hydrogels. Particularly, when exposed to solar irradiation, rapid evaporation leads to the shrinkage and eventual cracking of the hydrogel cavities, creating interconnected pores. This transition enables the capillary effect to govern water transport, effectively meeting the increased demand. Simultaneously, the swelling of the inner hydrogel suggests that osmosis further supports water movement. As a result, the dual hydration modes in the modified hydrogel (MGH) significantly improve the water supply rate compared to traditional hydrogels. By employing efficient water regulation methods like ICT and optimizing the placement of the absorber layer relative to the liquid–gas interface in 3D evaporators, researchers have enhanced evaporation performance by promoting capillary water formation. The relatively low dehydration temperature and the weak bonds in capillary water aid in vapor generation. Furthermore, capillary water does not obstruct pore channels and expands the exposed evaporation area, significantly reducing the evaporation enthalpy. Since capillary water forms without requiring further modification of hydrophilic groups, it simplifies the material synthesis process and broadens the range of potential materials. However, the precise mechanisms behind its formation remain unclear, highlighting an important avenue for future research. Nonetheless, the formation of capillary water demands careful control of the water supply, which can make devices utilizing this mechanism more complex and expensive. Unlike conventional freshwater acquisition methods, interfacial water evaporation stands out for its entirely passive nature, requiring no external energy inputs or mechanical components. Therefore, further investigation into more efficient
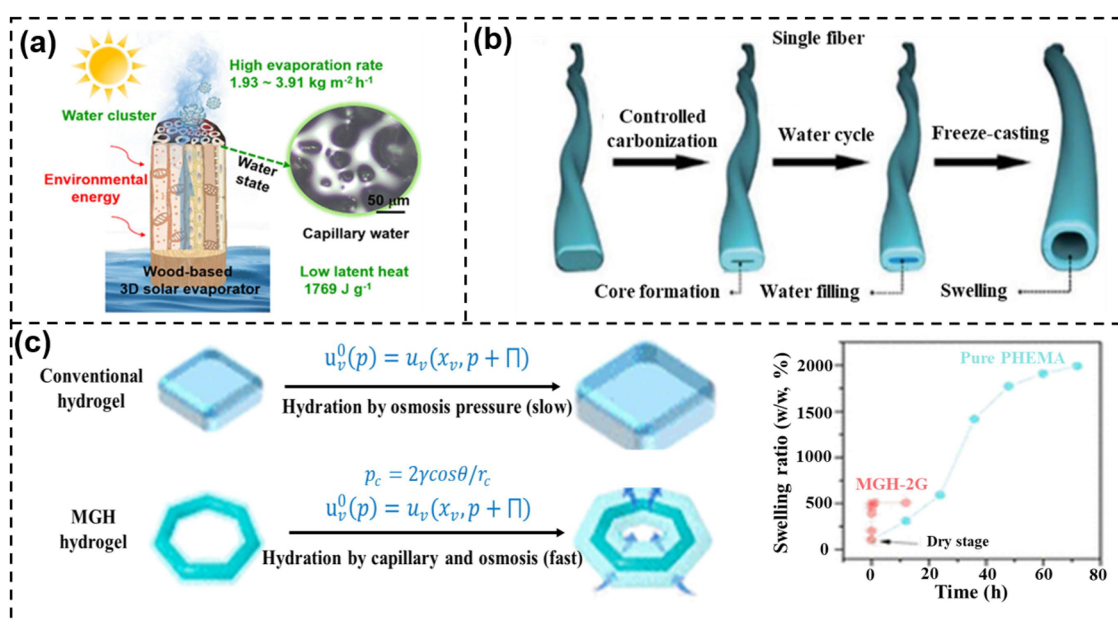

Fig. 11 Capillary water formation in the ISVG process. (a) Capillary water in a wood-based evaporator for vapor generation. Reprinted with permission.[119] Copyright 2020, American Chemical Society; (b) schematic representation of a single fiber transforming into a hollow fiber containing capillary water. Reprinted with permission.[120] Copyright 2021, Royal Society of Chemistry; (c) diagram illustrating the capillary water transport mechanism in both pure hydrogel and MGH, along with their respective swelling ratios. Reprinted with permission.[121] Copyright 2020, American Chemical Society.

and competitive water activation mechanisms is essential to optimize this process.

In conclusion, key strategies to improve vapor yield involve several approaches: firstly, enhancing the proportion of interfacial water (IW) in hydrophilic structures proves advantageous, as IW is characterized by weaker hydrogen or non-hydrogen bonds, which allows it to escape from hydrophilic networks with lower energy costs for evaporation. Secondly, optimizing structural designs to promote the vaporization of clustered liquid water molecules aids in lowering the enthalpy of vaporization. Lastly, boosting capillary water content within pore structures leads to a more efficient evaporation process by reducing blockages. These mechanisms often operate together within the same system, working synergistically to lower the latent heat of evaporation.

2.4.3   Salt ion transport. The salt transport process is determined by the diffusion equation, which could be written as:

$$\nabla \cdot (D_S \nabla \rho_s) = 0 \tag{39}$$

where ρ_s is the concentration of salt, and D_s denotes the mass diffusivity of salt ions. Because of the salinity difference between the evaporation surface and the bulk water, salt ions flow back into the bulk water through the channels in the water absorbers, preventing their accumulation on the evaporator surface. Strategies for anti-salt deposition based on controlling the salt diffusion rate will be outlined in section 2.5.1.

2.4.4   Vapor transport. When water reaches the top of the evaporator, it absorbs heat to form vapor, which then diffuses into the surrounding environment. The transport of vapor involves both the generation and diffusion of vapor. In this section, we will discuss fundamental principles of vapor generation and diffusion at the interface of solar evaporators, as well as proposing strategies to promote vapor diffusion during the ISVG process.

Vapor generation. When water reaches the top of the evaporator, it absorbs heat to form vapor, which then diffuses into the surrounding environment. The transport of vapor involves both the generation and diffusion of vapor. This section will cover the basic principles of vapor generation and diffusion at the solar evaporator interface from the perspective of solution chemistry, along with strategies to enhance vapor diffusion during the ISVG process. Firstly, the chemical potential (μ) reflects the free energy of the molecules in the system, affecting the migration and interaction of the molecules. For the ISVG system in which the liquid (L) and gas (G) phases coexist, the balance of the chemical potential is the central reason to determine whether and how the phase transition process can occur. This means that the chemical potential of each molecule in the liquid phase at a given temperature and pressure must be equal to that of each molecule in the gas phase, and only under such equilibrium conditions do molecules in the liquid not spontaneously transfer to the gas phase and *vice versa*. The conditions for chemical potential equilibrium can be expressed as:

$$\mu_L = \mu_G \tag{40}$$

The liquid-phase chemical potential and the gas-phase chemical potential can be expressed as eqn (41) and (42), respectively:

$$\mu_L = \dot{\mu}_L + RT \ln a_L \tag{41}$$

$$\mu_G = \dot{\mu}_G + RT \ln\left(\frac{P}{P^\ominus}\right) \tag{42}$$

where $\dot{\mu}_L$ and $\dot{\mu}_G$ are the liquid-phase and gas-phase chemical potentials in the standard state, respectively. P is the vapor pressure at the liquid–gas phase transition while $P^\ominus$ is the pressure in the standard state (usually 1 atm.). R is the gas constant, T is the absolute temperature, and a_L is the activity of the liquid phase and can usually be expressed as a mole fraction or concentration. For brine or sea water, activity can be expressed as the effective concentration of water molecules, subject to the influence of a solute such as a salt. In general, it can be expressed by activity coefficient and mole fraction:

$$a_L = \gamma_L x_L \tag{43}$$

where γ_L is the activity coefficient of water in the liquid phase, and x_L is the mole fraction of water in the liquid phase. For non-ideal solutions such as seawater, phage $L < 1$. Substituting eqn (41)–(43) into eqn (40), the vapor pressure can be obtained:

$$P = P^\ominus \cdot e^{\frac{\dot{\mu}_L - \dot{\mu}_G}{RT}} \cdot \gamma_L x_L \tag{44}$$

In an equilibrium system, usually $\dot{\mu}_L = \dot{\mu}_G$, eqn (44) can be simplified as:

$$P = P^\ominus \gamma_L x_L \tag{45}$$

$\gamma_L x_L < 1$, thus $P < P^\ominus$. This result demonstrates that the vapor pressure of sea water is lower than that of pure water, as well as explaining why the evaporation rate in seawater is lower than in the pure water. In fact, a direct method to enhance the evaporation rate in is to reduce the vapor pressure, achievable through rapid vapor condensation and the use of large condensers. In an open system, vapor escapes freely into the environment, maintaining a low vapor pressure at the evaporation interface, thereby sustaining a higher evaporation rate. Conversely, in a closed system, vapor accumulation leads to increased vapor pressure, which significantly slows down the evaporation rate. This is due to the elevated vapor pressure reducing the chemical potential gradient between the liquid and vapor phases, thereby diminishing the driving force for evaporation. For freshwater production through interfacial evaporation, operating within a closed system is often necessary. Hence, a comprehensive understanding and precise control of solution properties, such as vapor pressure and chemical potential, are critical. Mastery of these parameters is essential for optimizing the solar-to-water efficiency of ISVG systems and ensuring their competitiveness with other desalination technologies.

Meanwhile, many inspirations can be obtained when exploring the relationship between the phase diagram (Fig. 12) and the interfacial evaporation process in depth, especially by focusing on the vapor diffusion process. Specifically, the liquid–gas phase transition line, also known as the boiling

This journal is © The Royal Society of Chemistry 2025

Energy Environ. Sci., 2025, **18**, 6366–6437 | **6385**

point curve, in the phase diagram indicates the temperature at which a liquid transforms into a gas at various pressures. For seawater, the phase transition line shifts towards higher temperatures and pressures due to the presence of solutes. By analysing the phase diagram, one can determine the boiling point of seawater at any given pressure. This information is crucial for optimizing the evaporation rate by precisely controlling the heating temperature. Moreover, the phase diagram provides insights into the saturated vapor pressure at different temperatures, which is essential for understanding the impact of temperature gradients on vapor diffusion rates. Higher temperatures correspond to higher vapor pressures, leading to increased diffusion rates. This knowledge can be leveraged to enhance the efficiency of evaporation processes in seawater desalination and other applications.

Vapor diffusion. For effective solar-to-vapor efficiency enhancement, efficient vapor diffusion strategies are essential when vapor is generated at the air–water interface. Vapor diffusion is governed by the mass transfer equation. However, in practical applications, the mass transfer equation may require modification based on specific conditions such as temperature, pressure, and turbulence. The modified mass transfer equation can be expressed as:

$$\frac{\partial \rho}{\partial t} + \nabla \cdot (\rho u) = \nabla \cdot (D \nabla \rho) + S + \nabla \cdot (\rho D_{eff} \nabla T) \tag{46}$$

where $\frac{\partial \rho}{\partial t}$ represents the time rate of change of mass density (ρ), indicating how the density of the substance at a point in space changes over time; $\nabla\cdot$ represents the divergence operator, which is used to calculate the divergence of a vector field such as a flow velocity field (*i.e.*, the difference between the inflow and outflow of a fluid); $\nabla\cdot(\rho u)$ is the divergence of the mass flux density, where u is the velocity vector field of the substance, It measures how mass flow changes per unit volume at a given point; D is the diffusion coefficient representing how readily the substance diffuses through the medium. This term represents the diffusion of mass due to concentration gradients; the source term S accounts for any mass generation or consumption within the system, such as from chemical reactions or phase changes; D_{eff} is

the effective diffusion coefficient, accounting for the influence of temperature gradients (∇T) on mass diffusion. This term reflects the contribution of thermal diffusion to mass transfer. Here, a temperature gradient term $\nabla\cdot(\rho D_{eff} \nabla T)$ is introduced. Based on the above equation, this section will propose four strategies to boost vapor diffusion. These strategies include: (1) increasing the interconnect channel width, (2) reducing the diffusion distance, (3) expanding the vapor diffusion area, and (4) expanding the vapor diffusion boundary. Here, we will introduce research studies toward these four strategies as well as discuss the mechanisms by which these four strategies promote vapor diffusion.

Zhu's group developed a groundbreaking carbon foam with a three-dimensional, interconnected porous structure. This innovative design promotes effective vapor diffusion through convective flow, achieving an impressive evaporation rate of 10.9 kg m^{-2} h^{-1} (Fig. 13a).[122] The increased flow cross-section within the foam allows for a higher vapor velocity (u), which significantly enhances the convection term $\nabla\cdot(\rho u)$. This improvement in vapor velocity consequently accelerates the vapor transport speed. Additionally, the presence of wider channels within the structure reduces the frequency of molecular collisions, resulting in longer mean free paths for the molecules. This change effectively increases the diffusion coefficient (D_{eff}), further optimizing the foam's performance in vapor transport applications. Zhai and co-workers introduced a self-supporting, self-floating three-dimensional solar evaporator (SE) that incorporates porous foam particles and vertically arranged water channels. This innovative design is produced through a continuous directional freezing casting method (Fig. 13b).[123] The foam particles offer significant buoyancy, while the capillary forces in the vertically aligned water channels facilitate rapid vertical water transport. This design ensures stable and efficient vapor generation at the evaporation surface. Notably, the aligned channels reduce the migration distance for both salt ions and vapor from the surface to the bulk water, enhancing vapor diffusion and preventing salt buildup. This, in turn, greatly improves the overall efficiency of the evaporator. According to Fick's First Law, the diffusion flux is given by $J = -D\nabla\rho$. Reducing the diffusion distance, the diffusion flux is directly increased, thereby accelerating the vapor's transport to the target location. This enhanced flux facilitates a more efficient and rapid vapor diffusion process, significantly improving the overall performance of the system. In addition to the strategies already mentioned, expanding the diffusion area of solar evaporators is also a highly effective approach to improve vapor diffusion efficiency. Chen and co-workers designed a functional photo-thermal fabric with programmable 2D and 3D structures to achieve controllable in-plane and out-of-plane solar vapor generation in a scalable, cost-effective, and programmable manner (Fig. 13c).[124] In this system, a large-area polypyrrole (PPy)-modified cotton (PMC) fabric was achieved through a controllable oxy polymerization strategy. Due to the strong wicking effect of the cotton fabrics, water molecules from the bulk water are smoothly transported to the photo-thermal PMC surface, enabling effective solar
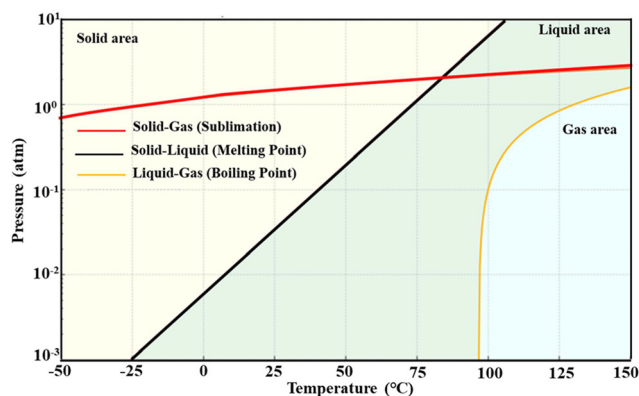
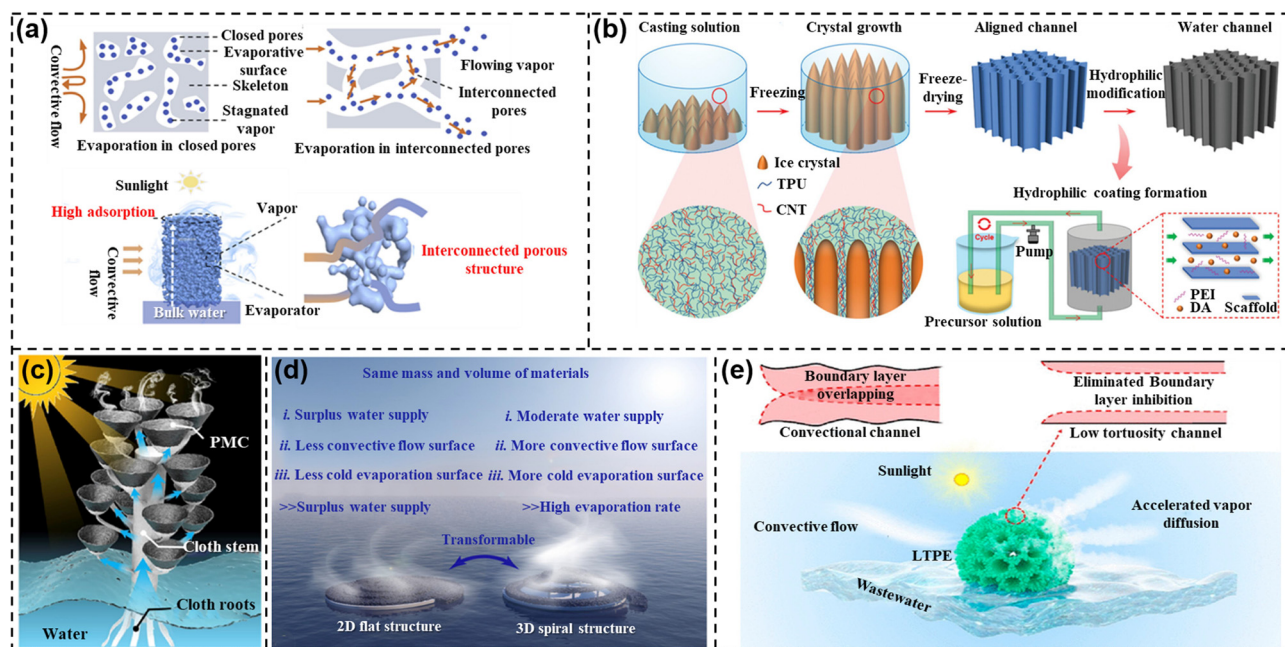**Fig. 12** Simplified phase diagram of seawater.

Fig. 13 Strategies of enhancing vapor diffusion efficiency in the ISVG process. (a) The three-dimensional interconnected porous evaporator increases the vapor diffusion channel. Reprinted with permission.[122] Copyright 2020, Elsevier; (b) the design of aligned water channels inside the solar evaporator enables directional diffusion of vapor. Reprinted with permission.[123] Copyright 2023, Wiley-VCH; (c) schematic of the tunable and programmable 3D hierarchical architectures for expanding the vapor diffusion area. Reprinted with permission.[124] Copyright 2019, Elsevier; (d) schematic illustration of the transformation of a 2D flat to a 3D spiral evaporator for expanding the vapor diffusion area. Reprinted with permission.[125] Copyright 2021, Elsevier; (e) diagram of low-tortuosity channels for breaking through the long-existing vapor diffusion limitation. Reprinted with permission.[126] Copyright 2023, American Chemical Society.

vaporization. Meanwhile, the as-prepared PMC units can serve as building blocks to construct hierarchical 3D structures as a programmable 3D system. The increased surface area further enhances the vapor diffusion efficiency, which is crucial for optimizing vapor transport. Similarly, Xu's group developed a versatile photothermal evaporator using reduced graphene oxide (rGO) and a cellulose sponge, capable of reversible transformation between a 2D flat structure and a 3D spiral configuration (Fig. 13d).[125] The straightforward change from a 2D to a 3D evaporator significantly expands the evaporation surface area, boosting vapor diffusion and improving water transport efficiency. In fact, a larger diffusion area corresponds to an increased vapor generation region, which enhances the source term (S). This results in higher vapor generation rates and stronger concentration gradients ($\nabla\rho$), further driving the diffusion process. Meanwhile, the expanded diffusion area also facilitates more efficient heat transfer, leading to more uniform temperature distributions and improving the effective diffusion coefficient (D_{eff}). These combined effects significantly enhance vapor transport efficiency, providing a solid theoretical and practical foundation for optimizing vapor diffusion in advanced material design, energy systems, and chemical engineering. Indeed, the pore configurations of the majority of solar evaporators are usually designed without a specific pattern, which hinders vapor diffusion and restricts water output. Recently, Xiao and his team were the first to observe the boundary layer inhibition effect (Fig. 13e).[126] They proposed that low-tortuosity channels, which reduce the boundary layer thickness, can effectively overcome the

long-standing limitation of vapor diffusion. To demonstrate their approach, they designed nature-inspired channels with low tortuosity for a solar evaporator. By mitigating the boundary layer inhibition, the diffusion of vapor was improved, facilitating its efficient release from the evaporator. This resulted in an evaporation rate of 16.8 kg m^{-2} h^{-1} under a convective flow of 4.0 m s^{-1} and 1 sun irradiation. This study offers a promising strategy for addressing the boundary layer inhibition effect in solar evaporation systems. Moreover, expanding the vapor diffusion boundary can significantly enhance the overall diffusion process. By providing more boundary conditions, this approach optimizes vapor diffusion near the boundaries, thereby reducing local concentration gradients. Additionally, expanding the boundary can also alter the temperature distribution within the system, making the temperature gradient (∇T) more uniform. This uniformity enhances the term $\nabla\cdot(\rho D_{eff}\nabla T)$, which promotes more efficient diffusion. Thus, the combined effects of optimized boundary conditions and temperature gradients contribute to a substantial improvement in vapor diffusion efficiency.

In summary, increasing the interconnect channel width, reducing the diffusion distance, expanding the vapor diffusion area, and expanding the vapor diffusion boundary each optimize specific parameters of vapor diffusion, such as flow velocity, diffusion coefficient, diffusion flux, and source term. Each strategy employs unique physical mechanisms that, when combined, significantly enhance vapor diffusion efficiency. This comprehensive approach provides a robust theoretical foundation and guidance for practical applications.

Vapor condensation. In ISVG systems, the condensate water is usually the desired product, rather than the vapor itself. Therefore, while some recent studies report extremely high evaporation rates, the efficient condensation of solar vapor remains a critical bottleneck limiting the overall solar-to-water conversion efficiency. This aspect is often overlooked in current research. In practice, solar vapor generally has a relatively low temperature, making it challenging to condense effectively into liquid water, especially when the vapor exists as humidity in the air, as seen in systems where vapor rises and condenses on a transparent cover. We call for future research in ISVG to place more emphasis on this aspect, as high evaporation rates are of little consequence if the vapor cannot be efficiently condensed into liquid water.

This challenge is fundamentally linked to the significant changes in the chemical potential of water molecules during the evaporation and condensation process (Fig. 14). Initially, liquid water absorbs solar energy, causing a temperature rise and an increase in its chemical potential. As the water molecules are transported within the evaporator structure, they become more activated, leading to a further, albeit modest, increase in chemical potential. Once these activated molecules absorb sufficient heat, they transition into vapor, reaching the highest chemical potential (μ_{vap}). As the vapor diffuses, it undergoes thermal exchange with the environment, leading to a decrease in its chemical potential. However, the chemical potential of the vapor remains higher than that of the liquid phase. Eventually, the vapor condenses on a surface, releasing latent heat and reducing its chemical potential to the lowest level (μ_{cs}). The chemical potential of the condensed water is lower than that of the initial liquid water, as the condensation process releases heat and lowers the temperature. For effective condensation and collection of water vapor, the condition $\mu_{cs} < \mu_{vap}$ must be satisfied. When $\mu_{cs} = \mu_{vap}$, a critical condensation temperature ($T_{critical}$) is established. The temperature of the condensation surface (T_{cs}) must be below this critical temperature to ensure that condensation takes place.

In addition to the challenges surrounding efficient condensation, understanding the underlying principles of the gas–liquid phase change is essential for optimizing ISVG systems. As solar vapor generation involves a sequence of complex thermodynamic processes, the phase change from liquid to vapor and *vice versa* plays a pivotal role in the system efficiency.
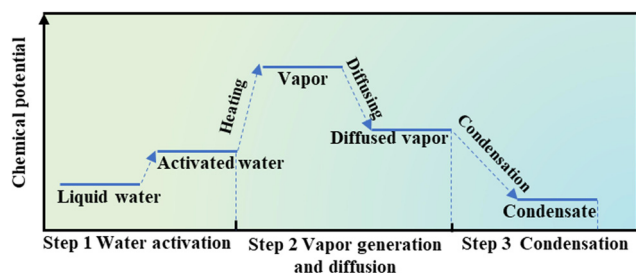

Fig. 14 Chemical potential variation in the vapor generation and condensation process of ISVG technology.

In particular, the gas–liquid phase change occurs in stages, each governed by specific energy transfer and vapor pressure dynamics. Specifically, the gas–liquid phase change operates on the principle that (1) solar radiation heating: solar radiation warms the saline water at the interface of the solar evaporator, which floats within the distiller basin. This process utilizes the solar energy to increase the water temperature, facilitating the evaporation phase. The solar radiation absorbed by the water surface can be quantitatively described using the formula for solar energy absorption by a surface, taking into account the Stefan–Boltzmann law for blackbody radiation:[127,128]

$$Q = A \cdot I \cdot \alpha \cdot t \tag{47}$$

where Q is the energy absorbed (J), A is the surface area exposed to solar radiation (m²), I and α represent the intensity of solar radiation (W m⁻²) and absorptivity of the evaporator surface (dimensionless, between 0 and 1), respectively. t is the solar irradiation time (s). This equation takes into account the area of the evaporator exposed to the sun, the intensity of solar radiation and the proportion of radiation absorbed by the solar evaporator. Adjustments to surface area and material properties can significantly enhance the efficiency of heat absorption, thereby accelerating the evaporation process.

(2) Vapor formation and convection: as the water heats and evaporates, the saturated vapor pressure at the water surface can be described by the Clausius–Clapeyron equation, which is crucial for understanding the phase transition under varying temperatures:[129,130]

$$\ln(P) = -\frac{\Delta H_{vap}}{R}\left(\frac{1}{T}\right) + C \tag{48}$$

where P represents saturated vapor pressure (P), ΔH_{vap} is the heat of vaporization (Joules per mole), R and C represent the universal gas constant and integration constant, respectively, and T is the absolute temperature (K). This equation explains how the vapor pressure increases with temperature, facilitating the upward movement of vapor due to convection. Meanwhile, the condensation process is essentially a thermodynamic process, involving heat transfer and phase change of substances. The condensation rate can be expressed by the following equation:

$$\dot{m} = h_{fg} \cdot A \cdot (P_{sat}(T_s) - P_\infty) \tag{49}$$

where $\dot{m}$ is the mass of water condensed per unit time (kg s⁻¹); h_{fg} is the mass transfer coefficient (kg m⁻² s⁻¹ Pa⁻¹) per unit area and per unit pressure difference; A is the area (m²) of the condensing surface; $P_{sat}(T_s)$ is the saturated vapor pressure (Pa) at the surface temperature T_s; P_∞ is the vapor pressure (Pa) in the environment. Furthermore, conservation of energy (*i.e.* heat balance) in condensation is one of the core principles in the condensation process. This can be expressed by the following equation:

$$Q = m \cdot L \tag{50}$$

where Q represents the heat change in the condensate system; m is the mass of the condensed water, and L is the latent heat of

phase transition of water (the heat released per unit mass when it transitions from a gas to a liquid). A higher latent heat of phase transition means more heat is released per unit mass of water during condensation, which enhances condensation efficiency. The conventional relationship between heat and mass in condensation is described by Fourier's Law and Fick's Law:

$$q = -k\frac{dT}{dx} \qquad (51)$$

where q is the heat flux (heat per unit area per unit time), k is the thermal conductivity of the material composed of the condensate collection device and $\frac{dT}{dx}$ is the direction of the temperature gradient heat flow, which is always transferred from a high to low temperature.

$$J = -D\frac{dc}{dx} \qquad (52)$$

where J is the flux of matter (mass per unit area per unit time), D is the diffusion coefficient, and $\frac{dc}{dx}$ is the concentration gradient. The high thermal conductivity (k) of the material composed of a condensate collection device means that the heat energy is transferred more quickly, which helps to improve the condensation efficiency while a higher diffusion coefficient (D) helps the migration of water vapor in the air and better promotes the condensation process.

(3) Condensation and collection: the heat transfer during condensation can be described by Newton's law of cooling, which gives us a way to quantify the rate at which heat is transferred from the condensing vapor to the cooler surface:

$$Q = h \cdot A \cdot (T_{vapor} - T_{surface}) \cdot t \qquad (53)$$

where Q is the heat transferred (J), h is the convective heat transfer coefficient (W m^{-1} k^{-1}), A is the area of the condensing surface (m^2), and T_{vapor} and $T_{surface}$ represent the temperature of vapor and condensing surface (K), respectively. t is the time period over which condensation occurs (s). This equation explains why enhancing the surface area of the condenser or improving the convective heat transfer coefficient can increase the rate of condensation, effectively speeding up water collection. Upon reaching the cooler glass surface, the vapor condenses into liquid water droplets. These droplets gradually coalesce and, due to gravity, slide down the inclined surface towards a specially designed trough for collecting potable water. The rolling distance of condensate in the roof also affects the efficiency of condensate collection. The growth of the droplet on the surface of the condensate collection device can be described by the rate of change of the droplet radius with time, which reflects the condensation rate:

$$\frac{dr}{dt} = \frac{G}{\rho L} \qquad (54)$$

where r is the droplet radius, t is the time, G is the mass condensed onto the droplet per unit time, ρ is the density of the liquid, and L is the latent heat. The droplet rollover behavior can be understood by considering the surface energy difference

and the gravitational action. The critical rollover radius of the droplet can be estimated by the following equation:[131]

$$r_c = \sqrt{\frac{\sigma}{\rho g \Delta h + 2\sigma/R}} \qquad (55)$$

where r_c is the critical roll-off radius, σ is the surface tension of the liquid, g is the gravitational acceleration, Δh is the height difference between the bottom and top of the wave drop, and R is the contact radius at the bottom of the drop. It is clear that the lower surface tension prompts the droplet to roll more easily and reduces the critical roll radius, which facilitates the rapid removal of condensed water. Meanwhile, the density of the droplet can affect the rollover behavior. Higher density means stronger gravity, which helps the droplets roll off from the condensate collection device. In addition, the condensation efficiency is also affected by the hydrophilicity and hydrophobicity of the collecting device surface. Hydrophilic surfaces improve heat transfer efficiency because water films are able to conduct heat more efficiently, while water droplets easily diffuse and merge to form a film-like water layer, which facilitates rapid water removal. In contrast, on the hydrophobic surface, the condensed water exists in a large drop form, which is not easy to diffuse. The water drops roll off by themselves after reaching a certain size by merging. Such droplet condensation helps maintain a dry condensing surface, although it can impair heat transfer efficiency due to the 'dead zone' created by the gaps between droplets. Modifying the micro/nano structure of the condenser surface can notably influence the behavior of droplet movement by minimizing the contact area between droplets and the surface, thereby reducing adhesive forces and facilitating droplet coalescence.

2.5 Anti-fouling of ISVG

As vaporization at the water–air interface of the solar evaporator and the diffusion of vapor persist, salts in the seawater slowly accumulate on the evaporator surface, reducing solar absorption and obstructing the water transport channels. Meanwhile, microorganisms and bacteria in natural seawater may block the fundamental structure of solar evaporators and reduce their evaporation performance. Therefore, addressing salt and biofouling concerns is critical. Without appropriate anti-fouling measures, salt accumulation and biofouling may occur, obstructing incident light penetration and clogging channels crucial for water conveyance and vapor release, thereby decreasing evaporation efficiency. In this section, we will first introduce some effective strategies currently to combat fouling issues based on relevant scientific principles.[132,133]

2.5.1 Anti-salt deposition. In previous research, managing salt buildup frequently required washing the system with water after each evaporation cycle, which proved inadequate for long-term applications.[134–136] To address this issue comprehensively, three effective strategies (Fig. 15) will be introduced in this section including (1) salt ion rejection, (2) salt ion diffusion and (3) salt ion isolation (detailed in Section 3.2.1). In this section, we will first discuss the mechanism of these three strategies for preventing salt accumulation. Subsequently, we
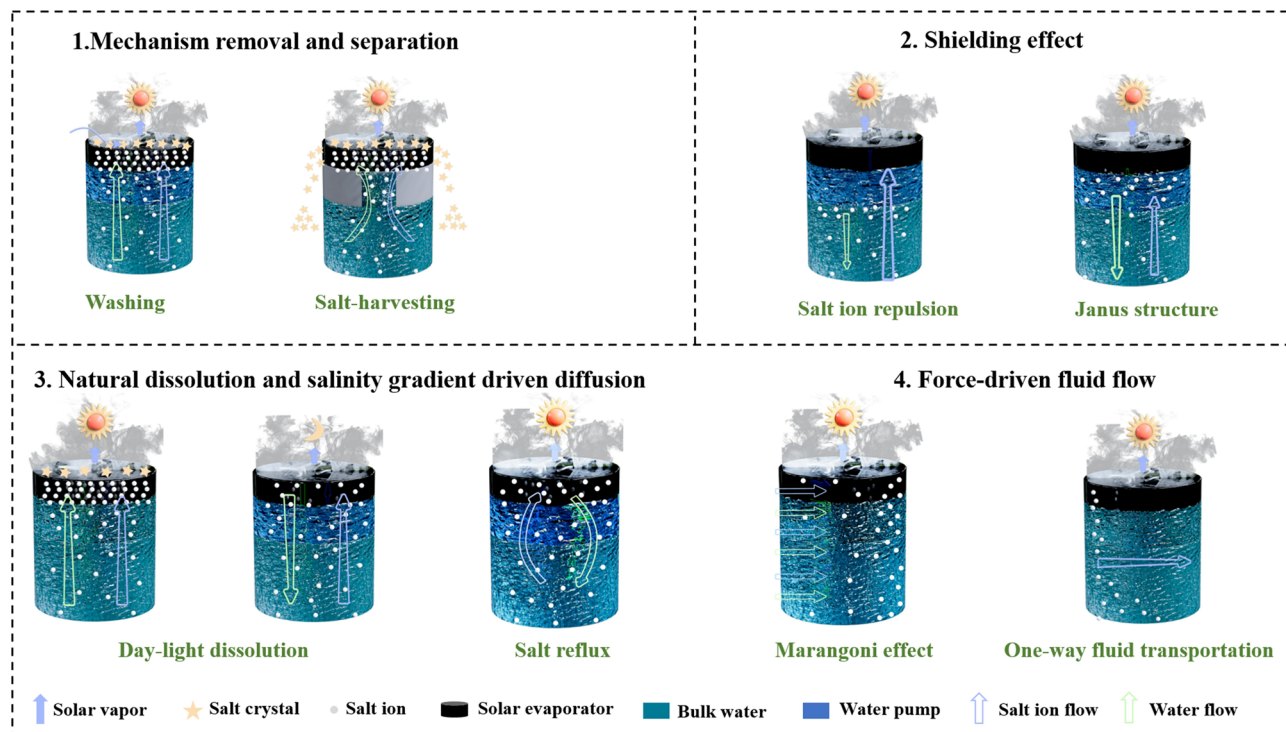
This journal is © The Royal Society of Chemistry 2025

Energy Environ. Sci., 2025, **18**, 6366–6437 | **6389**

Fig. 15 Schematic diagram of comprehensive salt-blocking strategies.

will introduce the recent developments of anti-salt deposition in the ISVG process based on the corresponding mechanism of each strategy.

Salt ion rejection. In the ISVG process, the salt ion blocking performance can be described by the Gibbs adsorption equation:[137]

$$\Gamma = -\frac{1}{RT} \times \frac{\partial \gamma}{\partial \ln C} \qquad (56)$$

where Γ represents the surface excess, which quantifies the amount of a substance adsorbed at the interface relative to its bulk concentration. It is typically expressed in moles per unit area. R is the universal gas constant, representing the factor of proportionality that relates the energy scale in thermodynamics to the temperature scale. T is the absolute temperature (K), which reflects the thermodynamic state of the system. γ represents the surface tension of the interface, quantifying the energetic cost of creating an additional surface area (N m^{-1}). C represents the concentration of the solute (*i.e.* salt ions) in the bulk phase (mol L^{-1}) while $\ln C$ is the natural logarithm of the concentration, providing a dimensionless measure of concentration changes relative to a reference state. This equation describes the relationship between the amount of solute (*i.e.* salt ions) adsorbed at the interface (Γ) and the interfacial tension (γ) and the solute concentration (C). The key here is to understand how the amount of adsorption affects the chemical and physical state of the surface, thereby hindering or promoting salt crystallization. In fact, most of approaches for salt ion blocking are by adjusting the chemical functionalization (*i.e.*,

Janus structure) or physical structure of the surface to change the interfacial tension (γ), thus preventing salts from accumulating and crystallizing. Subsequently, we will introduce recent developments of anti-salt accumulation in the ISVG process.

In 2018, our group developed a novel Janus hydrophilic/hydrophobic nanoporous double-layer membrane designed for efficient and sustainable water desalination (Fig. 16a).[138] The structure incorporated a hierarchical layer with hydrophobic and salt-resistant properties, consisting of nanosphere arrays of Cu_2SnSe_3 (or $Cu_2ZnSnSe_4$), which facilitated improved absorption of solar energy and enhanced water vapor evaporation. This was paired with a hydrophilic filter membrane to ensure a steady water supply and consistent vapor production. The resulting self-floating devices exhibited excellent solar water evaporation performance, achieving an average evaporation rate of 1.657 kg m^{-2} h^{-1} and a photo thermal efficiency of 86.6% under one-sun conditions. In this work, hydrophilic layers in various designs consistently reduce surface tension (γ), facilitating water transport to the evaporative surface and enhancing evaporation rates. Meanwhile, hydrophobic layers act as barriers to salt ion adsorption, effectively lowering the surface excess (Γ). This reduction is vital for maintaining high solar-to-vapor conversion efficiencies, keeping evaporative surfaces free from salt accumulation and preserving photothermal properties. In the same year, Zhu's group reported a flexible Janus absorber, with a top hydrophobic layer of carbon black nanoparticles (CB) coated on polymethylmethacrylate (PMMA) for light absorption, and a bottom hydrophilic polyacrylonitrile (PAN) layer for water transport.[139] The unique Janus structure of the evaporator prevented water from reaching the top

6390 | *Energy Environ. Sci.*, 2025, **18**, 6366–6437

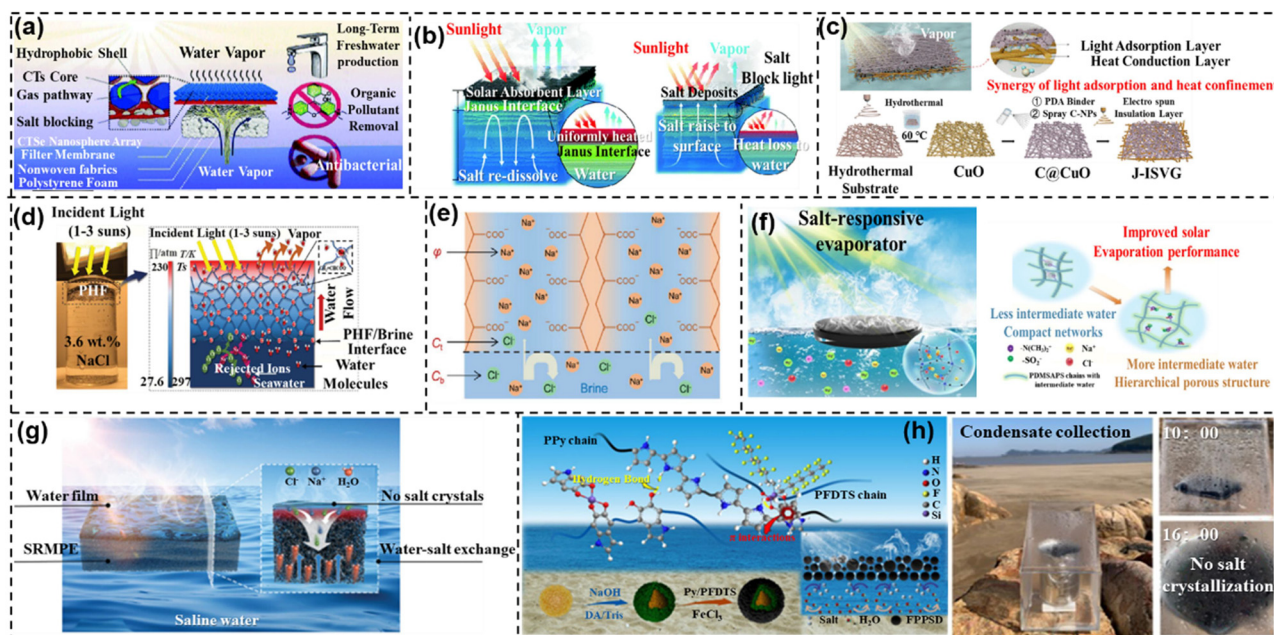This journal is © The Royal Society of Chemistry 2025

Fig. 16 Salt ion blocking strategies in the ISVG process. (a) Schematic illustration of the hydrophilic/hydrophobic nanoporous structure for salt rejection. Reprinted with permission.[138] Copyright 2018, Royal Society of Chemistry; (b) schematic diagram of Janus wood as a salt-resistance evaporator. Reprinted with permission.[140] Copyright 2021, Royal Society of Chemistry; (c) schematic illustration of the Janus interface solar vapor generation and its salt resistance performance. Reprinted with permission.[141] Copyright 2023, American Chemical Society; (d) schematic illustration of the ionic pumping effect for salt resistance. Reprinted with permission.[142] Copyright 2019, Wiley-VCH; (e) schematic diagram of Donnan distribution for salt blocking. Reprinted with permission.[143] Copyright 2021, Wiley-VCH; (f) schematic illustration of a salt-responsive evaporator. Reprinted with permission.[144] Copyright 2022, Wiley-VCH. (g) Schematic diagram of a salt-resistant SRMPE evaporator. Reprinted with permission.[99] Copyright 2024, Wiley-VCH; (h) salt-blocking mechanism of a superhydrophobic sand-based evaporator and its outdoor evaporation performance. Reprinted with permission.[145] Copyright 2024, Elsevier.

hydrophobic photothermal surface, causing salt ions to accumulate only in the bottom hydrophilic layer. Seawater evaporation cycling tests showed that the Janus evaporator maintained consistent performance for over 16 days. These two studies were among the earliest to report a Janus structure for salt blocking in the ISVG process. Moreover, Ren and co-workers reported a wood-based solar evaporator with a Janus structure (Fig. 16b).[140] The Janus wood evaporator features a pronounced asymmetry in surface wettability, with a hydrophobic top layer functioning as a solar absorber, effectively repelling water and resisting salt accumulation, while the hydrophilic bottom layer facilitates rapid water replenishment and provides exceptional thermal insulation. This innovative design achieves an evaporation efficiency of 82.0% for a 20 wt% NaCl solution under one-sun irradiation and exhibits remarkable salt resistance, maintaining a stable performance over 10 consecutive cycles in long-term tests. Furthermore, to evaluate the environmental impact, a life cycle assessment (LCA) was conducted for the first time, highlighting its functional and sustainable potential for off-grid desalination and humanitarian applications. Wood-based evaporators with a Janus structure are well-regarded for their exceptional environmental sustainability. However, a critical challenge of Janus structures is the long-term durability of their hydrophobic coatings. Conventional hydrophobic treatments on wood substrates typically employ low surface energy coatings, which are susceptible to degradation and peeling under

prolonged exposure to saltwater and harsh environmental conditions. This deterioration results in the loss of hydrophobic properties and consequently diminishes the salt resistance of the evaporator. Further research is required to enhance their adaptability for deployment in diverse real-world open water bodies and dynamic environments that may involve severe physical damage, such as cracking, swelling, and biofouling. In addition, a high-efficiency Janus-structured interfacial solar vapor generator (J-ISVG) was created by combining solar photothermal conversion with heat confinement (Fig. 16c).[141] The upper super hydrophilic photothermal layer, made of a carbon black and copper oxide composite membrane, absorbs a wide range of light. The lower layer, consisting of a superhydrophobic nanofiber porous membrane, provides thermal insulation and sustains a stable underwater air cushion, effectively minimizing heat loss from the photothermal layer to the surrounding water. This design achieved a water evaporation rate of 1.88 kg m^{-2} h^{-1} under one-sun illumination over 8 hours of continuous seawater desalination under natural light, showcasing impressive long-term stability. In addition to the material's inherent hydrophobic properties or structure, the unique ion inhibition effect can also be utilized to block salt ions. Chen *et al.* introduced a novel ionic pump effect using polyelectrolyte hydrogel foam (PHF) to achieve this functionality.[142] The inherent ionic strength of the polyelectrolytes, combined with the unique water diffusion behavior within the polymer

This journal is © The Royal Society of Chemistry 2025

Energy Environ. Sci., 2025, **18**, 6366–6437 | **6391**

network, enabled high water flux and exceptional resistance to fouling. This ionic hydrogel was capable of blocking approximately 35% of salt molecules due to its significant ionic strength. While some salt molecules could penetrate the hydrogel, they were retained within the crosslinking network due to electroneutrality. Consequently, using an ionic hydrogel as the water pumping path prevents any salt sediment from forming on the top of the solar evaporator. These structures effectively manage solute concentration (C) by minimizing salt concentration variations at the evaporative interface, thereby preventing salt crystallization. This ensures stable solute concentrations and long-term operational efficiency. Basically, when the local salt concentration surpasses saturation, salt crystallization occurs either within the absorber or on its surface, which hinders light absorption and obstructs water supply pathways, leading to reduced device performance and shorter operational lifetimes. As water evaporates, the salt concentration around the solar absorber rises, leading to inevitable salt crystallization. An effective solution would be to minimize salt ion entry into the water supply layer, thereby preventing salt accumulation on the absorber's surface. The Donnan effect-based approach is an effective method to block salt ions from infiltrating the water supply layer. In this process, counter-ions (e.g., Na^+) are trapped by fixed charges (such as COO^-) within the water supply layer, maintaining electrical neutrality. This creates a high chemical potential that shifts the equilibrium of salt ions between the water supply layer and the surrounding brine. Utilizing this effect, Zhu and colleagues created a salt-resistant solar evaporator with a hierarchical structure that efficiently traps Na^+ ions (Fig. 16e).[143] The elevated chemical potential of confined Na^+ ions creates a Donnan equilibrium, greatly minimizing the diffusion of salt ions into the water supply layer and preventing salt buildup. The hierarchical structure enables the solar evaporator to maintain stable evaporation from high-salinity brine (15 wt% NaCl), achieving a solar-to-vapor conversion efficiency of 80% under one-sun irradiation over extended durations. Recently, salt-responsive polyzwitterionic hydrogels (PZHs) were used as an innovative platform for high-salinity solar desalination (Fig. 16f).[144] Utilizing the distinctive anti-polyelectrolyte effect, PZHs capture salt ions from brine, creating a more hydrated polymer network that boosts solar vapor generation efficiency. These PZHs achieve a remarkable solar evaporation rate of 4.14 kg m^{-2} h^{-1} in 10 wt% brine, roughly 20% higher than in pure water. This work provided insights for the design of next-generation solar desalination systems. However, the mechanism of enhancing solar evaporation rates need to be further explored. Most recently, Li's group developed a flexible single-layer salt-rejecting monolithic porous evaporator (SRMPE) that combines a free-floating capability near the water surface with high water flux to achieve effective salt rejection (Fig. 16g).[99] This system demonstrated self-cleaning properties, removing 33 wt% of salts from seawater (3.5 wt% salinity) within 1.25 hours and maintaining superior salt rejection during 12 hours of continuous evaporation in highly concentrated brine (25 wt% salinity) under one sun irradiation without any salt crystallization. Similarly, a novel superhydrophobic sand solar (FPPSD) evaporator with a core–shell structure was developed by Chen and co-workers through interface functionalization, enabling continuous and efficient photothermal desalination (Fig. 16h).[145] The FPPSD evaporator demonstrated exceptional salt-resistance stability, maintaining continuous photothermal performance even after 96 hours of evaporation under 3-sun irradiation with a 10 wt% saline solution, ranking among the best in reported studies. Additionally, it exhibited remarkable environmental durability, retaining its water transport capacity after 30 days under harsh conditions, highlighting its potential for robust and long-term applications. These advancements highlight the transformative potential of innovative materials and structural designs in overcoming salt accumulation challenges and achieving stable, long-term performance in photothermal desalination systems.

In summary, the commonality in advanced solar desalination systems lies in their ability to manipulate surface tension, solute concentration, and surface excess synergistically. By strategically employing hydrophilic and hydrophobic layers, these systems achieve high evaporation rates, efficient salt rejection, and prolonged stability.

Salt ions redissolving. In ISVG processes, salt recirculation is employed to prevent or reduce the salt accumulation on evaporator surfaces or within the equipment. As discussed earlier, salt diffusion occurs naturally due to the salinity gradient between the evaporation surface and the bulk water, preventing salt buildup to some extent. However, under high evaporation rates or extended operation, diffusion alone may not suffice to mitigate salt crystallization effectively. To address these challenges, advanced approaches, including active salt recirculation (salt ions reflow) and structural optimization of evaporators, have been developed to physically displace concentrated brine and enhance salt transport efficiency. These strategies involve adjusting the solution's flow to physically displace the fluid, thereby diluting local salt concentrations and mitigating issues related to crystallization and salting out. This mechanism can be effectively described using a comprehensive convection-diffusion-evaporation framework. The corresponding theoretical equations incorporate the interactions among fluid dynamics, mass transfer, and heat transfer, providing a robust basis for understanding and optimizing salt recirculation in evaporative systems:

$$\frac{\partial C}{\partial t} + \vec{u} \cdot \nabla C = D\nabla^2 C + S - R \qquad (57)$$

where C denotes the salt concentration; $\vec{u}$ represents the fluid velocity vector; D is the diffusion coefficient of the salt; ∇^2 symbolizes the Laplacian operator indicative of the diffusion term; S represents sources or sinks of salt, typically zero in this context; R indicates the reduction in salt concentration due to evaporation, which is a crucial term directly related to evaporation rate and local concentration. The fluid velocity ($\vec{u}$) controls the convective transport of salt, and high flow velocities help to promote the uniform distribution of salt ions in the evaporator and reduce local concentration. When designing the evaporator structure, the internal flow channel should be optimized to

6392 | *Energy Environ. Sci.*, 2025, **18**, 6366–6437

This journal is © The Royal Society of Chemistry 2025

increase the flow rate, especially in areas where salt can easily accumulate, so as to improve the reflux efficiency of salt ions. This explains why solar evaporators with directional channel structures usually have excellent salt reflux properties. R represents the rate at which salt concentration in the solution increases per unit time due to water evaporation. This parameter reflects the direct impact of the evaporation process on salt concentration and is a critical factor to be closely monitored in the design and operation of evaporation systems. The following equation can be used to describe the salt concentration change (R) during evaporation:

$$R = \frac{\Delta C}{\Delta t} = \frac{E \cdot C_{\text{int}}}{V - E \cdot \Delta t} \qquad (58)$$

where ΔC is the change in salt concentration, Δt is the time interval, E is the evaporation rate (the volume of water evaporated per unit time), C_{int} is the initial salt concentration, and V is the total volume of the solution at the beginning. Based on the above equations, we will introduce some examples of salt ion diffusion back in the ISVG process.

In 2019, a self-regenerating solar evaporator with remarkable anti-salt deposition properties was reported by Hu's group (Fig. 17a).[146] This solar evaporator operates through a precisely engineered artificial channel array integrated into a natural wood substrate. During solar evaporation, salt concentration gradients develop between the millimeter-sized drilled channels, which have lower salt concentrations, and the micro-sized natural wood channels, which hold higher salt concentrations. These gradients facilitate spontaneous salt exchange through 1–2 μm pits, diluting the salt in the micro-sized wood channels. The drilled channels, due to their high hydraulic conductivity, function as effective salt-rejection pathways, rapidly exchanging salt with the bulk solution. Specifically, the temporal change in salt concentration $\left(\frac{\partial c}{\partial t}\right)$ is minimized through the careful design of artificial channel arrays. The millimeter-sized drilled channels with high hydraulic conductivity facilitate rapid advection ($\vec{u} \cdot \nabla C$) effectively transporting salt from areas of higher concentration in the micro-sized natural wood channels to areas of lower concentration. This high advection rate is crucial for maintaining low local salt concentrations and
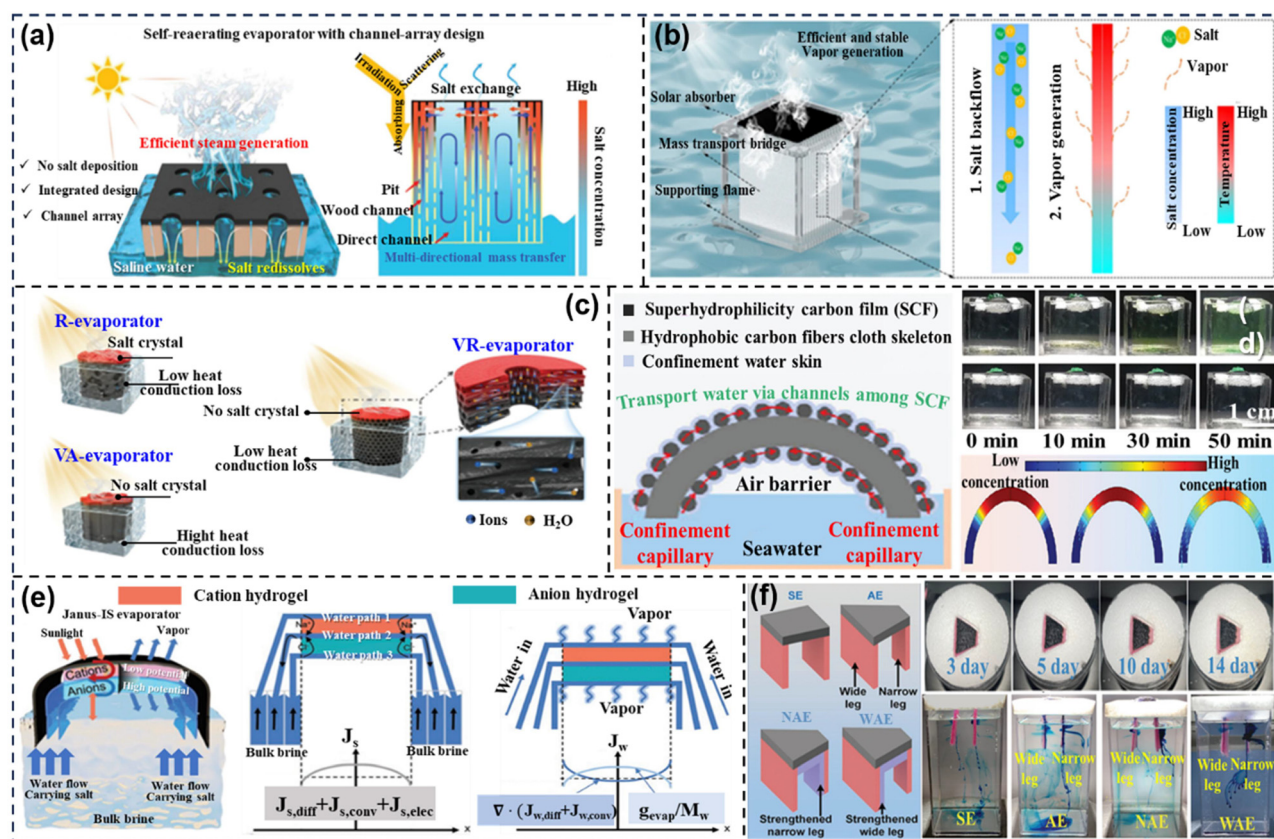

Fig. 17 Salt reflux during the ISVG process. (a) Schematic illustration of the salt reflux solar evaporator design. Reprinted with permission.[146] Copyright 2023, Wiley-VCH; (b) schematic diagram and working principles of the 3D salt redissolve solar evaporator. Reprinted with permission.[147] Copyright 2022, Springer Nature. (c) Schematic description of salt ions redissolving in three distinct evaporator structures. Reprinted with permission.[148] Copyright 2022, Wiley-VCH; (d) diagram and photograph of the water skin effect for dissolving salt crystals. Reprinted with permission.[149] Copyright 2023, Wiley-VCH; (e) schematic diagram of a Janus-IS hydrogel evaporator for redissolving salt ions. Reprinted with permission.[150] Copyright 2023, Wiley-VCH; (f) schematic of symmetrical and various asymmetrical structures of evaporators, along with their salt resistance performance. Reprinted with permission.[151] Copyright 2023, Wiley-VCH.

preventing crystallization, thus enhancing the desalination efficiency. Meanwhile, the diffusion coefficient (D) plays a pivotal role in promoting the uniform distribution of salt within the evaporator. The high diffusion rate in the micro-sized wood channels ensures that salt is evenly dispersed and transferred through the 1–2 μm pits to the drilled channels. This efficient diffusion process mitigates concentration peaks and supports continuous dilution, maintaining the evaporator's functionality over extended periods. Finally, the rate of change of salt concentration ($\Delta C/\Delta t$) is optimized by increasing the efficiency factor (E) and removal rate (R). The high E and R facilitated by the drilled channels ensures effective and fast salt rejection, maintaining low internal salt concentrations (C_{int}) and preventing performance degradation. In conclusion, the strategic manipulation of these parameters—minimizing $\frac{\partial c}{\partial t}$, maximizing $\vec{\mu} \cdot \nabla C$ and D, enhancing R and E—enables the real-time self-regeneration of the evaporator. Similarly, Han and co-workers developed a rationally designed 3D salt-rejection evaporator that ensures stable and efficient water evaporation by optimizing salt backflow (Fig. 17b).[147] The key feature of this evaporator is a series of vertically aligned mass transfer bridges (MTBs) with numerous hydrophilic microchannels. Experimental results show that this 3D evaporator operates continuously without salt buildup, even when processing high-salinity water (e.g., 12–14 wt% NaCl solutions and concentrated brine from RO facilities), achieving a high vapor generation rate of approximately 1.64 kg m^{-2} h^{-1}. Additionally, scaled-up versions of these solar evaporators were tested on a rooftop and in the Red Sea, demonstrating their practical applicability. A daily water collection rate of around 5 L m^{-2} and a solar-water collection efficiency exceeding 40% were achieved, surpassing the previous record of approximately 22%. Water transport in carefully engineered 3D evaporators is inherently linked to heat conduction losses, resulting in a trade-off between thermal localization and salt resistance. Zheng and colleagues created a 3D hydrogel evaporator with vertical radiant channels, successfully addressing this ongoing issue and achieving high-rate, stable solar desalination of high-salinity water (Fig. 17c).[148] Both experimental and numerical simulations show that the unique hierarchical structure—consisting of large vertical vessel channels, radiant vessels, and porous walls—promotes efficient self-salt discharge while reducing longitudinal thermal conductivity. Under one-sun illumination, this innovative design achieves exceptional performance, with an evaporation rate of 3.53 kg m^{-2} h^{-1}, handling 20 wt% salinity, and sustaining continuous evaporation for 8 hours. In this work, the term $\frac{\partial c}{\partial t}$ represents the temporal change in salt concentration, which is minimized by the evaporator's design, ensuring a steady-state concentration profile. The advection term ($\vec{\mu} \cdot \nabla C$) is crucial, as the high hydraulic conductivity ($\vec{\mu}$) of the vertical vessel channels facilitates efficient advective transport of salt from high-concentration regions (radiant vessels) to low-concentration regions (vertical vessel channels), driven by steep concentration gradients (∇C). The diffusion term ($D\nabla^2 C$) highlights the role of diffusion in homogenizing

salt concentrations within the microchannels, enhanced by the hierarchical structure that increases the effective diffusion coefficient (D). Notably, the removal rate equation further illustrates the importance of the efficiency factor E and internal concentration C_{int} in achieving high-rate salt removal. High hydraulic conductivity and optimized vessel design significantly boost E, facilitating rapid and continuous salt exchange. Maintaining a low C_{int} in the vertical vessel channels and managing higher concentrations in the radiant vessels are crucial for efficient recirculation. The overall volume V and time interval Δt are optimized to ensure continuous and effective salt removal. In summary, this innovative approach showcases a significant advancement in the field of solar desalination, offering practical solutions for high-salinity water treatment and setting a new benchmark for salt-free systems. Similarly, Wang and co-workers proposed a synergistic strategy that integrates the water skin effect and double-sided evaporation *via* an arched evaporator to address salt deposition (Fig. 17d).[149] This method involves applying super hydrophilic carbon films, derived from metal–organic frameworks (MOFs), onto a hydrophobic carbon-fiber cloth (CC), and shaping the assembly into an arch-like form. The resulting structure, with a hydrophobic core and hydrophilic shell, traps an ultrathin water layer (30–150 μm) on its surface, effectively simulating a "skin." The arched evaporator takes advantage of the water skin effect and co-evaporation from both the inner and outer surfaces, achieving an excellent evaporation rate of 2.87 kg m^{-2} h^{-1} (20 wt% NaCl) under one-sun illumination. Furthermore, the arch creates an air gap between the surface and the foam underneath, minimizing contact with the bulk water and reducing heat loss. This cost-effective and efficient method offers new insights into preventing salt deposition during solar evaporation. Conventional salt-resistant strategies primarily work by boosting water flow to prevent salt buildup. Although effective, these methods result in significant heat loss due to increased water convection, which in turn hampers water evaporation and reduces water production in real-world applications. Li's group recently introduced an ion-transfer engineering method that employs a Janus ion-selective (Janus-IS) hydrogel solar evaporator. This novel approach employs ion-electromigration (IEM) to eliminate salts, effectively overcoming the constraints of water-convection-based salt removal and minimizing heat loss (Fig. 17e).[150] Ion-selective hydrogels create a concentration gradient between the evaporation interface and the internal water pathways, leading to the downward migration of cations and the upward movement of anions. This differential ion movement generates an internal electric field that facilitates the expulsion of counterions, enhancing the salt resistance of the system. Notably, no salt accumulation or degradation in performance is observed during seven days of continuous exposure to high-intensity irradiation, even when treating brine with a 15 wt% salt concentration. The separate pathways for salt ion removal and water flow decouple salt removal from water convection, significantly minimizing additional heat loss. Unlike the complex fabrication process of previous solar evaporators, Li's group introduced a bi-layer asymmetric solar evaporator inspired by

6394 | *Energy Environ. Sci.*, 2025, **18**, 6366–6437

This journal is © The Royal Society of Chemistry 2025

electronic diodes. This design features a trapezoidal evaporation surface and a broad leg-strengthened water supply pathway, enabling directional salt ion migration. Additionally, the evaporator can be readily fabricated through the partial carbonization of commercially available coconut fiber cloth (Fig. 17f).[151] This approach leads to an evaporator that sustains a high and stable solar evaporation rate, even in high-salinity brine and intense irradiation conditions. The mechanism behind its exceptional salt resistance was confirmed through ion migration tests, visual color assessments, and numerical simulations, showing that the asymmetric structure of the evaporator generates a steeper salt concentration gradient in the narrow leg, promoting ion migration. This directionally selective ion migration strategy differs from the traditional one-leg water supply method by using water supplied from both legs. Exhibiting diode-like characteristics, the evaporator maintains stability over 14 days under 14 wt% NaCl and 4 suns irradiation, achieving an impressive evaporation rate of 7.28 kg m^{-2} h^{-1}. In this work, the distinct water supply paths in the wide and narrow legs result in differential distributions of $\vec{u}$ and ∇C, enhancing ion migration and thus salt resistance. Specifically, the high flow velocity in the wide leg ($\vec{u}$) and the corresponding low flow velocity in the narrow leg create a significant concentration gradient (∇C), facilitating efficient ion diffusion and migration according to Fick's law. These findings offer valuable insights for future developments in sustainable and efficient desalination technologies, providing a promising direction for practical applications.

In summary, key principles for enhancing salt backflow and desalination efficiency involve minimizing the temporal change in salt concentration $\left(\dfrac{\partial c}{\partial t}\right)$ and maximizing advection ($\vec{u}\nabla C$)

and diffusion ($D\nabla^2 C$). High hydraulic conductivity ($\vec{u}$) in specific channels ensures efficient advective transport of salt from high-concentration regions to low-concentration regions, driven by steep concentration gradients (∇C). This process prevents local salt crystallization and maintains low internal salt concentrations (C_{int}), critical for sustained performance. Additionally, optimizing the diffusion coefficient (D) within the evaporator ensures uniform salt distribution, mitigating concentration peaks and promoting continuous dilution through hierarchical structures and microchannels. Meanwhile, the design must balance overall volume (V) and time interval (Δt) to ensure persistent and effective salt rejection, minimizing performance degradation. Future developments should continue to focus on optimizing these parameters to achieve scalable, efficient, and sustainable desalination technologies.

2.5.2 Anti-biofouling. Considering the presence of massive micro-organisms and bacteria in natural seawater, the adhesion and formation of biofilms on photothermal evaporators have been commonly observed in long-term operation, which can lead to the obstruction of the functional structure of the photothermal evaporator and impair evaporation performance. Therefore, the advancement of solar evaporators equipped with anti-biofouling properties is becoming an inevitable and significant trend.

Drawing inspiration from plant transpiration and natural photosynthesis, Yang's group fabricated a hybrid hydrogel by integrating MXene/LSC nanohybrids with polyvinyl alcohol (PVA) and chitosan (CS), thereby bestowing bifunctional capabilities to the material (Fig. 18a).[152] This novel choice of materials and design allows the MLH evaporator to efficiently treat brine and wastewater, reaching a solar-to-vapor conversion efficiency of 92.3% and an impressive photodegradation
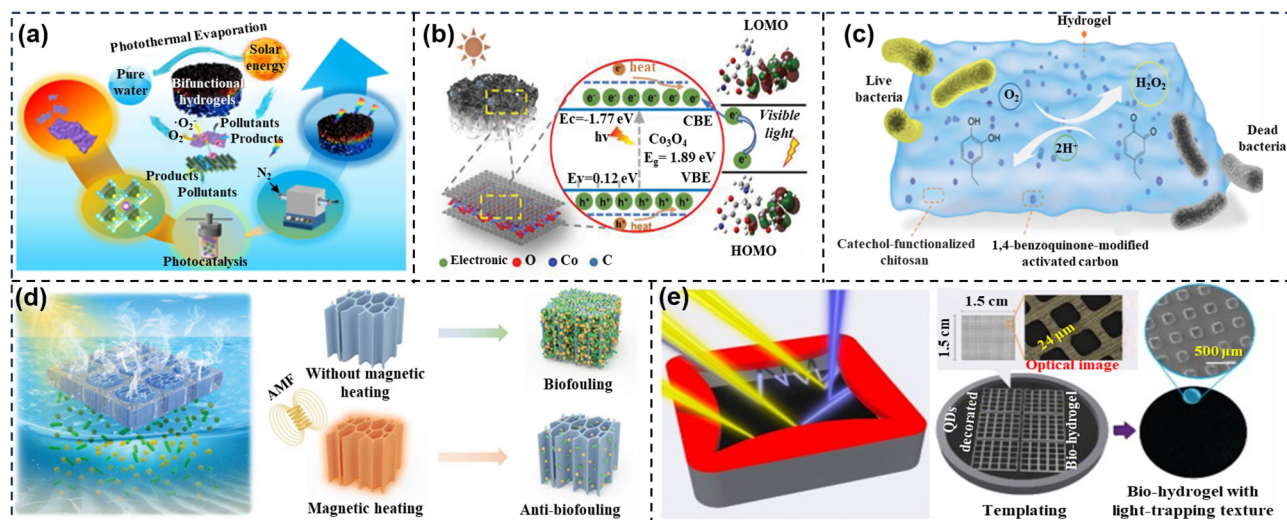

Fig. 18 Summary of anti-biofouling strategies on an evaporator surface. (a) Schematic illustration of a Ti$_3$C$_2$T$_x$ MXene based hydrogel for simultaneously vapor generation and photocatalytic pollutant degradation. Reprinted with permission.[152] Copyright 2021, Elsevier; (b) photocatalytic mechanism of solar evaporator toward pollutant degradation. Reprinted with permission.[153] Copyright 2023, Wiley-VCH; (c) schematics of sustainable solar vapor generation and anti-bacterial hydrogels (ABHs) for water disinfection and purification. Reprinted with permission.[154] Copyright 2021, Wiley-VCH; (d) schematic of the magnetic-heating mediated anti-biofouling strategy. Reprinted with permission.[155] Copyright 2023, Wiley-VCH; (e) schematic illustration of the light-trapping texture with excellent solar vapor generation and antibacterial performance. Reprinted with permission.[156] Copyright 2023, Elsevier.

efficiency (97.2%) for eliminating tetracycline hydrochloride (TC). Similarly, Zhou and co-workers developed a fully functional solar vaporization device (SVD) utilizing organic–inorganic hybrid nanocomposites (CCMs-x). These devices demonstrate efficient photothermal properties, enabling multitargeted interfacial reactions for simultaneous sewage degradation and saline water desalination (Fig. 18b).[153] The photothermal effect of CCMs-x induces localized heating at the interface, promoting surface-dominated catalysis and vaporization. The CCMs-x SVD achieves a solar water vapor generation rate of 1.41 kg m^{-2} h^{-1} (90.8%) and over 95% pollutant removal within 60 minutes under one-sun illumination, attributing to the customized microenvironments within the system. Apart from the coupling of interfacial evaporation technology and photocatalysis, reactive oxygen species (ROS) generation is also an effective method for biofouling resistance. Yu's group synthesized antibacterial hydrogels (ABHs) by forming a chitosan network functionalized with catechol groups (CCS), combined with activated carbon particles anchored with quinones (Fig. 18c).[154] The oxidation of catechol groups, induced by O$_2$ in both air and water, gradually releases H$_2$O$_2$ from the hydrogel, serving as a broad-spectrum disinfectant. Meanwhile, quinone-modified activated carbon (QAC) particles within the hydrogel interact with various biological sulfhydryl groups, such as those found in proteins and metabolites, thereby enhancing the bactericidal effect. These antimicrobial biohybrids (ABHs) can be directly applied to untreated water in tablet form, achieving a 5–6 log reduction (>99.999%) of *Bacillus subtilis*, *Escherichia coli* and *Pseudomonas aeruginosa* within 60 minutes, without the need for any external energy. Recently, Lu and co-workers introduced a magnetic heating strategy to combat biofouling in solar vapor generation using a magnetic silk fibroin (SF) scaffold with dual-heating capabilities (Fig. 18d).[155] Under one-sun illumination, the solar-heated top surface of the magnetic SF scaffolds facilitate water evaporation at a rate of 2.03 kg m^{-2} h^{-1}, while biofilm formation occurs within the unheated inner channels. Upon exposure to an alternating magnetic field (AMF), the entire magnetic SF scaffold is uniformly heated, raising the internal temperature to mitigate biofouling within the water transport channels. As a result, the magnetically heated scaffolds maintain stable water evaporation rates after exposure to *S. aureus* and *E. coli*, preserving 93.6–94.6% of their initial efficiency. Furthermore, the magneto-heated scaffold effectively prevents biofouling in natural lake water, retaining 99.5% of its original performance. Meanwhile, Tsang *et al.* introduced a novel light-trapping texture on the surface of a reduced graphene oxide (rGO)/agar–agar hydrogel, which possesses antibacterial and antifouling properties due to its coating of TaTe$_2$ quantum dots (QDs) (Fig. 18e).[156] These tellurium QDs have a high affinity for DNA sulfur proteins, enhancing the permeability of bacterial membranes and achieving elimination rates of up to 96.49% for *S. aureus* and 97.58% for *E. coli*. Notably, the primary advantage of interfacial evaporation is its elimination of the need for additional energy supplies and transport mechanisms. Leveraging this process to concurrently remove biological contaminants without incurring extra energy consumption offers a distinct and significant developmental edge.

3. Current application of the ISVG system

ISVG represents a groundbreaking technology developed over the past decade. Initially aimed at sustainable clean water production through desalination to address global water shortages, its applications have since significantly expanded across various essential sectors. This section will summarize the applications of the ISVG system, mainly focusing on vapor condensation,[157–159] salt ion isolation and extraction,[160,161] and energy generation,[162–164] with the aim of fostering a deeper understanding of its diverse potential and impact (Fig. 19).

3.1 Vapor condensation-oriented ISVG applications

Apart from the highly efficient evaporation rate, effective vapor condensation is also a critical step for ISVG systems due to the fact that the ability for harvesting purified water efficiently determines the application boundaries of ISVG systems, as ISVG applications aim to obtain clean water. In this section, we will discuss the mechanism of how to improve the vapor condensation rate based some relevant scientific principles, providing guidance for the design of condensation devices. Subsequently, we will introduce applications of ISVG systems toward vapor condensation including saline water desalination, wastewater purification, water desorption in atmospheric water harvesting (AWH), solar ocean agricultural cultivation and solar sterilization.

3.1.1 Saline water desalination.
The condensation process, which transforms vapor back into liquid water, is fundamentally tied to thermodynamic principles such as changes in the chemical potential of water molecules, temperature gradients and the material properties of the condensing surfaces. However, despite the impressive evaporation rates achieved in recent studies, the collection of this vapor remains a critical challenge, primarily due to the difficulty in effectively condensing low-temperature vapor, which often exists as humidity in the air.
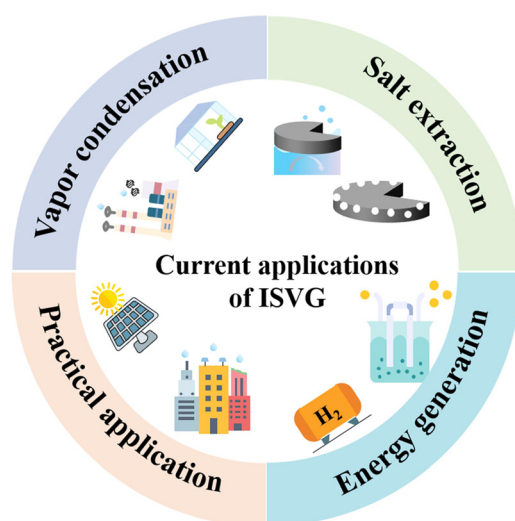

Fig. 19 Summary of current applications of ISVG technology.

Building on this understanding, the subsequent section delves into the design and optimization of condensation devices that are vital for the collection of distilled water in ISVG systems. To facilitate the transition from vapor to liquid, condensation devices must not only ensure efficient thermal exchange but also accommodate the physical collection of liquid water through carefully engineered surfaces. In particular, advancements in condenser designs, such as the incorporation of smooth conical or dome-shaped roofs, play an essential role in enhancing water collection by promoting condensation on the inner surfaces of the chambers. The following sections explore the various strategies employed in saline water desalination systems, with a focus on the critical role of vapor condensation devices in optimizing the efficiency of these systems under natural sunlight. To better illustrate these processes, two distinct condensation scenarios will be discussed (Fig. 20): one where vapor rises (single-stage) and another where vapor is directed downward (single-stage and multi-stage systems). The following discussion explores the various strategies employed in saline water desalination systems, with a focus on the critical role of vapor condensation devices in optimizing the efficiency of these systems under natural sunlight.

Microcystis pre-treatment for ISVG water purification systems. To address the challenges posed by organic contaminants like microcystins from algal blooms, pre-treatment strategies are essential before applying ISVG technology in wastewater and seawater purification. While ISVG shows promise in desalination and wastewater treatment, it cannot degrade complex organic contaminants on its own. Therefore, integrating ISVG with complementary technologies, such as photocatalysis, is crucial. Photocatalysis is an effective, environmentally friendly method for degrading microcystins and other organic pollutants. Though studies combining ISVG with photocatalysis for

algal bloom remediation are scarce, photocatalysis has proven successful in degrading microcystins in aquaculture wastewater. Photocatalysis works by activating a catalyst under light irradiation to generate reactive oxygen species (ROS) that damage algal cell walls, leading to the degradation of microcystins and disruption of algal growth. This process not only controls algae but also detoxifies the surrounding water. By integrating photocatalysis with ISVG, we can enhance water purification and provide a sustainable solution for environments affected by algal blooms. For example, Fan's group synthesized an Ag_2MoO_4/TACN floating photocatalyst using an oscillatory impregnation method for the removal of *Microcystis aeruginosa* (*M. aeruginosa*), as shown in Fig. 21a.[168] The Ag_2MoO_4/TACN@LF floating photocatalyst, when loaded at 6 g L^{-1}, caused significant damage to the membrane permeability, photosynthetic system, antioxidant system, and metabolic activity of the algae cells within 4 hours under visible light irradiation. Chen and co-workers, on the other hand, developed an efficient powder photocatalyst, Bi_2O_3@Cu-MOF, by coupling bismuth oxide with copper-based metal–organic frameworks (MOFs). The photocatalyst was successfully immobilized on melamine sponge (MS) using sodium alginate as a binding agent, resulting in a floating photocatalyst, MS/Bi_2O_3@Cu-MOF, which was used to inactivate *M. aeruginosa* under visible light (Fig. 21b).[169] When the loading amount was 0.4 g, the MS/Bi_2O_3@Cu-MOF exhibited good photocatalytic activity, achieving a 74.462% inactivation rate of *M. aeruginosa* after 120 hours. However, these studies are limited by the photocatalyst's weak visible-light response and the rapid recombination of photogenerated electron–hole pairs, indicating that further improvements in performance are necessary. To address this issue, Xu and co-workers synthesized a Z-scheme AgBr/NH_2-MIL-125(Ti) (AMNT) composite material with excellent visible light absorption properties using a co-precipitation

Fig. 20 Fundamental design principles of single-stage and multi-stage solar distillers. (a) Schematic diagram of a vapor condensation device. (b) Vapor upward condensation and collection devices (single stage). Reproduced with permission.[165] Copyright 2024, Wiley-VCH; (c) water droplets collection device (single stage). Reproduced with permission.[166] Copyright 2023, Wiley-VCH; (d) and (e) vapor downward condensation device. (d) Reproduced with permission.[167] Copyright 2024, Springer Nature; (e) reproduced with permission.[63] Copyright 2024, Royal Society of Chemistry.

This journal is © The Royal Society of Chemistry 2025

Energy Environ. Sci., 2025, **18**, 6366–6437 | **6397**

Fig. 21 Potential microcystis pre-treatment strategies for ISVG water purification systems. (a) Schematic diagram of potential pathways for the photocatalytic inactivation of *M. aeruginosa* by Ag₂MoO₄/TACN@LF floating photocatalyst under visible light exposure. Reprinted with permission.[168] Copyright 2023, Elsevier; (b) mechanism diagram of *M. aeruginosa* inhibition by MS/Bi₂O₃@Cu-MOF. Reprinted with permission.[169] Copyright 2024, Elsevier; (c) possible degradation mechanism of *M. aeruginosa* by ANMT photocatalysts; rep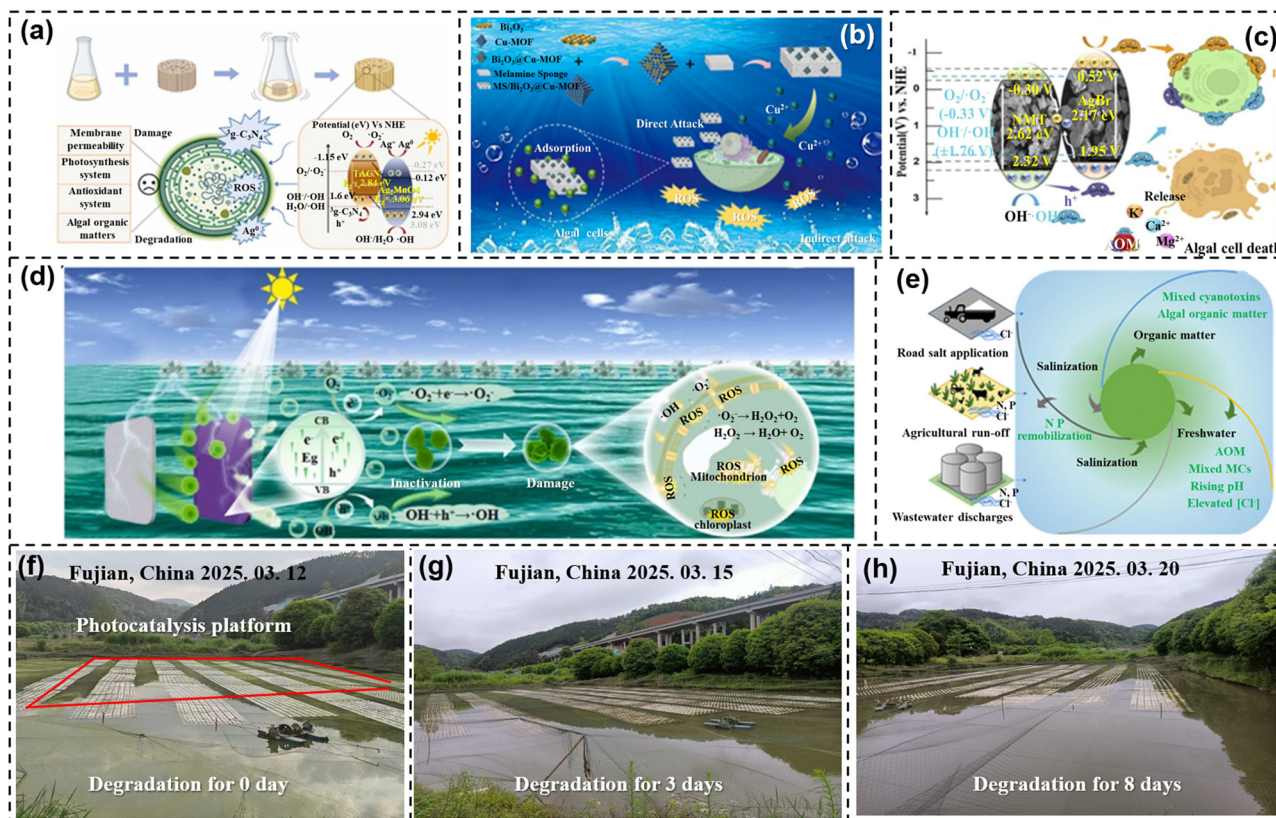rinted with permission.[170] Copyright 2024, Elsevier; (d) mechanism diagram of algae cell inactivation under R-TENG-assisted photocatalysis. Reprinted with permission.[171] Copyright 2024, Elsevier; (e) UV/chlorine treatment process for degrading harmful microcystins (MCs) in drinking water. Reprinted with permission.[172] Copyright 2025, American Chemical Society; (f) engineering application of *in situ* photocatalytic modules for aquaculture wastewater treatment; (g) photocatalytic module treatment and aesthetic design; (h) degradation process over 8 days. (f)–(h) Our group work, Product Copyright@Xi'an Qinshengfeng Tech. Co. Ltd., Photo copyright@author Yawei Yang, All rights reserved.

method (Fig. 21c).[170] This composite effectively inactivated *M. aeruginosa*. After 180 minutes of visible light irradiation, the degradation efficiency of chlorophyll a by AgBr/NH₂-MIL-125(Ti) was 98.7%, which was significantly higher (by factors of 3.20 and 36.75) compared to the degradation efficiencies of AgBr and NH₂-MIL-125(Ti), respectively. After five cycles of reuse, the removal efficiency remained at 91.1%. The experimental results indicate that superoxide radicals ($\bullet O_2^-$) are the primary reactive oxygen species involved in the photocatalytic process. The photocatalytic reaction altered the morphology and surface charge of the algal cells, suppressed their metabolic activity, and disrupted their photosynthetic and antioxidant systems.

The aforementioned studies demonstrate the effectiveness of visible light-driven photocatalysis in degrading microcystins and mitigating algal blooms. Similarly, UV-assisted degradation offers an alternative method for enhancing the breakdown of these organic pollutants, leveraging high-energy UV light to activate photocatalysts and improve the degradation efficiency of harmful contaminants. Nie and co-workers proposed a rotating triboelectric nanogenerator (R-TENG), as a self-powered bias

for photocatalysis to enhance algae removal efficiency (Fig. 21d).[171] The R-TENG collects waste wave energy from the coagulation pool, converting it into a stable direct current voltage (31 V) and current (27 μA). TiO₂ nanotubes (TNT) used as the anode in the TENG-assisted photocatalysis system achieved complete algae inactivation (>97%) after 7 hours of reaction, marking a 13.9% improvement compared to conventional photocatalysis. This enhanced performance is attributed to the improved generation of reactive species (*e.g.*$\bullet O_2^-$ and $\bullet OH$). During algae inactivation, these reactive species disrupted the algae cells' photosynthetic activity, antioxidant system and cell membranes. Recently, Dionysiou and co-workers demonstrated that UV-assisted degradation is a highly effective method for breaking down microcystins and other organic pollutants associated with harmful algal blooms (Fig. 21e).[172] It highlights the ability of UV light to activate photocatalysts, thereby generating reactive oxygen species (ROS) such as $\bullet OH$ and superoxide anions ($\bullet O_2^-$), which are crucial for disrupting the cellular structures of algae and organic contaminants. Through these mechanisms, the degradation efficiency of microcystins is

6398 | *Energy Environ. Sci.*, 2025, **18**, 6366–6437

This journal is © The Royal Society of Chemistry 2025

significantly improved, achieving high inactivation rates. Building upon the fundamental principles of photocatalysis, recent advancements have increasingly focused on integrating photocatalytic systems into practical engineering applications. As seen in Fig. 21f, our group has designed an *in situ* photocatalytic treatment module for aquaculture wastewater, which has been applied in practical settings. The treatment module is used for a single aquaculture pond, with an area of approximately 100 m^2, and the photocatalytic module covers an area of 20–40 m^2. The initial deployment of the photocatalytic platform on the first day of treatment in an aquaculture pond. At this stage, the water is visibly turbid, and a dense algal bloom is clearly evident, contributing to the degradation of water quality. Subsequently, a noticeable reduction in the algal bloom is observed (Fig. 21g). The photocatalytic treatment process begins to take effect, with a clear decrease in algae concentration and a corresponding improvement in water clarity. The visible reduction of the algae signifies the photocatalytic module's ability to degrade organic matter, including algae and associated toxins, through the generation of reactive oxygen species (ROS) under light exposure. By day 8, the water quality has improved dramatically, becoming visibly clear to the naked eye (Fig. 21h). The algal bloom has been significantly reduced, and the water is now free of the turbidity that characterized the initial stages. This outcome demonstrates the effectiveness of the *in situ* photocatalytic treatment in mitigating algal blooms and restoring the natural clarity of the water.

In summary, while ISVG provides an efficient solution for water purification and desalination, its limitation in degrading organic pollutants, such as those found in algal blooms, necessitates the integration with additional technologies. Photocatalysis, when coupled with ISVG, offers a promising approach by utilizing solar-driven chemical reactions to degrade organic pollutants, including algal toxins. The combination of solar-thermal and photocatalytic processes enables the *in situ* degradation of contaminants while generating clean water, thereby enhancing the efficiency of both pollutant removal and water recovery. For example, photothermal materials serving as both light absorbers and photocatalytic surfaces facilitate the destruction of harmful algal toxins while producing water vapor for condensation. Future advancements will focus on refining photocatalytic materials, optimizing their interaction with ISVG systems, and developing scalable, cost-effective solutions for real-world applications. The development of broad-spectrum photocatalysts and surface modifications to improve charge separation will significantly enhance system performance. Ultimately, integrating ISVG with photocatalysis offers a sustainable solution to address the dual challenges of water purification and pollutant control, particularly in regions impacted by harmful algal blooms.

Transparent top cover for forward vapor collection. After pretreatment, seawater can be directly used for interfacial evaporation to collect freshwater. In 2018, our group demonstrated a system capable of freshwater collection during continuous daytime operation (Fig. 22a).[138] Under natural sunlight, vapor was produced from the membrane surface and subsequently condensed and collected at the bottom. After four hours of operation, approximately 15 mL of freshwater was harvested, corresponding to 45.2% of the theoretical maximum yield. To minimize light refraction caused by prism structures, condensation devices with smooth conical or dome-shaped roofs have been widely adopted.[173–179] Yu and co-workers have reported the use of a hierarchically nanostructured gel, 20 cm in diameter, assembled within a desiccator-like condensation chamber for seawater desalination under natural sunlight (Fig. 22b).[115] Under an average solar flux of 0.7 kW m^{-2}, a daily clean water yield of 18–23 L m^{-2} was obtained over 12 hours, with a lab-measured open evaporation rate of 3.2 kg m^{-2} h^{-1}. The purified water had a resistance value of 1.4 MΩ, significantly higher than that of the original seawater (0.08 MΩ) and domestically supplied water (1 MΩ), indicating the high quality of the collected water. Similarly, Tang and co-workers developed a large-scale outdoor solar desalination device based on N, O dual-doped carbon foam (NCF) for freshwater production (Fig. 22c).[180] The daily freshwater yield per unit area is 6.3 kg, which is sufficient to meet the daily water consumption needs of two adults. However, in the studies mentioned above, condensation collection devices operate in a closed space at atmospheric pressure to gather condensed water. As the saturated vapor pressure within the sealed space increases, the efficiency of condensed water collection gradually decreases (as mentioned in Section 2.4.4). Fan's group established a low-pressure environment inside the collection chamber by linking a portable, manually operated vacuum pump to the left-side outlet on the top cover (Fig. 22d).[68] Throughout the evaporation process, the internal vacuum level is monitored in real-time *via* a gauge positioned on the right. To sustain the low-pressure state after reaching the target pressure, a vacuum switch is integrated into the system.

The majority of articles in the field focus primarily on improving the efficiency of solar-to-vapor conversion, while the efficiency of vapor-to-water conversion has received little attention. However, high evaporation rates alone are insufficient if the condensed vapor cannot be effectively collected as liquid water. Therefore, greater emphasis should be placed on optimizing condensation and collection processes, as these are equally critical for achieving practical solar-to-water conversion efficiency. To optimize the efficiency of saline water desalination systems, several key engineering strategies should be considered: (1) energy absorption: enhance solar energy absorption by using high photothermal conversion materials and optimizing surface absorptivity. Structural designs like multi-layered or textured surfaces can increase the effective exposure area and ensure uniform water distribution, minimizing thermal losses. Integrating solar concentrators or trackers is advised for regions with low solar irradiance. (2) Evaporation process: maintaining elevated temperatures within the evaporator, incorporating heat recovery systems, and using efficient photothermal materials are critical. Multi-stage evaporation systems should be optimized for temperature distribution across stages, and heat exchangers should be integrated to recover latent heat during condensation, allowing for

This journal is © The Royal Society of Chemistry 2025

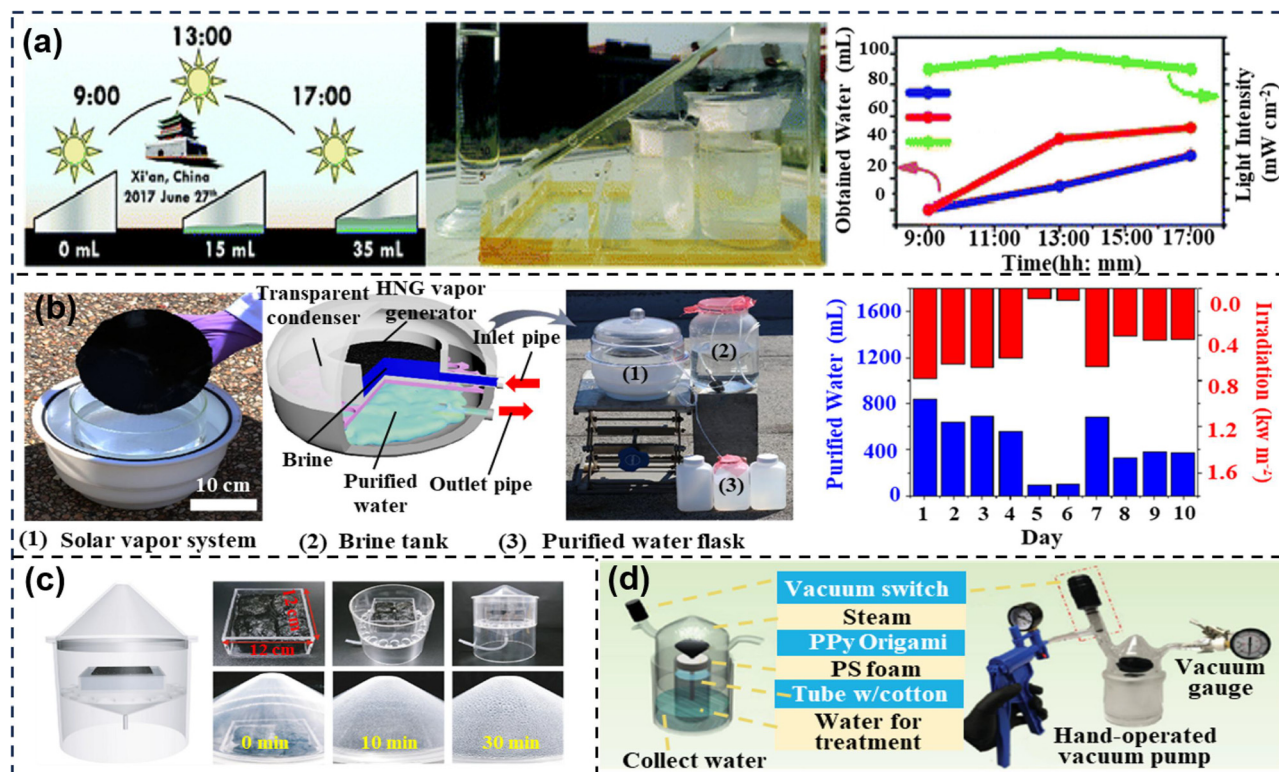*Energy Environ. Sci.*, 2025, **18**, 6366–6437 | **6399**

Fig. 22 Transparent top cover for forward vapor collection. (a) Optical photograph and diagram of water collection rate of the all-in-one solar distillation setup under natural sunlight.[138] (b) Schematic and photograph of the water receiver with the yield of purified water for 10 days with the corresponding average solar irradiation data. Reprinted with permission.[115] Copyright 2018, Springer Nature. (c) Scheme and photographs of a large-scale outdoor solar desalination device. Reprinted with permission.[180] Copyright 2022, Wiley-VCH. (d) Schematic and digital photographs of the designed low-pressure solar steam-collection system. Reprinted with permission.[68] Copyright 2019, Wiley-VCH.

preheating of saline water. Multi-effect distillation (MED) systems offer further energy efficiency by sequentially recovering latent heat and reducing energy consumption, and (3) condensation process: improving condensation efficiency can be achieved by increasing the surface area through extended surface designs (*e.g.*, layered or corrugated surfaces). By focusing on material selection, surface design, temperature control, and heat recovery strategies, the overall performance of saline water desalination systems can be significantly improved, providing practical and efficient engineering solutions.

Side and bottom collector for invert vapor collection. The top cover, serving as the primary path for light irradiation, may have its sunlight blocked or scattered by vapor and water droplets. In contrast to traditional condensation designs, Bo's group developed a novel solar vapor gap membrane distillation (SVGMD) technique that integrates self-directed water transport, localized heating, and membrane separation from the feed solution (Fig. 23a).[181] They have engineered a standalone, multifunctional light absorber using a graphene array to heat a thin water layer passing through graphene nanochannels. This method achieves a high solar-to-water efficiency of 73.4% under 1 sun illumination, a clean water collection rate of 82.3%, excellent anti-fouling properties, and stable permeate flux during continuous 72-hour operation. Additionally, a scaled-up

system for treating oil/seawater mixtures under natural sunlight has been developed, producing purified water at a rate of 92.8 kg m^{-2} per day. Similarly, Qu's group has developed an innovative solar desalination system (Fig. 23b).[182] In this design, the photothermal surface with high thermal conductivity is arranged vertically for optimal light energy absorption. A seawater reservoir with an inclined superhydrophobic metallic surface is installed at the upper rear section to deliver water. During desalination, seawater is directed to the backside of the photothermal layer for evaporation. The chilled seawater in the tank promotes efficient vapor condensation on the sloped metal surface, thereby mitigating solar energy losses associated with droplet-induced reflection and scattering on the photothermal interface. This synergistic effect results in an excellent water production rate of 1.95 kg m^{-2} h^{-1}, nearly matching the open environment evaporation rate of 2.21 kg m^{-2} h^{-1}. Differing from the previously mentioned forward and side vapor collection methods, Zhu and co-workers designed an inverted-structured single-stage solar water purifier (Fig. 23c).[183] The solar evaporator system features a selective absorber at the top and a honeycomb-structured water condenser at the bottom, constructed from hydrophobic nanostructured copper. This inverted system architecture effectively reduces optical losses caused by vapor condensation and simultaneously enhances heat transfer and condensation performance. Consequently, the

6400 | *Energy Environ. Sci.*, 2025, **18**, 6366–6437

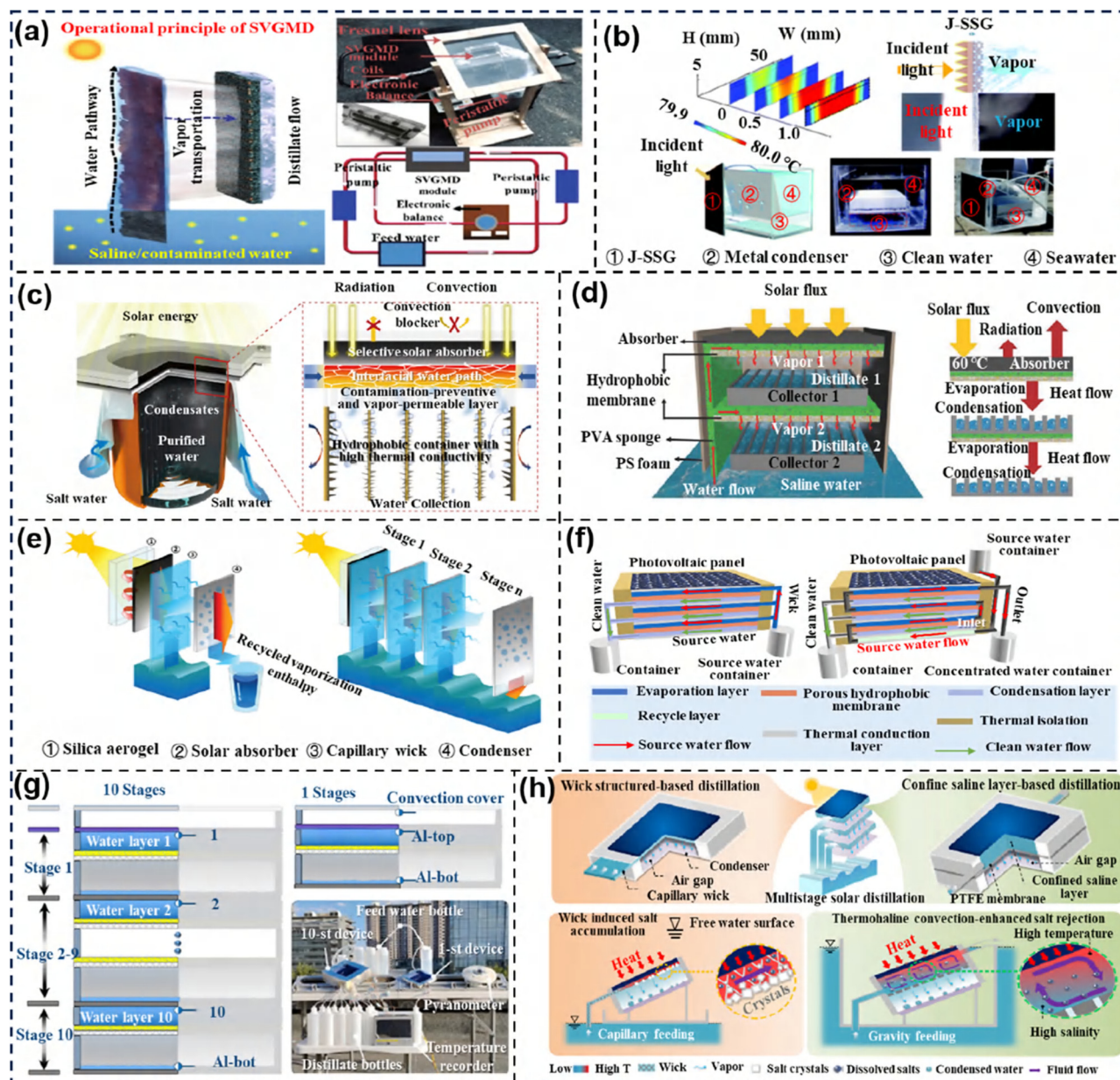This journal is © The Royal Society of Chemistry 2025

Fig. 23 Side and bottom collector for invert vapor collection with latent heat recovery. (a) Schematic of solar vapor gap membrane distillation (SVGMD) for back vapor collection. Reprinted with permission.[181] Copyright 2019, Springer Nature; (b) schematic diagram and photograph of a Janus-interface solar-steam generator (J-SSG) for back vapor collection. Reprinted with permission.[182] Copyright 2021, Royal Society of Chemistry; (c) schematic diagram and mechanism of single-stage invert-structured device for vapor collection. Reprinted with permission.[183] Copyright 2021, Elsevier; (d) schematic of an inverted multi-stage solar distillation system. Reprinted with permission.[184] Copyright 2018, Wiley-VCH; (e) diagram of a thermally-localized multistage solar still (TMSS) for vapor collection. Reprinted with permission.[185] Copyright 2020, Royal Society of Chemistry; (f) schematic illustration of multistage integrated photovoltaics-membrane distillation (PV-MD) devices. Reprinted with permission.[186] Copyright 2019, Springer Nature; (g) diagram of the outdoor platform of a salt-resistant multi-stage solar still for vapor collection. Reprinted with permission.[187] Copyright 2023, Springer Nature; (h) schematic diagram of the thermohaline convection-enhanced multi-stage solar distillation device. Reprinted with permission.[188] Copyright 2023, Elsevier.

device achieves a water harvesting rate of 1.063 kg m^{-2} h^{-1} and an overall solar-driven water collection efficiency of 70% within a single-stage purification setup. Despite these advancements, continuous solar desalination processes often face a gradual decline in evaporation and condensation rates over time. This happens because single-stage condensation devices rely on the release of latent heat through interaction with the surrounding

environment. As a result, the temperature within the condensation chamber rises, which in turn hinders the continuous phase transitions. To address this issue, multistage condensation systems have been developed to recover the lost latent heat and effectively cool the condensation chamber. The concept of a multistage solar evaporation–distillation system was first introduced by Zhou and his team in 2018 (Fig. 23d).[184] Their design

featured a two-level desalination device with a light-absorbing layer as the top cover. A polyvinyl alcohol (PVA) sponge, known for its high-water wicking capability, was used as the evaporator and was closely attached to the back of the light-absorbing layer. To prevent seawater leakage, a hydrophobic membrane made of poly (vinylidene fluoride-*co*-hexafluoropropylene) (PVDF-HFP) was spin-coated onto the back of the PVA sponge. During the evaporation process, the produced vapor was directed downward to condense on the collector, which subsequently acted as the thermal source to facilitate water evaporation in the next stage. Remarkably, this two-level device achieved a water productivity rate of 1.02 kg m^{-2} h^{-1}, surpassing the vapor generation rate under 1 sun irradiation in an open system. In outdoor trials, it showed remarkable water productivity of 3.67 kg m^{-2} over 8 hours, with a salt rejection rate surpassing 99.75%. After its initial implementation, the multistage solar evaporation–distillation design saw substantial improvements to boost the water production rate. The configuration of the multistage distiller reported by Asinari and co-workers was illustrated in the same year.[159] They used a photothermal layer encased by a convection reducer as the top cover to capture light energy. The subsequent evaporation and condensation units were sandwiched between two aluminum plates (12 × 12 cm^2) with high thermal conductivity. A hydrophilic microfiber layer was affixed to the backside of the aluminum plate, serving as the evaporator. To prevent potential salt contamination of the condensed freshwater, an air gap or hydrophobic membrane was utilized to separate the evaporation and condensation zones. In the solar distillation process, the latent heat released during water condensation was reutilized to sustain evaporation across successive stages. Under controlled laboratory conditions, a water production rate of 3 kg m^{-2} h^{-1} was achieved with a 10-stage system. To enhance heat and mass transfer in a multistage condensation system, Wang and colleagues carefully optimized the device's geometry. They modified several parameters, such as the evaporator size, air gap thickness, number of condensation stages, and sidewall thermal insulation (Fig. 23e).[185] Their optimized 10-stage condensation device achieved an exceptional energy efficiency of 385% and a clean water production rate of 5.78 kg m^{-2} h^{-1}. Remarkably, coupling systems that integrate multistage distillation devices on the backside of photovoltaic (PV) panels have been reported by Wang's group (Fig. 23f).[186] A photovoltaics-integrated membrane distillation (PV-MD) system has been designed to consistently yield clean water from seawater at rates above 1.64 kg m^{-2} h^{-1}, while preserving a high solar-to-electricity conversion efficiency (>11%) under standard one-sun illumination. This improvement in freshwater production is realized by integrating a multi-stage membrane distillation (MSMD) unit behind the solar cell, enabling successive recycling of condensation latent heat at each stage. Meanwhile, this design also leveraged the waste heat generated during the photovoltaic electricity generation process, utilizing it as the photothermal component to drive the production of clean water. While solar-driven reverse distillation combined with thermal localization has recently demonstrated impressive solar-to-water conversion efficiency, effective methods for salt

rejection and discharge remain limited. Recently, Xiong and co-workers developed solar distillation devices utilizing millimeter-scale reverse-evaporating water layers, achieving both high solar-to-water efficiency and effective salt rejection in solar desalination processes. Two passive operation modes, gravity and discharge, demonstrated solar-to-water conversion efficiencies of 59.1% and 60.6%, respectively, with 3.5 wt% brine. This system also maintained 47.4% efficiency when desalting high-salinity (21 wt%) water without salt crystallization. For broader applications, the authors tested ten-stage desalination systems based on reverse-evaporating layers, achieving a total efficiency of 354% and successful salt rejection at each stage (Fig. 23g).[187] Furthermore, inspired by thermohaline convection, Xu and co-workers presented a solar-powered multistage membrane distillation system with exceptional salt-resistance (Fig. 23h).[188] By using a confined saline layer as the evaporator, robust thermohaline convection was induced to prevent salt buildup and improve heat transfer. The ten-stage device achieves impressive solar-to-water efficiencies ranging from 322% to 121% for salinities between 0 and 20 wt% under one-sun illumination. It exhibited exceptional resistance to salt accumulation, maintaining 180 hours of continuous desalination of 20 wt% concentrated seawater. These two studies offered a groundbreaking approach to effective salt rejection in multistage devices, representing a significant advancement in the field of sustainable desalination technology. In addition to the experimental results mentioned above, Wang's group conducted numerical simulations to investigate the impact of device stages, sidewall insulation, and geometric configuration on overall efficiency.[189] Their findings revealed that increasing the number of stages to enhance efficiency is limited by an upper threshold determined by the device's geometric configuration, with the initial stages contributing most significantly to vapor production and marginal benefits diminishing in subsequent stages. Adding sidewall insulation was shown to further improve overall efficiency by increasing the amount of recoverable energy. For each fixed device width, under the constraint of capillary length, an optimized unit stage thickness was found to achieve the device's maximum overall efficiency, with this optimized thickness and corresponding peak efficiency increasing with the device width. Interestingly, the numerical simulation results indicated that a device with a unit stage thickness of 0.25 cm, a width of 15 cm, and appropriate insulation could achieve a solar standstill efficiency exceeding 700%, highlighting a significant gap between current achievable efficiencies and theoretical potential. This work provides valuable theoretical guidance for future research in the field.

Although the collection rate of condensate in single-stage evaporation is currently low, addressing the issues of optical loss and condensate reflux could significantly enhance the practical value of this simple and widespread system structure. While multistage evaporation technology shows characteristics of industrial design and has improved condensate collection efficiency, it faces numerous challenges, including difficulty in monitoring configurations and a lack of economic cost-effectiveness. These obstacles present significant barriers to its development. Meanwhile, whether in single-stage or

6402 | *Energy Environ. Sci.*, 2025, **18**, 6366–6437

This journal is © The Royal Society of Chemistry 2025

multistage condensate collection systems, the reported data on water collection are limited to small-scale devices monitored over short periods and specific conditions, which do not accurately reflect realistic freshwater production across various weather conditions. Furthermore, the fabrication cost of condensation devices remains a significant concern.

3.1.2 Wastewater purification

Non-volatile pollutants in wastewater. In solar desalination processes, liquid source water undergoes a phase transition to separate clean vapor from inorganic salts. Therefore, ISVG presents a promising potential for wastewater purification.[190,191] In practical industrial wastewater systems, contamination includes complex mixtures of chemical pollutants, organic compounds, suspended solids, volatile matter, bacteria, and microorganisms. However, current research has primarily concentrated on the evaporation of laboratory-simulated wastewater. For example, Li and colleagues developed a solar-powered purifier that enables high-efficiency water purification and production (Fig. 24a).[192] This meticulously designed structure achieves a collection rate of 4.2 kg m^{-2} h^{-1}, with ionic rejection exceeding 99% under one-sun illumination. This work represents one of the earliest reported cases of water disinfection based on ISVG technology. Wang and co-workers developed a 3D-MoS$_2$-PEG sponge that serves as an effective absorbent for mercury removal (Fig. 24b).[193] Additionally, the exhausted materials were functionalized with a hydrophilic PEG layer and reused in solar steam evaporation to produce freshwater. The resulting evaporator demonstrated excellent evaporation rates of approximately 1.45 kg m^{-2} h^{-1} under sunlight, producing freshwater with Hg^{2+} levels within the WHO drinking water standard of 0.001 mg L^{-1}. These results offer an environmentally friendly approach to recycling hazardous adsorbents for water purification. Recently, Zhu and co-workers developed an interfacial solar steam-driven reverse osmosis/nanofiltration system that generates high pressure to push water molecules through a filtration membrane, effectively separating them from ions (Fig. 24c).[194] This device achieves a water production rate of up to 81 kg m^{-2} h^{-1} under 12-sun illumination. Additionally, a theoretical model suggests considerable potential to enhance freshwater output by optimizing the device's thermal insulation and expansion ratio. This research opens new avenues for designing highly efficient, miniaturized, or decentralized drinking water systems. However, environmental pollution and the presence of complex contaminants in water pose significant challenges to obtaining clean water using previous methods. To address this issue, Qu and co-workers developed a solar-powered clean water extractor using a graphene/alginate hydrogel (GAH) with exceptional resistance to contaminants and superior antifouling capabilities (Fig. 24d).[195] This GAH demonstrates excellent selectivity in water transport, rejecting more than 99.5% of volatile organic compounds, over 99.3% of ions (Na$^+$, Mg^{2+}, K$^+$, and Ca^{2+}) and 100% of non-volatile organic compounds and bacteria. Furthermore, the GAH inhibits oil adhesion with a contact angle greater than 140° underwater, deactivates almost 100% of surface bacteria, and prevents salt crystallization. Thanks to its exceptional adaptability to various environments, this GAH can efficiently

convert complex surface water into clean, drinkable water. This study plays a crucial role in advancing solar-powered clean water harvesting technologies and addressing challenges in polluted water environments. In fact, the rate of fresh water production remains limited due to the substantial latent heat required for water evaporation and the efficiency of condensation.

Volatile organic compounds removal. In addition to non-volatile pollutants, water-soluble volatile organic compounds (VOCs), which pose significant environmental and health risks, are among the most challenging contaminants to treat in wastewater. Many VOCs are harmful to human health, even at low concentrations, and their removal from water is challenging due to their high volatility and low concentration in aqueous solutions. Although the ISVG system is effective in purifying water contaminated with non-volatile substances, it struggles with VOCs. These compounds tend to evaporate and condense together with water, complicating the purification process.[196,197] As a result, there is an urgent need for innovative and well-considered design in ISVG systems to effectively remove VOCs, guaranteeing the production of clean and safe drinking water.[198,199] We examine a system in which VOCs are transferred from the liquid phase to the gas phase through evaporation at the interface. The mass transfer rate of VOCs from the liquid to the gas phase can be characterized by the mass transfer coefficient (k_L) and the concentration gradient of VOCs at the interface. The mass transfer rate ($\dot{m}$) is expressed as

$$\dot{m} = k_L \cdot A \cdot (C_0 - C_i) \tag{59}$$

where $\dot{m}$ is the mass transfer rate (kg s^{-1}); k_L is the liquid-phase mass transfer coefficient (m s^{-1}); A is the area of the liquid–gas interface (m^2). C_0 and C_i represent the initial concentration of VOCs in the liquid phase and the concentration of VOCs at the interface (kg m^{-3}), respectively. We consider the change in concentration of VOCs in the bulk liquid phase over time. The mass balance for VOCs in the liquid phase can be written as:

$$\frac{dC}{dt} = -\frac{\dot{m}}{V} \tag{60}$$

where C is the concentration of VOCs in the bulk liquid phase (kg m^{-3}); t is the evaporation time (s); V is the volume of the liquid phase (m^3). Substituting eqn (59) into eqn (60), results in:

$$\frac{dC}{dt} = -\frac{k_L \cdot A \cdot (C_0 - C_i)}{V} \tag{61}$$

For simplicity, we assume that C_i is negligible compared to C_0 (*i.e.*, $C_i \approx 0$), which is reasonable if the concentration of VOCs in the gas phase is very low compared to the liquid phase. Thus:

$$\frac{dC}{dt} \approx -\frac{k_L \cdot A \cdot C}{V} \tag{62}$$

This is a first-order linear differential equation. To solve it, we separate the variables and integrate. We integrate both sides from the initial concentration C_0 at $t = 0$ to C at the time t:

$$\int_{C_0}^{C} \frac{1}{C} dC = -\frac{k_L \cdot A}{V} \int_{0}^{t} dt \tag{63}$$

This journal is © The Royal Society of Chemistry 2025

Energy Environ. Sci., 2025, **18**, 6366–6437 | **6403**

Fig. 24 Removal of non-volatile pollutants in wastewater by ISVG technology. (a) Diagram and performance of a plant leaf-inspired purifier for clean water production driven by solar energy. Reprinted with permission.[192] Copyright 2019, Springer Nature; (b) schematic diagram of the reclaimable adsorbents for water purification driven by ISVG.[193] (c) Schematic of the solar steam driven-reverse osmosis/nanofiltration (SSD-RO/NF) system for water production under various solar power densities over six cycles. Reprinted with permission.[195] Copyright 2023, Springer Nature; (d) schematic and performance of graphene/alginate hydrogel (GAH) in high selective pure water extraction and multi-effective antifouling capacity driven by solar energy. Reprinted with permission.[194] Copyright 2023, Springer Nature.

Therefore, the concentration of VOCs in the liquid phase at any time t is:

$$C = C_0 \exp\left(-\frac{k_L \cdot A \cdot t}{V}\right) \qquad (64)$$

Meanwhile, the removal efficiency E can be defined as the fraction of VOCs removed from the liquid phase:

$$E = 1 - \frac{C}{C_0} \qquad (65)$$

Substituting eqn (64) into eqn (65), the removal efficiency of VOCs can be obtained:

$$E = 1 - \exp\left(-\frac{k_L \cdot A \cdot t}{V}\right) \qquad (66)$$

This derivation and analysis provide a comprehensive understanding of how various factors influence the removal efficiency of VOCs during interfacial evaporation. In this case, Yu's group developed a novel super water-extracting gel (SWEG) based on highly hydrophilic alginate, designed to enable effective volatile organic compound (VOC) control and water purification *via* direct solar-driven distillation. Unlike other water-absorbing hydrogels, the SWEG uniquely retains all contained water at the molecular level (Fig. 25a).[200] The SWEG can extract water from VOC solutions due to the stronger stability of hydrogen bonds over the dipole–dipole interactions between water and VOC molecules. By separating VOCs from the evaporation interface, the SWEG effectively prevents contamination of the collected vapor. Under one-sun irradiation, it demonstrates outstanding removal efficiencies, eliminating more than 99.0% of phenol and 99.99% of trichloroethylene. In this work, the highly hydratable alginate matrix significantly enhances the mass

transfer coefficient (k_L). This enhancement is due to the gel's ability to maintain strong hydrogen bonds with water molecules, resulting in excellent water retention capacity and facilitating the efficient transfer of VOCs from the liquid phase to the gas phase. Another crucial parameter is the area of the liquid–gas interface (A). The unique molecular-level water retention capability of the SWEG increases the effective surface area available for mass transfer. The increased A allows more VOCs to come into contact with the evaporation surface, thereby enhancing the overall transfer process. The larger interface area directly contributes to the higher removal efficiency E by providing more sites for VOCs to evaporate. Similarly, Chen's team developed a novel dual-function solar-driven evaporation and photocatalysis system that combines efficient water evaporation with *in situ* purification (Fig. 25b).[201] This system, constructed from vertically aligned, wood-derived porous carbon uniformly loaded with polymetallic oxide nanoparticles, harnesses the synergy between photothermal conversion and photo-Fenton reactions. The hierarchical wood structures and embedded nanoparticles provide an optimal platform for photothermal conversion, catalytic activity, and effective transmission channels. This cutting-edge system delivers rapid water evaporation

Fig. 25 Application for the removal of volatile organic compounds (VOCs) in wastewater. (a) Schematic diagram and performance of a super water-extracting gel (SWEG) for VOC removal driven by ISVG. Reprinted with permission.[200] Copyright 2022, Wiley-VCH; (b) bionic design and degradation performance of highly concentrated mixed volatile organic wastewater treatment driven by ISVG. Reprinted with permission.[201] Copyright 2022, Elsevier; (c) diagram and performance of a solar-driven interfacial system to treat both volatile and non-volatile compounds *via in situ* photogenerated H_2O_2 and •OH. Reprinted with permission.[202] Copyright 2022, American Chemical Society.

This journal is © The Royal Society of Chemistry 2025

Energy Environ. Sci., 2025, **18**, 6366–6437 | **6405**

rates of up to 3.23 kg m^{-2} h^{-1} and effectively purifies mixed volatile wastewater, including rhodamine B, phenol, and tetracycline, at ultra-high total concentrations of up to 11 700 mg L^{-1} under one-sun irradiation. In a more recent work, Wang's group presented a solar vapor generator that demonstrates high efficiency in VOC degradation through the *in situ* generation of H$_2$O$_2$ and $\cdot$OH (Fig. 25c).[202] This system achieves a photothermal conversion efficiency of approximately 87.8% under one-sun solar irradiation, effectively activating localized H$_2$O$_2$ and $\cdot$OH production. This process not only rapidly generates steam but also creates a buffer zone enriched with H$_2$O$_2$ and $\cdot$OH, facilitating the swift removal of organic pollutants. The self-cleaning capability of the generator is effective against various volatile compounds, including phenol, aniline, 2,4-dichlorophenol, and *N,N*-dimethylformamide, across a wide concentration range.

In fact, it is worth noting that the application of interfacial evaporation technology for wastewater treatment is largely still in the experimental stage, and there is a significant gap between laboratory research and practical engineering applications. Specifically, it is essential to develop long-term stable, anti-fouling, and corrosion-resistant materials (such as hydrophobic/hydrophilic coatings or nanostructured materials) to effectively reduce surface fouling, extend equipment lifespan, and enhance evaporation efficiency. Additionally, optimizing the design of micro- and nanostructured surfaces can facilitate the rolling and coalescence of water droplets, thereby improving condensation efficiency and increasing overall water collection. Furthermore, efficient airflow guidance and condensation systems need to be designed to accelerate the transport of vapor from the evaporator to the condenser, minimizing vapor residence time. Moreover, optimizing the surface area and structural design of condensers is critical for improving condensation efficiency, ensuring maximum water recovery and reducing heat loss.

The future of interfacial evaporation for VOC removal lies in further material innovation and system optimization. Enhancing the intrinsic properties of hydrogels and catalytic materials can lead to even higher efficiencies. Integrating multifunctional materials that combine photothermal, photocatalytic, and adsorption properties can create synergistic effects, further improving performance. Additionally, scaling these technologies for real-world applications involves overcoming challenges related to system stability, durability, and cost-effectiveness. Research should focus on developing scalable manufacturing processes and ensuring long-term operational stability under varying environmental conditions.

3.1.3 Water desorption in atmospheric water harvesting (AWH). Water desorption in atmospheric water harvesting (AWH) is closely linked to interfacial evaporation, both aiming to convert water from a liquid or adsorbed state into vapor efficiently. By using interfacial evaporation techniques, AWH systems can improve water desorption efficiency through localized heating and optimized mass and energy transport, effectively releasing water from moisture-absorbing materials. In the following section, we will explore specific examples and case studies that highlight the successful application of interfacial

evaporation in atmospheric water harvesting, demonstrating its practical benefits and advancements.

The ability to achieve high-yield water harvesting hinges on the rapid dynamics of water adsorption and desorption. However, the intricate multistep sorption mechanisms complicate the understanding of the structure–activity relationship in nanoporous carbon and its water sorption dynamics. Generally, water adsorption–desorption on nanoporous carbon involves several stages: Initially, water molecules adhere to the adsorbent particles, penetrate into open pores (ii, iii), and are then adsorbed by specific binding sites (iv). Finally, the water molecules are desorbed and leave the adsorbent (v). Modifying material properties can enhance one diffusion step while impeding another. For instance, increasing the hydrophilicity within pores aids water entry (step (iii)), but may obstruct the in-pore diffusion (steps (iv) and (v)), thereby decelerating the overall water uptake. Therefore, a systematic investigation into how structural factors influence each diffusion step is crucial for designing nanoporous carbon materials that can facilitate rapid cycling and thereby achieve higher yields. In 2022, Zhu and co-workers developed a nanoporous carbon material derived from metal–organic frameworks (MOFs), which demonstrated remarkable sorption kinetics and photothermal properties, making it highly effective for atmospheric water harvesting (AWH). The optimized structure, characterized by 40% adsorption sites and pore sizes of approximately 1.0 nm, achieved enhanced sorption kinetics by reducing diffusion resistance. Additionally, this carbon-based sorbent exhibited rapid desorption kinetics, facilitated by efficient solar-thermal heating and high thermal conductivity. This innovative rapid-cycling water harvester was capable of producing 0.18 L of water per kilogram of carbon per hour at a relative humidity of 30% under one-sun illumination (Fig. 26a).[203] These findings highlight the potential of finely tuned nanoporous carbon materials to significantly improve the efficiency and yield of AWH systems. However, the low water production rate restricted its long-standing application. Wang and co-workers introduced a simple method for synthesizing bidirectionally aligned, hierarchically structured nanocomposites (BHNC) aimed at scalable and efficient solar-assisted atmospheric water harvesting (SAWH) (Fig. 26b).[204] The BHNC benefits from the synergistic effects of its ordered hierarchical structures, which enhance vertically oriented moisture convection and radially oriented intrapore diffusion. As a result, the BHNC achieves an ultrahigh water uptake of 6.61 kg of water per kg of sorbent and exhibits exceptionally fast water sorption kinetics, surpassing current leading sorbents. Additionally, a scalable and efficient solar-driven SAWH prototype was also developed by assembling arrays of BHNCs. This prototype demonstrated rapid cycling and high-yield water production, reaching up to 2820 mL of water per kg of sorbent per day. This work paved a way for scalable, energy-efficient, and all-weather water harvesting from the air using solar energy. Recently, Si and colleagues developed a bio-based gel (cellulose/alginate/lignin gel, CAL gel) by integrating a whole biomass-derived polymer network with lithium chloride (Fig. 26c). This CAL gel exhibits rapid adsorption and desorption kinetics, achieving a water capture rate of 1.74 kg kg^{-1} h^{-1} at

6406 | *Energy Environ. Sci.*, 2025, **18**, 6366–6437

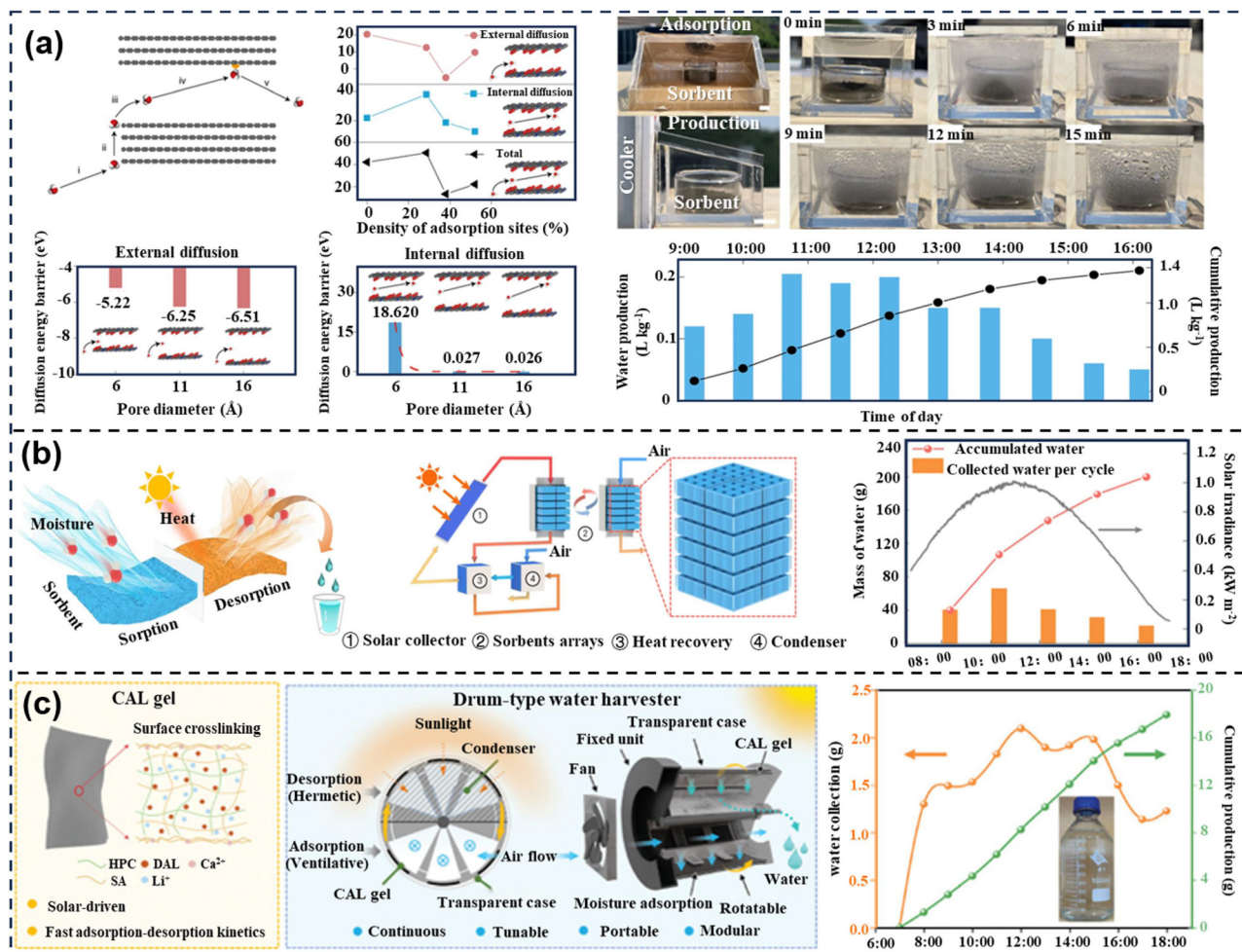This journal is © The Royal Society of Chemistry 2025

Fig. 26 Integration of ISVG and AWH for water harvesting. (a) Diffusion process of water vapor in nanoporous carbon and practical water production. Reprinted with permission.[203] Copyright 2022, Springer Nature; (b) mechanism and operating principles of the water sorption/desorption process for rapid-cycling water harvesting from air driven by solar energy. Reprinted with permission.[204] Copyright 2023, American Chemical Society; (c) schematic of the CAL gel with excellent solar-to-vapor ability and fast adsorption–desorption kinetics for continuous water production. Reprinted with permission.[205] Copyright 2024, Wiley-VCH.

30% relative humidity and a desorption rate of 1.98 kg kg^{-1} h^{-1}. To harness these properties, a solar-driven, drum-type, tunable, and portable harvester was developed. This device efficiently captures atmospheric water, operating 36 cycles (180° rotations) per day under outdoor conditions, and achieves a water yield of 8.96 kg kg^{-1} h^{-1}.

Despite encouraging progress, the overall performance of water desorption in AWH systems still requires significant improvement. Water desorption typically involves heating the sorbent to re-vaporize the captured water. To enhance this process, designing materials with nanoscale structures—such as porous carbon materials or photothermal conversion nanoparticles—can significantly boost water molecule adsorption and activation energy. This approach effectively lowers the energy barrier for water molecules transitioning from the adsorbed state to the evaporated state, thereby accelerating desorption. Additionally, optimizing interfacial thermal management strategies, such as combining localized photothermal effects with overall heat dissipation, can achieve efficient and uniform heat distribution, further enhancing water desorption efficiency. However, the desorption kinetics in AWH systems warrant further investigation. Beyond optimizing the internal structure, such as synthesizing interconnected porous frameworks to facilitate exchange, the surface properties of adsorbents are crucial for improving their kinetics. For instance, creating asymmetric surface geometries can enhance water droplet collection efficiency by facilitating the release of captured water in droplet form. Moreover, increasing the thermal conductivity of the surface can improve heat transfer between the adsorbent and the heater during desorption, reducing the heating time required. These advancements in material design and surface engineering can significantly elevate the overall performance of AWH systems. By addressing these aspects, we can pave the way for more efficient and scalable atmospheric water harvesting technologies, potentially offering robust solutions to water scarcity.

The specific details are outlined in Table 1 below, which provides a clear overview of the experimental conditions across

This journal is © The Royal Society of Chemistry 2025

Energy Environ. Sci., 2025, **18**, 6366–6437 | **6407**

Table 1 Summary of experimental parameters for vapor condensation-oriented ISVG applications

Application scope	Solar evaporator	Solar irradiance (kW m^{-2})	Ambient temperature (°C), relative humidity (%)	Water collection rate (kg m^{-2} h^{-1})	Solar-to-vapor conversion efficiency (%)	Ref.
Saline water desalination	HNG gels	~0.65	~30, ~35	1.61	95	115
	NCF foam	~0.25	~20,—	1.05	83.8	180
	Graphene membrane	~0.8	36,—	~3.87	73.4	181
	PVA and chitosan-based copper foam	1	~25, ~55	1.95	88	182
	3D-printed hydrophobic nanostructured copper	~0.6	~25,—	1.063	70%	183
	Hydrophobic nanofiber network on PVA sponge	1	~25,—	1.07	72%	184
	Multistage solar still (TMSS)	~0.6	~28,—	5.78	385%*	185
	Multi stage membrane distillation (MSMD)	~0.5	—,—	1.65	—	186
Wastewater purification	Melamine foam skeleton with a hydrogel	1	—,—	4.2	—	192
	MoS$_2$ sponge	1	26, 66	1.41	83.45	193
	Graphene/alginate hydrogel	1	—,—	1.45	—	194
	Super water-extracting hydrogel	1	—,—	1.57	85	200
	Polymetallic oxide-loaded wood carbon	1	26, 60	3.23	—	201
	PDA and Ag/AgCl co-modified melamine foam	~0.8	—,—	~2.0	87.8	202
Water desorption in AWH	MOF-derived nanoporous carbon	1	—, 50	0.18	—	203
	Hierarchically structured nanocomposite	~0.8	~28, 30	0.28	—	204
	CAL gel	1	20–29, 24.0–28.4	~0.6	—	205

Note: "—" indicates that no relevant data is provided in the manuscript. All data presented in the table were obtained from outdoor testing as reported in the original source. The efficiency of 385% TMSS refers to the solar-to-water conversion efficiency, rather than the solar-to-vapor energy efficiency.

the selected studies, enabling a more in-depth comparison and understanding of the influence of these factors on system performance. This table is included to enhance the clarity of the discussion and provide the necessary context for evaluating the variability and relevance of the experimental parameters in relation to the performance outcomes.

3.1.4 Solar ocean agricultural cultivation. The innovative concept of a solar sea farm, utilizing cutting-edge technologies across the vast ocean expanse, is a promising solution to address the pressing challenges of water scarcity and land degradation. Integrating an ISVG system within a greenhouse-like structure could enable solar ocean agricultural cultivation, utilizing only seawater and sunlight for plant cultivation. For practical agricultural use, it is crucial to enhance the production of clean water and carefully design the system to maximize solar-to-water efficiency. In 2021, Song and co-workers created a desalination–cultivation platform that effectively combines solar-powered desalination with plant cultivation.[206] However, this platform requires separate units for seawater intake, solar evaporation, freshwater harvesting, and plant irrigation and growth, leading to substantial space usage. Additionally, this system cannot be directly implemented on sea surfaces. To address these challenges, Tan's group developed an autonomous solar sea farming system (Fig. 27a) featuring a floating photothermal evaporator integrated within the plant growth unit.[207] These evaporators efficiently convert seawater into freshwater, providing sufficient water for plant growth. By incorporating the photothermal evaporators into the plant growth chamber, the system saves space and simplifies its structure. In a similar approach, Li and his team created a 3D gradient graphene spiral (GGS) sponge designed for high-rate solar evaporation and zero liquid discharge (ZLD) desalination of high-salinity brine (Fig. 27b).[208] In outdoor trials, the GGS sponge demonstrated a remarkable freshwater production rate of 3.1 kg m^{-2} h^{-1}. The purified water

is suitable for crop irrigation through a solar-powered continuous desalination-irrigation system, improving the practical application of solar desalination devices and promoting self-sustaining agricultural irrigation solutions. In fact, high sunlight intensity causes elevated temperatures within the system, necessitating intermittent manual maintenance (*e.g.*, opening the hood) to maintain suitable plant growth temperatures. This intervention interrupts the continuous collection of clean water. Xu's group introduced a solar-powered vertical double-layer sea farming system.[209] This innovative system includes a lower ISVG chamber and an upper plant growth chamber. The photothermal evaporators in the lower chamber generate freshwater *via* interfacial solar evaporation, which then condenses on the inner walls and is transferred to the upper plant growth chamber *via* water transfer belts. This design effectively prevents overheating and maintains optimal conditions for plant growth. Moreover, the system can float directly on the sea surface without requiring external energy or freshwater inputs, making it simple, efficient, and ideal for unsupervised marine agriculture. In fact, the solar efficiency of the farming area is low as the energy needed for photosynthesis lies in the visible range, which accounts for only 51% of solar energy. To address this issue, Gu and co-workers developed an innovative off-grid maritime agriculture system, termed "Farming on the Ocean *via* Desalination (FOOD)", which integrates solar desalination with plant cultivation in a floating wooden dome (Fig. 27c).[210] This system utilizes visible light for photosynthesis while converting other spectral regions into water for irrigation. Meanwhile, the dome's light transmittance can be adjusted to optimize conditions for various plant growth stages. During outdoor tests, the system demonstrated effective water production rates suitable for germination and growth of multiple crops. This technology promises to address global water and food security challenges, providing a sustainable agricultural solution that can withstand extreme weather conditions.

Fig. 27 ISVG-driven desalination for sustainable agricultural cultivation. (a) Image of an autonomous irrigation solar ocean farm. Reprinted with permission. Copyright 2022, Wiley-VCH; (b) schematic of potential applications of the continuous irrigation system. Reprinted with permission. Copyright 2024, Wiley-VCH; (c) the proof-of concept about farming on the ocean (FOOD). Reprinted with permission.[210] Copyright 2023, American Chemical Society. TEAM represents the wood dome fabricated by a transparent evaporation material while STEAM and DREAM represent the wood dome fabricated by a semi-transparent evaporation material and dark evaporation material, respectively.

Interfacial evaporation technology for solar ocean agricultural cultivation marks a significant leap in sustainable agriculture. Recent advancements have shown substantial promise in efficiently converting seawater into freshwater while simultaneously fostering plant growth. By utilizing advanced materials, these systems significantly boost water production rates and ensure a reliable supply of clean irrigation water. Current research is dedicated to refining material properties and optimizing system designs to enhance efficiency and scalability. Looking ahead, the integration of multifunctional materials and intelligent systems is expected to further improve the adaptability and resilience of these platforms. This progress paves the way for widespread implementation, offering a robust solution to global food and water security challenges in the face of climate change and extreme weather events.

3.1.5 Solar sterilization. Sterilizing medical devices is a critical step in healthcare to ensure patient safety. Traditional steam sterilization, powered by electricity, is highly reliable and commonly used, yet it demands significant energy. In contrast, the innovative ISVG technology presents a more sustainable and cost-efficient alternative, harnessing solar energy for steam production.[211] This advancement not only reduces energy consumption but also offers an environmentally friendly solution, making it a promising option for the future of medical sterilization practices. For instance, utilizing concentrated solar light at an intensity of 2.56 W cm^{-2}, the generated steam achieved temperatures of approximately 132 °C. This enabled rapid steam sterilization, completing the process in just 5 minutes.[212] To avoid using the solar concentrator, a proof-of-concept sterilization system, highlighting significant kinetic advantages, was developed by Zhu's team (Fig. 28a).[213] This innovative system offers rapid response times, achieving a full sterilization cycle in as little as 8.4 minutes, and demonstrates remarkable energy efficiency, consuming only 100 J mL^{-1} to generate steam at

This journal is © The Royal Society of Chemistry 2025

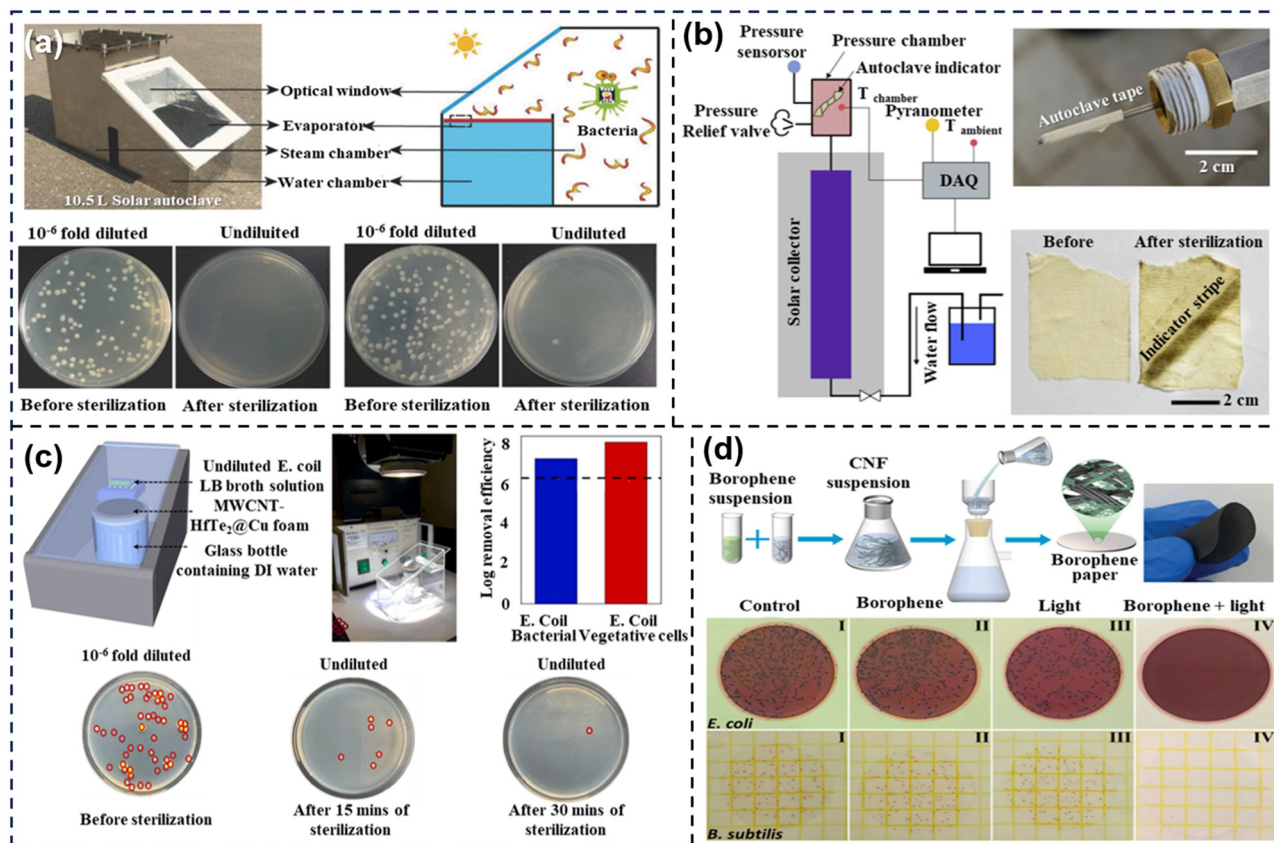*Energy Environ. Sci.*, 2025, **18**, 6366–6437 | **6409**

Fig. 28 ISVG-driven solar sterilization. (a) Bacterial sterilization performance of the interfacial-heating-based solar autoclave. Reprinted with permission.[213] Copyright 2018, Wiley-VCH; (b) schematic of the experimental setup for the sterilization demonstration with verification of effective sterilization. Reprinted with permission.[214] Copyright 2020, Elsevier; (c) schematic and image illustration of the solar-driven sterilization chamber with the removal efficiency after sterilization. Reprinted with permission.[215] Copyright 2022, Elsevier; the blue bar and red bar represent different sterilization times (15 and 30 min), respectively. While the horizontal dashed black line refers to the WHO standard for sterility of medical equipment. (d) fabrication process of the borophene/cellulose nanofiber (CNF) paper and its antibacterial performance driven by solar energy. Reprinted with permission.[216] Copyright 2023, Wiley-VCH.

121 °C. The system includes a 10.5 L solar autoclave that is cost-effective over its entire lifecycle and operates with a minimal carbon footprint. It has proven to be highly effective, achieving approximately 99.999999% pathogen inactivation, surpassing the food and drug administration's requirements. Unlike conventional methods that rely on light concentration to directly produce high-temperature steam, Wang and colleagues developed a thermal concentration approach, integrating precisely engineered optical and thermal systems to achieve elevated steam temperatures (Fig. 28b).[214] In their design, a silica aerogel—characterized by its high optical transparency and low thermal conductivity—was used to encapsulate a selective absorber, thereby significantly reducing thermal losses while permitting efficient solar transmission. To further enhance the light input, a non-imaging compound parabolic concentrator (CPC) with a geometric concentration ratio of 2.133 and an acceptance angle of 25° was incorporated. This combined system enabled the generation of saturated steam at 100 °C, achieving thermal conversion efficiencies of 56% without CPC and 47% with CPC under real-world outdoor conditions. Furthermore, when connected to a pressure chamber, the device could consistently

produce pressurized steam at 128 °C and 250 kPa, demonstrating its practical potential for applications such as sterilization. In a similar study, Tsang's team introduced a 1D–2D metallic MWCNT and HfTe2 van der Waals thermal concentration heterostructure, which elevated the steam temperature to 132 °C in under 20 minutes. The simple fabrication process and minimalist design led to a substantial reduction in sterilization costs, bringing it down to just ¢0.21 per liter. Furthermore, a proof-of-concept demonstration showed a 99.04% reduction in *E. coli* bacteria, exceeding the World Health Organization's standards (Fig. 28c).[215] Implementing this kind of sterilization system could annually reduce CO_2 emissions by 2.45 tons when replacing a conventional 10 L capacity autoclave. In a more recent advancement, the integration of borophene into cellulose nanofiber (CNF) matrices has led to the development of a highly efficient photothermal material. This composite demonstrated outstanding antibacterial performance, successfully eradicating nearly 100% of both Gram-positive and Gram-negative bacteria within just 20 minutes under irradiation equivalent to three suns (Fig. 28d).[216] This breakthrough paves the way for advanced sterilization technologies in

6410 | *Energy Environ. Sci.*, 2025, **18**, 6366–6437

This journal is © The Royal Society of Chemistry 2025

medical and environmental applications. The integration of interfacial evaporation in solar sterilization represents a significant advancement in sustainable healthcare technologies. This method not only reduces the reliance on conventional energy sources but also enhances the efficiency of sterilization processes. Moreover, the minimalistic design and cost-effective fabrication of these systems make them highly suitable for deployment in off-grid and resource-limited settings, addressing critical global health challenges. The future development and optimization of ISVG-based sterilization technologies hold great promise for improving public health outcomes, particularly in remote and underserved areas, by providing a reliable, sustainable, and cost-effective solution for medical device sterilization and water purification.

3.2 Salt extraction-oriented ISVG applications

Compared to the collection of condensed steam, salt crystallization is another significant output of the interfacial evaporation system. Focusing on salt crystallization as the target product offers a promising direction for practical engineering applications of the ISVG systems.

3.2.1 Salt ion isolation. In the ISVG process, salt ions depositing at the edge of the evaporator rather than at the surface is a complex scientific issue which involves multiple factors including fluid dynamics, thermodynamics, and the transport mechanism of dissolved matter (*i.e.* salt ions). To fully reveal and understand this phenomenon and control where salts are deposited, the following theoretical equations and factors should be considered. Then, we will dedicate some space to introducing some effective strategies currently in place to address fouling challenges.

During evaporation, the fluidity of the solution can affect the transport of salts. Edge effects, the accumulation or slowing of fluid flow at the edges of the vessel, may lead to salt deposition in these areas. This can be described by the Navier–Stokes equation, which takes into account factors such as fluid velocity, pressure, viscosity, and external forces:[217]

$$\rho\left(\frac{\partial \boldsymbol{u}}{\partial t} + \boldsymbol{u} \cdot \nabla \boldsymbol{u}\right) = -\nabla p + \mu \nabla^2 \boldsymbol{u} + \boldsymbol{f} \tag{67}$$

where density (ρ) is the density of a liquid, which affects the inertia and flow characteristics of the fluid; flow velocity (u) describes the velocity vector of the fluid in space, which is used to calculate the trajectory and velocity distribution of the fluid; pressure (p) describes the static or dynamic pressure of a fluid, which is one of the driving forces for fluid flow; dynamic viscosity (μ) is a measure of viscous resistance inside a fluid, which affects the viscosity and flow resistance of a fluid and volume force (f) represents external forces acting on a unit volume of a fluid, such as gravity or other volume forces.

The diffusion of salts can be described by Fick's second law, which states that the rate of diffusion of matter is proportional to the concentration gradient:[218]

$$\frac{\partial C}{\partial t} = -D\nabla C^2 \tag{68}$$

where C is the salt concentration and D is the diffusion coefficient. During evaporation, the nonuniform evaporation rate on the surface may lead to the formation of local concentration gradients, prompting the precipitation of salts in the marginal regions. The solubility of salts tends to change with temperature, and most salts, such as common sodium chloride, increase in solubility with increasing temperature. The temperature gradient inside the evaporator is significant, the higher temperature area may maintain more salt in the solution, while the cooler area may cause salt precipitation. This phenomenon can be described by the following equation:

$$S(T) = S_0 + \left(\frac{\partial S}{\partial T}\right)\Delta T \tag{69}$$

where $S(T)$ represents the solubility at the temperature T; S_0 is the largest solubility mass in the solution at a given temperature; $\frac{\partial S}{\partial T}$ is the partial derivative of the solubility with respect to temperature and ΔT is the change in temperature. When the temperature increases (*i.e.*, the temperature gradient increases), the solubility $S(T)$ usually increases. This means that in areas with higher temperatures, more salts can be dissolved in the same amount of solvent. The uneven distribution of temperature inside the evaporator caused by the temperature gradient will cause the solution in the higher temperature area to hold more salt while the solution in the lower temperature region may reach or exceed saturation, resulting in salt precipitation. The central temperature of the evaporator during evaporation is often much higher than the temperature at the edge of the evaporator, which explains why most of the common water–salt separation evaporator salts are precipitated and deposited at the edge of the evaporator. Notably, the evaporation rate is directly affected by temperature, and the higher the temperature, the faster the evaporation rate is generally. This leads to faster evaporation of water in regions with higher temperatures and an increase in relative salt concentration, which may trigger salt precipitation in these regions. Therefore, there is a trade-off between increasing evaporation rate and preventing salt deposition—the rate of salt diffusion and water evaporation. Salt ions should accumulate on the edge of the solar evaporator while water evaporation rate becomes highest on the centre.[63,219]

In 2020, Song and co-workers proposed an energy reutilization strategy utilizing a biomimetic three-dimensional (3D) evaporator design.[220] Within this structure, a naturally formed water film with spatially varying thickness and temperature gradients effectively captures input energy *via* the Marangoni effect, promoting localized salt crystallization. The precipitated salts remain attached to the 3D evaporator surface and can be readily removed (Fig. 29a). Notably, the extended water film within the salt layer allows for continuous evaporation without significant impairment of energy efficiency or water production rates. This approach highlights a promising pathway toward sustainable and long-term stable solar-driven desalination systems. In this work, the key parameter changes are primarily reflected in fluid dynamics, mass transfer, and surface tension. First, the fluid density (ρ) slightly increases during water

This journal is © The Royal Society of Chemistry 2025

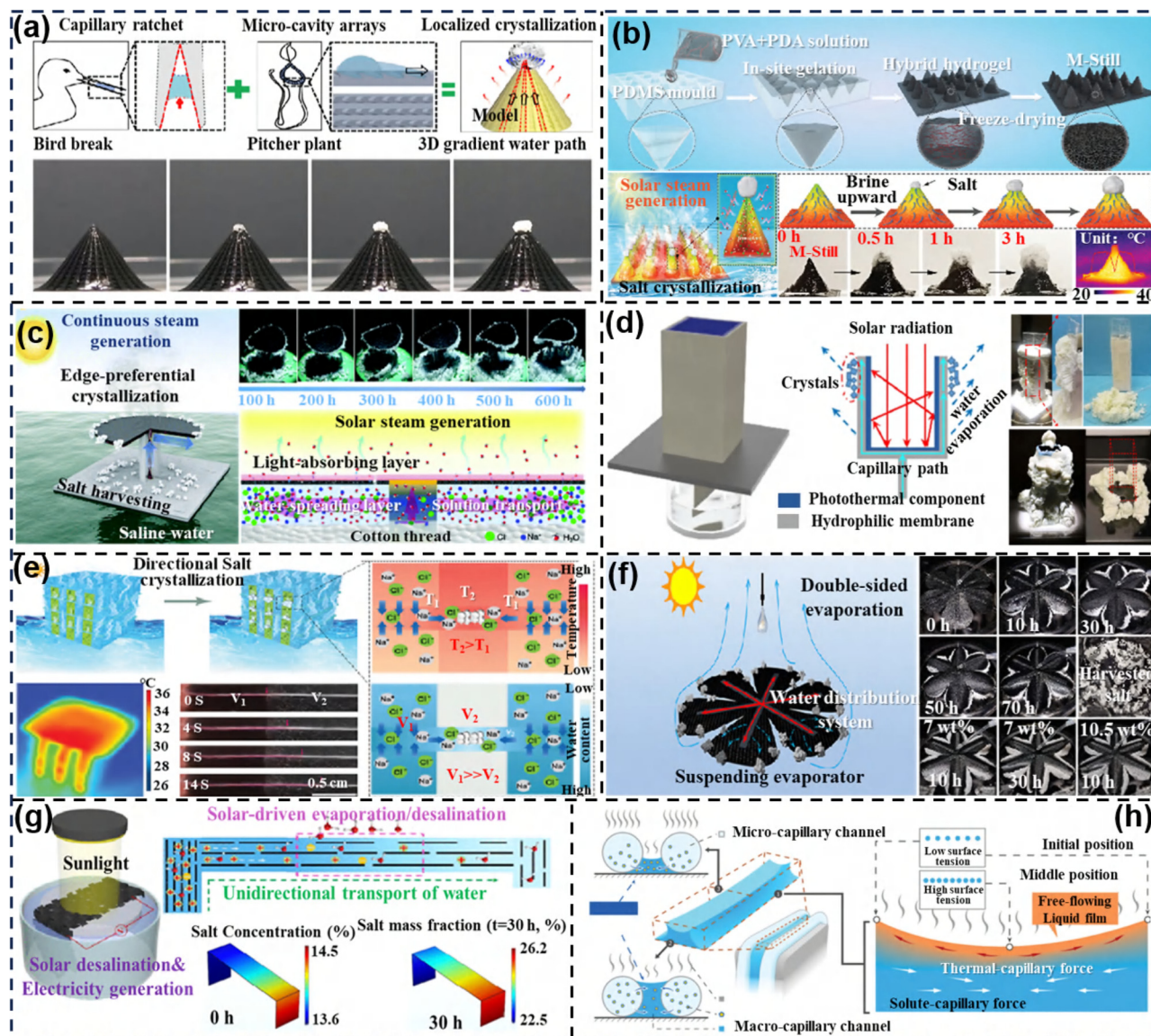*Energy Environ. Sci.*, 2025, **18**, 6366–6437 | **6411**

Fig. 29 Recent developments of salt ion isolation in the ISVG process. (a) Design of the biomimetic 3D evaporator for salt ion separation isolation from the solar evaporator. Reprinted with permission.[220] Copyright 2020, Springer Nature; (b) schematic illustration of the mill needle array solar still (M-Still) network preparation and time-sequence images of localized salt crystallization and isolation process. Reprinted with permission.[221] Copyright 2021, Wiley-VCH; (c) schematic illustration of the novel design for long-term salt separation and isolation. Reprinted with permission.[222] Copyright 2019, Royal Society of Chemistry; (d) schematic of the main and cross section view of the solar crystallizer with a photo image of self-isolated salt after 48 h operation. Reprinted with permission.[228] Copyright 2020, Springer Nature; (e) schematic of directional salt isolation within 3D evaporators. Reprinted with permission.[224] Copyright 2023, Wiley-VCH; (f) schematic diagram of suspending evaporator with salt separation and isolation performance. Reprinted with permission.[225] Copyright 2022, American Chemical Society; (g) schematic diagram of unidirectional water transport and salt ion isolation process. Reprinted with permission.[226] Copyright 2021, American Chemical Society; (h) fabric-based solar evaporator for salt ion isolation. Reprinted with permission.[227] Copyright 2024, Wiley-VCH.

evaporation due to the elevated salt concentration in the remaining liquid. The more significant impact is on fluid viscosity (μ), which rises with increasing salt concentration, leading to greater flow resistance. Moreover, the temperature gradient (ΔT) is a crucial factor. It creates a differential across the structure surface that drives the Marangoni effect. This effect causes fluid to move from cooler to warmer regions due to reduced surface tension (S) at higher temperatures. Specifically, the apex of the evaporator, where the temperature is

highest, exhibits the lowest surface tension, thereby promoting fluid flow towards this area and enhancing the evaporation rate. Additionally, the pressure gradient (∇p) decreases in regions of elevated temperature, further facilitating fluid movement towards the apex. In terms of mass transfer, the salt concentration (C) increases continuously as water evaporates, particularly at the apex. This is because the high evaporation rate due to elevated temperature leads to a significant increase in the salt concentration gradient (∇C), ultimately resulting in

6412 | *Energy Environ. Sci.*, 2025, **18**, 6366–6437

This journal is © The Royal Society of Chemistry 2025

localized salt crystallization at the apex. Furthermore, the diffusion coefficient (D) decreases with rising salt concentration, slowing the diffusion rate in high-concentration areas and further promoting localized salt crystallization. In summary, the combined effects of the temperature gradient-driven Marangoni effect, increased viscosity and changes in the concentration gradient lead to directed salt crystallization at the apex of the evaporator, achieving efficient separation of water and salt. Similarly, Lee and colleagues developed a straightforward solar evaporator featuring an array of aligned mill needles designed for efficient solar water evaporation and precise site-specific salt formation (Fig. 29b).[221] This innovative design facilitates the spontaneous formation of salt at the tips of the mill needles, enabling effective salt harvesting. In addition to top-localized salt crystallization, the precipitation of salt ions at the edges of the evaporation surface is an excellent strategy for isolating salt ions, as it prevents obstruction of incident solar irradiation on the evaporative surface. Zhang and colleagues engineered a solar-driven evaporator capable of sustaining continuous vapor generation while concurrently collecting salt from saline water by optimizing the internal transport and distribution of the salt solution within the photothermal structure (Fig. 29c).[222] A central uptake thread was introduced in the evaporation disc, establishing a radial salt concentration gradient. This configuration promoted salt crystallization exclusively at the disc periphery, thereby preserving the primary evaporation surface. Due to the relatively weak adhesion between the crystallized salts and the substrate, the accumulated salts naturally detached under gravitational force. This innovative design, featuring edge-localized crystallization and a passive self-cleaning mechanism, enabled uninterrupted vapor generation and efficient salt collection for over 600 hours of continuous operation. In this evaporator setup, with a horizontal evaporation disk and a vertical solution uptake thread, water is transported upward through the cotton thread to the disc's center, where it diffuses within the disk. This configuration creates a radial distribution of the fluid velocity field u, driving water from the center to the edge. As water evaporates from the surface of the evaporation disk, the water content decreases, leading to a continuous increase in salt concentration C. Due to the evaporation rate of water $\left(\frac{\partial u}{\partial t}\right)$ and the diffusion effect of water flow (∇u), the salt concentration gradually increases near the center of the evaporation disk and diffuses towards the edge. Meanwhile, due to the efficient light absorption properties of the carbon nanotube layer, the temperature in the central region of the evaporation disk is higher, leading to a temperature rise in the local solution (ΔT). This reduces the solubility in the central region, making it easier for the salt to precipitate. In summary, as the design of the evaporation disk causes water to diffuse from the center to the edge, the evaporation of water in the central region leads to a gradual increase in salt concentration, forming a salt concentration gradient. Simultaneously, the temperature gradient results in a solubility gradient, making salt crystallization more likely in the edge region. Experimental and CFD simulation results show that the salt concentration increases sharply from the center to the edge,

making the edge the primary area for salt precipitation. Assisted by gravity, the precipitated salt naturally falls off at the edge, achieving continuous salt collection and self-cleaning functionality. This design cleverly controls the transport paths of water and salt and utilizes the changes in temperature and solubility to achieve preferential salt crystallization at the edges of the evaporation disk. Apart from salt isolation from the evaporator surface and bulk water, Wang's group introduced an advanced approach to manage highly concentrated waste brine by utilizing a sophisticated solar crystallizer combined with a salt crystallization inhibitor (Fig. 29d).[223] This method employs nitrilotriacetic acid (NTA) to influence salt crystallization patterns on the solar crystallizer's surface, effectively preventing dense scaling crust formation during the treatment of actual seawater brine. The system demonstrated effective performance by treating highly concentrated seawater reverse osmosis brine (21.6 wt%) for 288 hours, maintaining a high and stable water evaporation rate of 2.42 kg m^{-2} h^{-1} with just 8.4 wt% of the salt as the inhibitor. Furthermore, outdoor field tests of the solar crystallizer array revealed an impressive daily water evaporation rate of 48.0 kg m^{-2}, highlighting its significant potential for practical applications. However, an additional salt crystallization inhibitor would increase the cost of practical application. A strategy that achieves zero liquid discharge without the need for the salt crystallization inhibitor was reported by Caruso and co-workers (Fig. 29e).[224] A metal-phenolic network (MPN)-engineered 3D evaporator was developed, combining photothermal superhydrophilic/superhydrophobic sponges with side-twisting hydrophilic threads. Salt crystallization predominantly takes place on the thread segments that come into contact with the superhydrophobic surfaces. The temperature variation across different components accelerates water evaporation, causing the remaining brine to become more concentrated and leading to salt precipitation. Additionally, the thread facilitates water exchange and pumping from the super hydrophilic components, controlling the flow of brine. This results in the brine on the thread reaching saturation first, forming salt crystals, and enabling directional salt crystallization. This design promotes efficient desalination with directional salt crystallization, achieving zero liquid discharge. Interestingly, to break the limitation of capillary force, Wen's group introduced a novel double-sided floating evaporator, featuring a top water supply and a surface water distribution system designed to improve solar evaporation efficiency and facilitate salt collection across large areas (Fig. 29f).[225] This evaporator design allows both sides to simultaneously evaporate water while automatically collecting salt at the edges. Remarkably, this evaporator can sustain continuous solar evaporation and concurrent salt harvesting for up to 70 hours. Meanwhile, unidirectional fluid transportation for salt ion isolation has also been investigated. In 2020, Tan's group reported a novel fluidic photothermal structure capable of unidirectional brine fluid transportation, which effectively prevents salt accumulation during long-term desalination. This system utilizes a photothermal composite material that integrates micro- and macro-capillary networks to facilitate continuous water supply and efficient solar-thermal conversion. The temperature gradient

This journal is © The Royal Society of Chemistry 2025

Energy Environ. Sci., 2025, **18**, 6366–6437 | **6413**

across the material surface drives the water molecules from cooler regions to warmer regions, promoting consistent evaporation and preventing salt build-up on the evaporation surface. Additionally, the structure induces an electric potential through the formation of an electric double layer, further enhancing salt ion migration and enabling simultaneous clean water and power production. Similarly, a photothermal evaporator using a nano-fluidic asymmetric textile pump was developed by Fu and co-workers for simultaneous salt-resistant solar desalination and power generation (Fig. 29g).[226] The system employs MXene nanosheets deposited asymmetrically on a hydrophilic cotton textile, which facilitates unidirectional saline water transport through capillary action and temperature gradients. This design prevents salt accumulation on the evaporation surface by continuously discharging unevaporated saline. In addition, the tangential shear force generated by the gradient of surface tension along the interface results in slip velocity, causing the saline liquid to move from regions of lower to higher surface tension, which is a phenomenon known as the Marangoni effect. Asinari and co-workers have, for the first time, conducted an in-depth investigation into the transport mechanism of salt ions through the Marangoni effect using numerical simulations and experimental methods. The underlying mechanism was attributed to a surface tension gradient generated by spatial variations in salt concentration. Experimental observations tracking the horizontal distribution of concentrated brine injected into the evaporator confirmed that salt transport equilibrium within the passive system could be achieved within 4 hours. Furthermore, multi-physics simulations illustrated that the Marangoni effect significantly accelerated the expulsion of the NaCl solution, effectively overcoming the salt accumulation issues typically encountered by hydrophilic evaporators following daytime operation. In a recent study, Fan and co-workers developed a fabric-based solar vapor generation device utilizing the Marangoni effect to enhance desalination performance (Fig. 29h).[227] This innovative SSG system employs a dual-capillary structure within the photothermal composite fabric (PCF), consisting of micro-capillaries within the yarns and macro-capillaries between the yarns. The Marangoni effect, driven by temperature gradients across the fabric, facilitates the efficient transport of saline water from the cooler regions to the warmer photothermal interface. This temperature-induced surface tension gradient prevents salt accumulation by directing high-salinity water away from the evaporation surface, thus maintaining high evaporation rates and energy conversion efficiency.

To address the challenges of salt deposition in interfacial evaporation systems, several key engineering strategies are recommended: (1) Temperature gradient design: Controlling the temperature distribution on the evaporative surface is crucial for directing salt deposition. By designing a temperature gradient where high-temperature regions (evaporative zones) promote evaporation and low-temperature regions (edges) facilitate salt precipitation, salt accumulation on the high-temperature surface can be minimized. This can be achieved through localized heating or cooling techniques. (2) Fluid flow optimization: Optimizing the flow path on the evaporator

surface is essential for controlling salt deposition. By adjusting the geometry of the evaporator (*e.g.*, conical shapes or flow-guiding structures), liquid flow can be directed toward edge regions, reducing flow velocity in high-temperature areas and encouraging salt deposition at the periphery rather than on the evaporative surface. (3) Real-time monitoring and dynamic control: Implementing an automated recirculation control system that monitors temperature, salt concentration, and flow velocity in real time is recommended. This system ensures rapid evaporation in the central region while directing high-concentration salt solutions to the edges for controlled precipitation and (4) heat and flow management: Utilizing a combination of fluid dynamics (based on the Navier–Stokes equation) and temperature control allows for optimized salt migration. Salt ion diffusion, driven by concentration gradients, can be regulated by real-time adjustments to evaporation rate and flow conditions, preventing salt deposition in critical areas. These strategies not only improve evaporation efficiency but also prevent equipment degradation due to salt accumulation, extending system lifespan and ensuring optimal performance.

3.2.2 High-value resource extraction.
High-value metal resources, *i.e.*, lithium (Li) and uranium (U), are critical resources with significant importance in the fields of renewable energy and nuclear power. As the global demand for sustainable and low-carbon energy solutions continues to grow, efficient and environmentally friendly extraction methods for lithium and uranium are becoming increasingly important. Interface evaporation technology has emerged as a promising approach for the extraction of lithium and uranium due to its efficiency and cost-effectiveness. However, the coupling of ISVG systems and salt separation engineering with extraction of resourceful salt from sea salt has rarely been reported in previous reviews. This section will outline the recent developments of uranium and lithium extraction, which can be used as a further continuation of the research on water–salt separation in ISVG systems. Xu and co-workers developed innovative photothermal ion pumps (PIPs) for efficient, enhanced, and sustainable lithium extraction from seawater using solar energy (Fig. 30a).[229] These photothermal ion pumps (PIPs) are engineered by coupling a hydrophilic nanofibrous core capable of selectively trapping Li$^+$ ions with an outer hydrophobic photothermal shell. This optimized spatial configuration effectively coordinates gravity-driven water transport and solar-powered evaporation, thereby enhancing ion separation efficiency and overall system performance. Unlike traditional methods, PIPs significantly improve ion replenishment, diffusion, and concentration, resulting in a higher Li$^+$ trapping rate and exceptional Li$^+$ separation factors (Li$^+$/Na$^+$ of approximately 53 747 and Li$^+$/Mg^{2+} of approximately 13 151) with minimal electric energy consumption (around 0.00358 J mg$_{Li}^{-1}$ for artificial brine and approximately 3.18 J mg$_{Li}^{-1}$ for seawater). Furthermore, deploying 18 PIPs in an array can achieve a Li$^+$ production rate of up to 308.6 mg m^{-2} day^{-1}. Zhang's group developed a specialized solar evaporator (S-evaporator) to achieve efficient fresh water collection and selective Li$^+$ adsorption from brine using only sunlight (Fig. 30b).[230] The S-evaporator features a tilted n-shaped fabric modified with H$_2$–TiO$_3$ and a photothermal sheet. The super-

6414 | *Energy Environ. Sci.*, 2025, **18**, 6366–6437

This journal is © The Royal Society of Chemistry 2025

hydrophilic fabric channels brine to the photothermal sheet, offering ample sites for Li$^+$ adsorption while the photothermal sheet boosts solar evaporation and enhances Li$^+$ adsorption by significantly increasing the fabric's temperature. This configuration allows for simultaneous freshwater collection and selective Li$^+$ adsorption. Under one-sun illumination, the S-evaporator maintained a stable evaporation rate of 1.51 kg m^{-2} h^{-1} over the long term for 20 wt% brine and achieved a high Li$^+$ adsorption capacity of 20.09 mg g^{-1}. However, the aforementioned studies require further desorption to obtain a lithium-rich solution after the successful extraction of Li$^+$. Ren's group developed an effective and self-concentrating crystallization technique for selectively extracting lithium from brine and seawater (Fig. 30c).[231] This approach uses a twisted, slender 3D porous natural cellulose fiber structure to achieve sequential and separable crystallization of cations with varying concentrations and solubilities through capillary and evaporative flows. The process demonstrated a high evaporation rate of 9.8 kg m^{-2} h^{-1}, significantly concentrating lithium. As water evaporates, LiCl remains within the crystallizer, and a wash-soak method was employed to recover the Li-rich salt. In this method, the Na-rich outer layer was removed by briefly dipping the crystallizer in water. This work provided an efficient and sustainable approach for lithium extraction. Furthermore, Jin and co-workers introduced a method for directly extracting lithium from salt-lake brines by combining an ion separation membrane with a solar-driven evaporator (Fig. 30d).[232] This ion-selective system employs a multilayer architecture: a top photothermal layer to drive water evaporation, an intermediate hydrophilic porous membrane that generates capillary pressure to sustain water transport, and a thin ion separation membrane at the bottom that selectively permits Li$^+$ ions to pass while effectively excluding multivalent ions. This integrated design enables outstanding lithium extraction performance. In experiments using synthetic salt-lake brine with a total salt concentration of 348.4 g L^{-1}, the system successfully decreased the Mg^{2+}/Li$^+$ ratio by 66-fold, from an initial value of 19.8 down to 0.3. This study combines ion separation with solar-driven evaporation to directly obtain LiCl powder for the first time, offering a novel insight and approach for the direct extraction of lithium from seawater. In a most recent study, Song and colleagues introduced a solar transpiration–powered lithium extraction and storage (STLES) system that utilizes natural sunlight to extract and store lithium ions from brines with the help of a hierarchically structured solar evaporator (Fig. 30e).[233] Specifically, this device integrates interfacial evaporation with selective membrane filtration to create a pressure gradient that facilitates the efficient separation of lithium ions from brines while storing them in a vascular-inspired layer. This nature-inspired system addresses the challenges of high energy consumption and environmental costs associated with conventional lithium mining. Extensive long-term experiments demonstrated its scalability, compatibility with various brine compositions, and robust stability, highlighting its practicality for real-world applications. This study represents a milestone in the field, as it successfully demonstrates the feasibility and practicality of lithium extraction through interfacial solar vapor generation (ISVG). The innovative integration of solar-driven evaporation and ion-selective filtration not only addresses critical challenges in selectivity and sustainability but also firmly establishes ISVG as a credible and scalable approach for resource recovery. With the publication of this work, the concept of lithium extraction *via* interfacial evaporation has gained significant academic recognition, marking a transformative moment that solidifies its position as a groundbreaking engineering solution in sustainable resource mining.

Similar to lithium, uranium extraction through interface evaporation presents significant opportunities for enhancing resource recovery efficiency and environmental sustainability. Hydrogels are chosen as the base material for coupling interfacial evaporation with uranium extraction from seawater primarily due to their excellent water absorption and retention capabilities, which ensure a continuous water supply and facilitates the migration and adsorption of uranyl ions. Additionally, their three-dimensional network structure offers excellent ion transport properties, accelerating the diffusion of uranyl ions towards adsorption sites, thus enhancing extraction efficiency. Moreover, the tuneable chemical properties of hydrogels, achieved by incorporating functional ligands, can significantly improve the selective adsorption of uranyl ions, making hydrogels an ideal material for this application. For example, Yuan and colleagues developed a plant-mimetic directional-channel poly(amidoxime) (DC-PAO) hydrogel to enhance uranium extraction efficiency by actively transporting uranyl ions into the adsorbent (Fig. 30f).[234] The oriented channels were created in the PAO using an ice-crystal growth technique, with channel diameters adjustable by altering the solid content of the precursor solution. These directional channels remained stable in seawater, providing optimal pathways for the rapid transport of uranyl ions into the hydrogel network. Building upon this design, the system demonstrated a markedly enhanced uranium adsorption performance driven by transpiration-assisted flow and efficient solar desalination. Specifically, under natural seawater conditions over a period of seven days, the hydrogel achieved a uranium uptake capacity of 6.42 ± 0.56 mg g^{-1}, significantly outperforming the hydrogel lacking liquid transport channels (3.58 ± 0.39 mg g^{-1}) and the DC-PAO hydrogel operated without solar irradiation (4.69 ± 0.42 mg g^{-1}). These results highlight the critical role of photothermal-driven water transport and structural optimization in promoting selective ion capture from complex aqueous environments. Meanwhile, this hydrogel enabled an efficient solar evaporation performance of 2.86 kg m^{-2} h^{-1}. Similarly, a solar thermal collector featuring 3D ion-transport networks made from eco-friendly biomass adsorption material was reported (Fig. 30g).[235] This material includes antibacterial adsorption ligands and photothermal graphene oxide. The antibacterial properties achieved through a simple one-step reaction, combined with the rapid mass transfer from photothermal conversion, collectively enhance the original adsorption capacity of the hydrogel by 46.7%, reaching 9.18 mg g^{-1} after 14 days of exposure to natural seawater. Guo's group developed a DNA hydrogel-based solar-powered evaporation system designed for both freshwater production and uranium extraction from natural seawater (Fig. 30h).[236] The DNA

This journal is © The Royal Society of Chemistry 2025

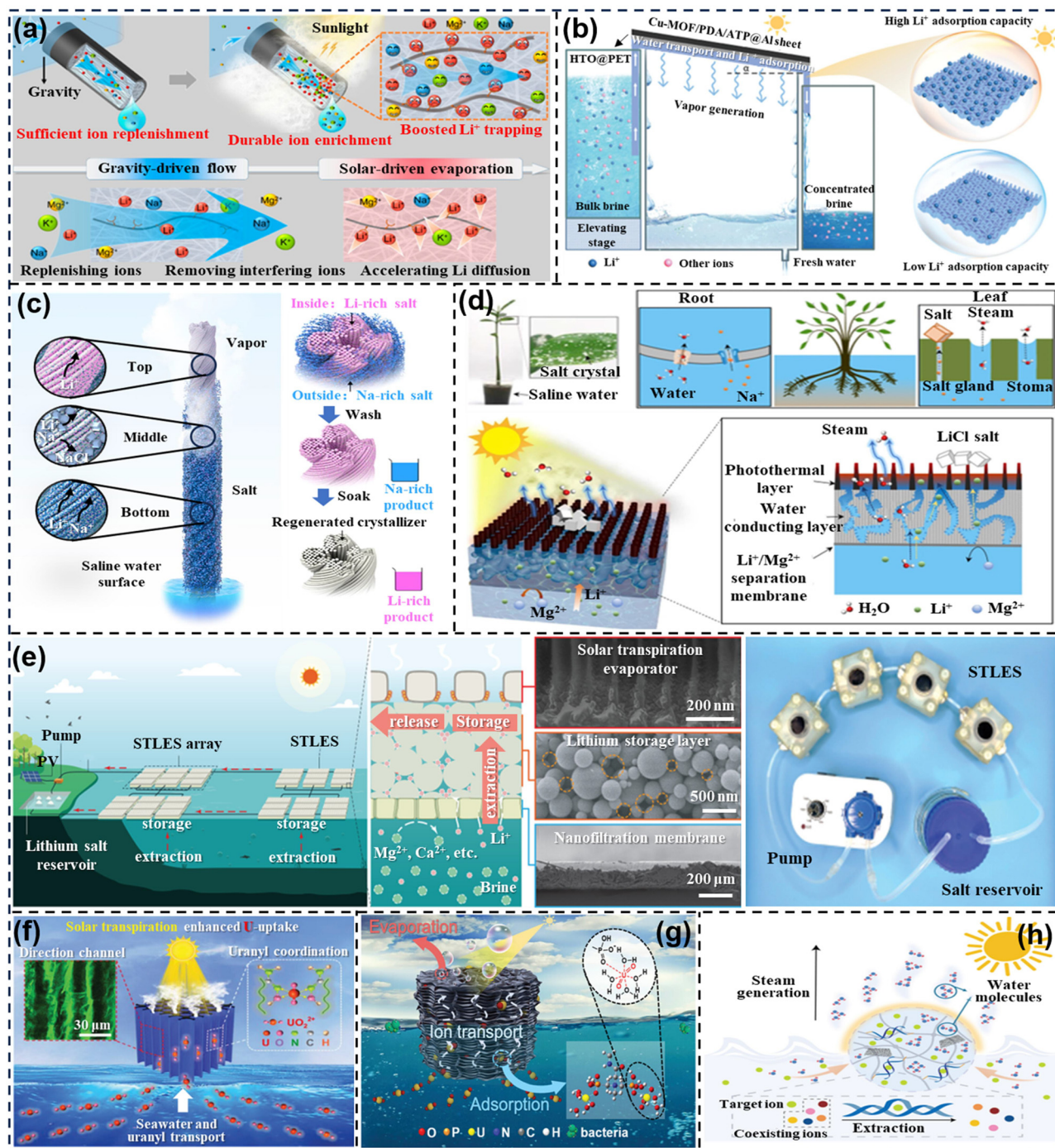*Energy Environ. Sci.*, 2025, **18**, 6366–6437 | **6415**

Fig. 30 Resource extraction during the ISVG process. (a) Schematic diagram of photothermal ion pumps (PIPs) for effective lithium extraction. Reprinted with permission.[229] Copyright 2024, American Chemical Society; (b) schematic illustration of simultaneous fresh water collection and lithium selective adsorption using the separated solar evaporator. Reprinted with permission.[230] Copyright 2024, Wiley-VCH; (c) schematic of the 3D spatial crystallization and recovery process. Reprinted with permission.[231] Copyright 2023, Springer Nature; (d) working principle of polyamide membrane-based ISVG-driven lithium extraction. Reprinted with permission.[232] Copyright 2024, Springer Nature; (e) schematic illustration, structural characterization and system setup of the STLES. Reprinted with permission.[233] Copyright 2024, American Association for the Advancement of Science; (f) schematic of transpiration-enhanced uranyl ion extraction from seawater by a directional-channel hydrogel. Reprinted with permission.[234] Copyright 2021, Wiley-VCH; (g) schematic diagram of ISVG-enhanced uranium adsorption from seawater. Reprinted with permission.[235] Copyright 2023, Wiley-VCH; (h) the solar-powered GO-loaded DNA hydrogels (GDHs) for uranyl ion extraction. Reprinted with permission.[236] Copyright 2023, American Association for the Advancement of Science.

hydrogel significantly enhanced water evaporation, achieving an evaporation rate of 3.54 kg m^{-2} h^{-1} under one-sun irradiation. Additionally, the uranyl-specific DNA hydrogel demonstrated a high uranium capture capacity of 5.7 mg g^{-1} from natural seawater, attributed to the rapid ion transport driven by solar-powered interfacial evaporation and its high selectivity.

6416 | Energy Environ. Sci., 2025, 18, 6366–6437

This journal is © The Royal Society of Chemistry 2025

Despite the promising advancements in coupling interfacial evaporation technology with the extraction of valuable metals in recent years, current applications are still in the early stages, and several scientific issues require further study. Firstly, the kinetic mechanisms need more in-depth research. We need to better understand the dynamics of water evaporation and ion migration during the interfacial evaporation process. This involves studying the relationships between evaporation rate, ion migration rate, and material properties such as pore size, hydrophilicity, and photothermal conversion efficiency to optimize material design and process parameters.

Secondly, the principles of diffusion and mass transfer need further exploration. The behavior of ion diffusion and mass transfer within adsorbents is critical for extraction efficiency. In addition, while ISVG technology has shown considerable progress in seawater desalination and conventional salt extraction, its potential in the extraction of high-value resources remains underexplored. Specifically, in the extraction of high-value salts such as boron (B), potassium (K), and iodine (I), ISVG could significantly expand its applicability. Moving forward, ISVG-based systems can be optimized by tailoring evaporation and condensation processes to the unique physical and chemical properties of these compounds, enabling more efficient and selective extraction.

3.3 Coupling electric generation with ISVG technology

The integration of photovoltaic (PV) and electric generation with ISVG technology represents a promising frontier in the development of multifunctional, sustainable energy–water systems.[237,238] Fundamental principles behind this integration lie in the system's ability to simultaneously capture solar energy for both photothermal evaporation and the generation of electrochemical potential. To date, a wide range of materials have been explored for the construction of hydro-voltaic devices, including carbon-based materials,[239–241] inorganic semiconductors,[242,243] metal oxides,[244,245] biomass materials,[246–248] and others,[249–253] and have emerged for constructing electricity generation systems coupled with ISVG technology. Building upon these diverse studies, this section will introduce the latest developments in solar evaporation-induced electricity generation, including water-flow mechanisms (*i.e.*, hydro-voltaic and salinity gradient-induced electricity generation) and heat-flow generation mechanisms (*i.e.*, temperature difference).

3.3.1 Water-flow induced electricity generation in the ISVG process. Various mechanisms, including streaming potential, evaporation potential, and salinity gradient, can lead to the generation of electrical potential during the solar evaporation process (Fig. 31). In this section, we will review the development of water-electricity co-generation cases based on these three mechanisms within ISVG technology.

Natural evaporation is an inherent physical phenomenon wherein liquid water absorbs thermal energy from its environment and undergoes a phase transition to vapor. This fundamental mechanism is central to maintaining the global water cycle and drives water transport in various liquid-phase systems. During the evaporation process, water molecules escape from the liquid–vapor interface, establishing a vapor pressure gradient that propels the molecules away, thereby forming a localized low-density zone at the interface (Fig. 31a). Cohesive forces between the molecules then pull nearby liquid molecules into this low-density area, maintaining the flow of water along the channel. This interaction between mass and heat transfer generates significant energy flux, which can be effectively utilized for continuous electricity generation with the help of nanostructured materials. The thermal energy absorbed from the environment can serve as the primary energy source for electricity production. In 2017, Guo's team has made a significant breakthrough by developing an electrical generator that harnesses water evaporation on nanostructured carbon materials, consistently generating voltages of up to 1 V under ambient conditions for the first time (Fig. 32a).[254] This pioneering research has sparked significant interest and inspired subsequent studies in this field. Meanwhile, Zhang's group also introduced a novel evaporation potential-induced electricity generation system (HPGS) that combines environmental water harvesting with a patterned coating, a solar steam generator (Fig. 32b).[255] The Al_2O_3/CB nanoparticle-based coating exhibited remarkable solar thermal conversion capabilities, elevating the device temperature by more than 18 °C and increasing the open-circuit voltage (V_{oc}) from 2.54 V to 5.86 V at 50% relative humidity under standard solar conditions. At the same time, the system uses environmental water with a high ion concentration (conductivity of 505.95 μS cm^{-1}), which is purified
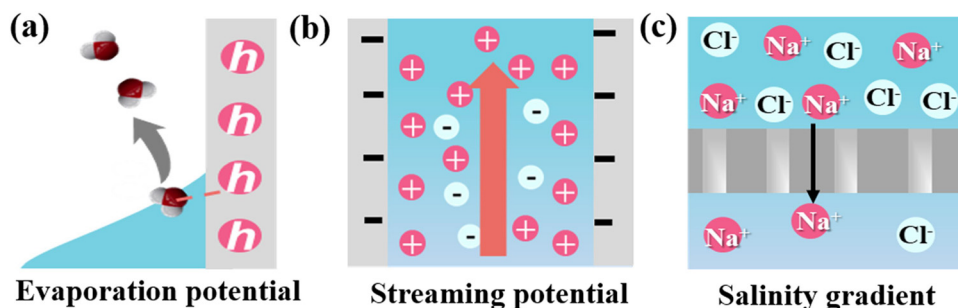

Fig. 31 Mechanisms of water–flow induced electricity generation. Schematic diagrams of (a) evaporation potential, (b) streaming potential, and (c) salinity gradient induced electricity generation.

This journal is © The Royal Society of Chemistry 2025

Energy Environ. Sci., 2025, **18**, 6366–6437 | **6417**

through the solar steam generator to produce low-conductivity pure water ($\sim$6.32 μS cm^{-1}), thereby overcoming challenges related to water source limitations for the HPGS.

While thermal energy generated from the evaporation process offers a viable method for energy harvesting, recent advances have increasingly focused on electrokinetic effects at the solid–liquid interface, particularly through the generation of streaming potential. Different from evaporation potential, the streaming potential mechanism arises from the interaction between water flow and charged narrow channels (Fig. 31b). When an ionic solution is introduced into narrow, charged micro- or nanoscale gaps, an electric double layer (EDL) forms at the solid–liquid interface due to Coulomb interactions and van der Waals forces.[258] As water flows through these charged nanochannels, counterions migrate in a directional manner, leading to the generation of electrical potential.[259] This phenomenon has been extensively explored in both natural porous materials and engineered micro/nanochannels.[260–264] Tang's group developed a lotus-inspired interfacial evaporation-driven hydro-voltaic generator (IEHVG) designed to efficiently co-generate water vapor and electricity from seawater. By integrating multiple IEHVGs, the system achieved an impressive voltage output exceeding 100 V (Fig. 32c).[256] This advanced system integrates a biomimetic hydrogel featuring engineered liquid transport channels, graphene quantum dot/MXene nanocomposites, and a graded hydrophobic interface. These components synergistically enhance both photothermal-driven evaporation and electricity generation by mimicking the natural transpiration mechanisms found in lotus stems and leaves. The coupled thermo-diffusion processes enable a power output density reaching 45.6 μW cm^{-2}, sufficient to operate electronic devices or recharge commercial supercapacitors. When 192 IEHVG modules are assembled, the system achieves a peak voltage of 105 V alongside a freshwater production rate of 2.0 L m^{-2} h^{-1} under optimal outdoor solar irradiation. Recently, Zhou's team developed a living leaf transpiration-based energy generator (LTG) inspired by the lotus leaf, which allows for the direct capture of latent energy through the natural transpiration process (Fig. 32d).[257] This generator showcased continuous electricity production throughout the day, with an open-circuit voltage of 0.25 V and a short-circuit current of 50 nA. The generated power was successfully enhanced through series or parallel configurations. The study offered a significant step forward in hydro-voltaic technology by demonstrating the direct harvesting of energy from plant transpiration. The LTG system's ability to generate continuous power from a natural process, which is not dependent on external water supplies, presents a sustainable, green energy solution with substantial implications for applications in off-grid settings.

In addition, osmotic pressure-driven water flow can also generate electricity. By employing an ion-selective membrane, the salinity gradient across the membrane induces the selective transport of ions, thereby converting the energy from the salinity gradient into electrical energy (Fig. 31c). In 2019, Hu and co-workers have developed an ionized wood membrane for this purpose. This membrane preserves the naturally aligned

nanochannels found in cellulose nanofibers extracted from wood. Meanwhile, these nanochannels can be functionalized to carry either positive or negative charges by *in situ* modification of the cellulose hydroxyl groups, transforming them into quaternary ammonium or carboxyl groups, respectively. The charged nanochannels then serve as selective ion transport pathways for oppositely charged ions, enabling efficient charge separation and generating an electrochemical potential difference. The wood-based reverse electrodialysis (RED) device, consisting of 100 cells arranged in a scalable stacked configuration, produces a maximum open-circuit voltage of 9.8 V when operating with synthetic river water and seawater (Fig. 33a).[265] Zhou and co-workers integrated a thermogalvanic cell (TGC) with reverse electrodialysis (RED) in the context of solar-driven interfacial evaporation for the first time, allowing for the simultaneous harvesting of energy from both temperature and salinity gradients (Fig. 33b).[266] By exploiting the synergistic effects of ion transport, this combination of TGC and RED dramatically increases the power output, achieving improvements by several orders of magnitude. The resulting steam-electricity cogeneration system demonstrates an impressive capability, producing 1.4 kg m^{-2} h^{-1} of vapor and 1.11 W m^{-2} of electricity under standard 1-sun illumination. Similarly, Qiu and co-workers developed an integrated system designed to simultaneously produce fresh water and generate electricity under varying salinity conditions while effectively preventing salt crystallization (Fig. 33c).[267] The system incorporates a distinctive interlayer structure made from polyaniline-graphene oxide-MnO$_2$ (PANI@GO/MnO$_2$) electrodes, which helps maintain electrochemical potential recovery across a wide range of ion concentrations. The inclusion of the Donnan potential generated by the anion exchange membrane further enhances performance, achieving an open-circuit voltage of 10.2 V. Under standard solar illumination, the system is capable of achieving an evaporation rate of 1.25 kg m^{-2} h^{-1}, while simultaneously preventing salt buildup, thus ensuring sustained operation over extended periods. However, systems discussed previously have shown promising results in terms of simultaneous water and electricity generation, and they often face limitations such as moderate efficiency and the need for complex materials or scaling challenges. To address these issues, Ho's group introduced an integrated system that combines desalination, power generation, and crop cultivation (Fig. 33d).[268] This innovative setup utilizes solar energy to concurrently generate fresh water, produce electricity, and provide irrigation for agricultural crops. As water evaporates, the enhanced salinity gradient drives reverse electrodialysis to harvest electrical energy, while the resulting drainage water can be used for irrigating wheat crops. Over extended operational periods, this integrated system consistently maintains an evaporation rate of approximately 1.42 kg m^{-2} h^{-1} and achieves a peak electrical power output of about 0.25 W cm^{-2}. In a recent study, Li's group introduced a novel all-day system that operates both during the day for evaporation and generates salinity-gradient electricity at night using waste-evaporated brine. This approach leverages the ionization electronegativity of the hydrogel, which selectively facilitates the transport of cations
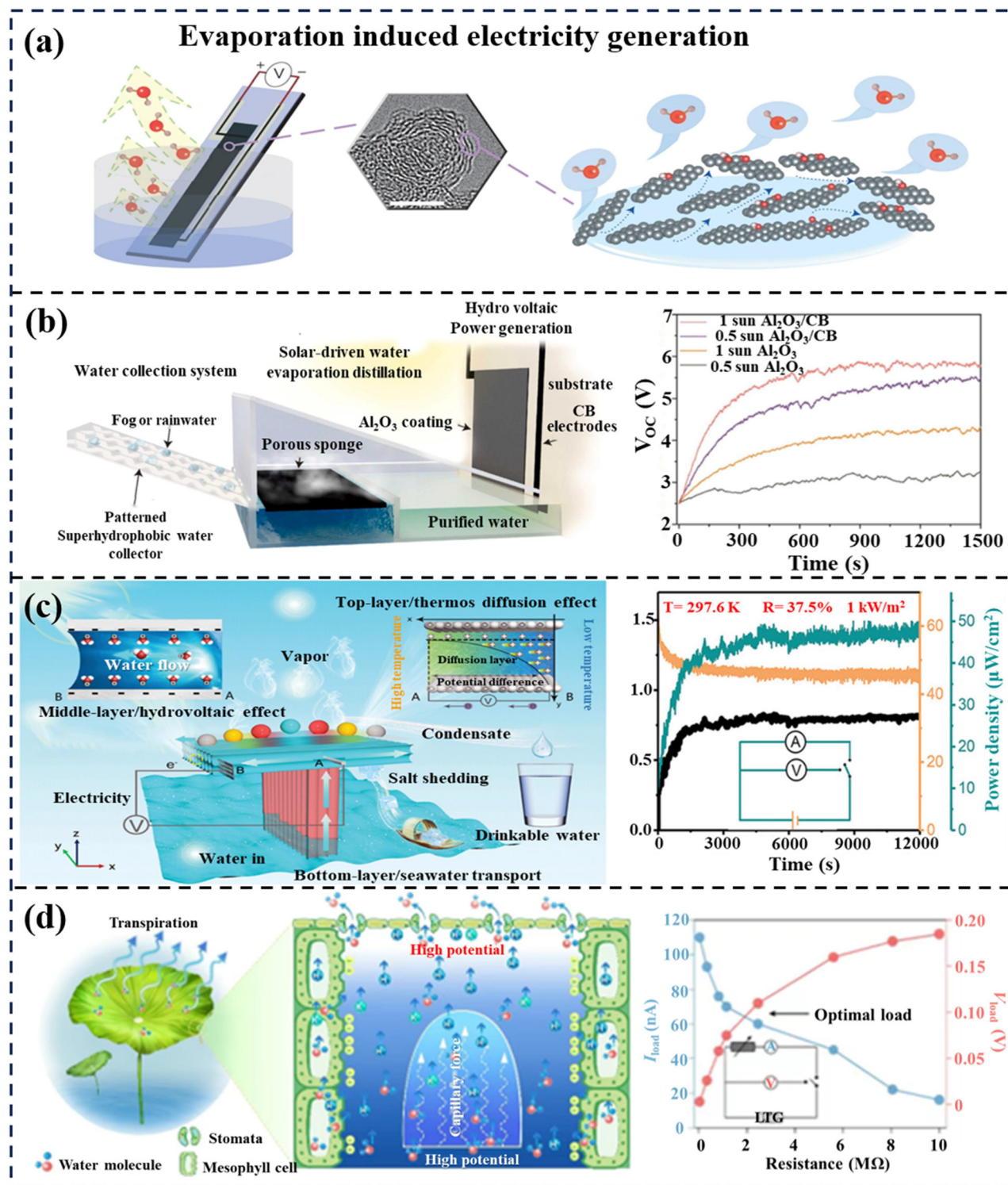
6418 | *Energy Environ. Sci.*, 2025, **18**, 6366–6437

This journal is © The Royal Society of Chemistry 2025

Fig. 32 Water-flow induced electricity generation during the ISVG process. (a) Schematic diagram of device configurations for evaporation-induced electricity generation. Reproduced with permission.[254] Copyright 2017, Springer Nature; (b) schematic diagram and performance of the solar thermal conversion boosted hydro-voltaic power generation system (HPGS). Reproduced with permission.[255] Copyright 2022, Elsevier; (c) schematic diagram and power generation performance of an interfacial evaporation-driven hydro-voltaic generator (IEHVG) system. Reproduced with permission.[256] Copyright 2024, Wiley-VCH. (d) Schematic diagram and LTG performance of the electricity generation induced by transpiration of the lotus leaf. Reproduced with permission.[257] Copyright 2024, Springer Nature.

across the salinity gradient, while anions are retained, leading to redox reactions that help balance the solutions. This mechanism promotes directional electron flow (Fig. 33e), enabling energy harvesting without the need for external power sources.[269] This innovative strategy provides a groundbreaking solution for continuous operation, combining solar desalination during the day with salinity-gradient electricity generation at night, and offers a promising advancement in addressing both water and energy challenges. Interestingly, Xu and co-workers recently developed a dual-function evaporator using gel-functionalized photothermal sponges.[270] This research introduced a new mechanism for power generation, revealing that within the intermediate water region, proton concentration fields generated by water could induce an additional ionic electric field in the free water region containing solutes, thereby enhancing the electricity output. By regulating the directional movement of water and the non-uniform distribution of water molecules within the polyelectrolyte membrane, a

high voltage output was achieved under controlled humidity conditions. Moreover, the proton concentration gradient remained stable, ensuring consistent power generation. Under standard solar irradiance, the evaporator demonstrated a high evaporation rate of 3.53 kg m^{-2} h^{-1} and a solar-to-vapor conversion efficiency of 98.6%. Additionally, it provided a sustained voltage output of 0.972 V over extended periods, even in high-concentration saline solutions, without significant salt buildup.

3.3.2 Temperature-gradient induced electricity generation in the ISVG process. The temperature gradient in the ISVG process enables the dual generation of water and electricity by leveraging both thermal and electrochemical mechanisms. As the thermal energy from solar irradiation is absorbed by the evaporator surface, a temperature differential is established between the heated surface and the bulk water, driving the phase transition of water molecules from liquid to vapor. Concurrently, this temperature gradient induces a thermoelectric potential difference
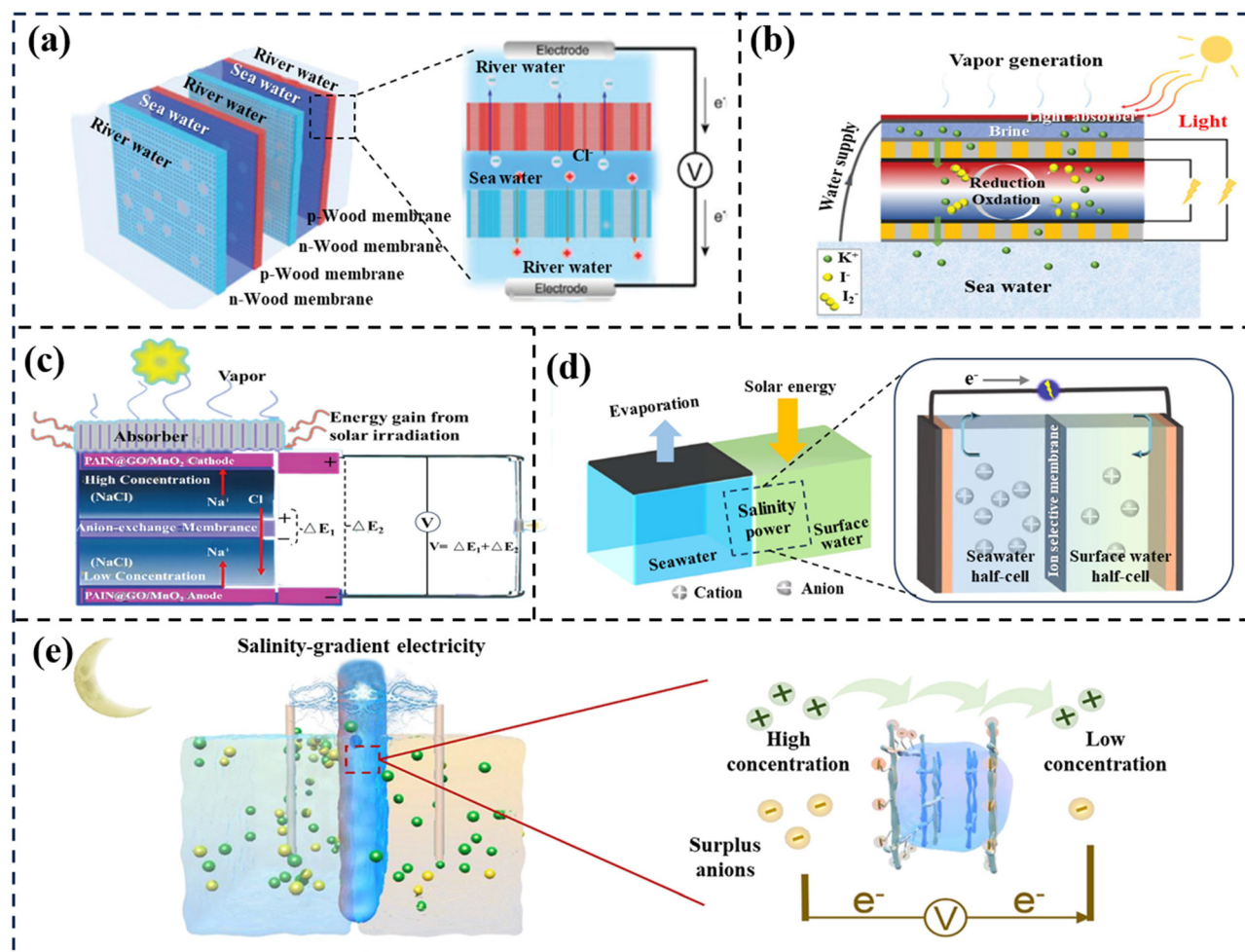

Fig. 33 Salinity-gradient induced electricity generation during the ISVG process. (a) Schematic image of a large-dimension wood-based reverse electrodialysis (RED) device for power generation from the salinity-gradient energy between river water and sea water at an estuary. Reproduced with permission.[265] Copyright 2020, Wiley-VCH; (b) schematic of the proof-of-concept device combining solar vapor generation with a thermos galvanic cell (TGC) and reverse electrodialysis (RED). Reproduced with permission.[266] Copyright 2021, Wiley-VCH; (c) schematic diagram of a PANI@GO/MnO$_2$ salinity-gradient energy harvesting system. Reproduced with permission.[267] Copyright 2024, Wiley-VCH; (d) mechanism of salinity-gradient energy extraction. Reproduced with permission.[268] Copyright 2023, Springer Nature; (e) schematic diagram of salinity-gradient electricity generation at night. Reproduced with permission.[269] Copyright 2024, Springer Nature.

within the system, creating conditions for electrochemical processes. Specifically, the gradient causes ion mobility and charge separation at the interface, which can be harnessed through thermogalvanic effects, where the heat-induced movement of charge carriers generates electrical energy. Meanwhile, the thermal flux responsible for water evaporation also facilitates ionic transport within the system, thus providing an opportunity for the simultaneous harvesting of thermal and electrical energy.

Fig. 34a illustrates a system where waste heat from a power generator is used as the heat source for water evaporation. In this setup, heat is generated by solar-irradiated modules in the power plant. The evaporator captures the waste heat from the upper part of the system, cooling the power generation module and simultaneously producing freshwater. Wang's group has developed a series of hybrid systems based on photovoltaic (PV) technology for efficient electricity-water-heat cogeneration.[186,271,272] They first presented a novel multifunctional PV panel cooling strategy leveraging an adsorption-based atmospheric water harvester as an efficient cooling component (Fig. 34b).[271] The atmospheric water harvesting (AWH)-integrated PV cooling system demonstrated a mean cooling power of 295 W m^{-2}, effectively reducing PV panel temperatures under laboratory conditions. Specifically, under a solar irradiance of 1.0 kW m^{-2}, the system achieved a temperature reduction of at least 10 °C. Field trials conducted in
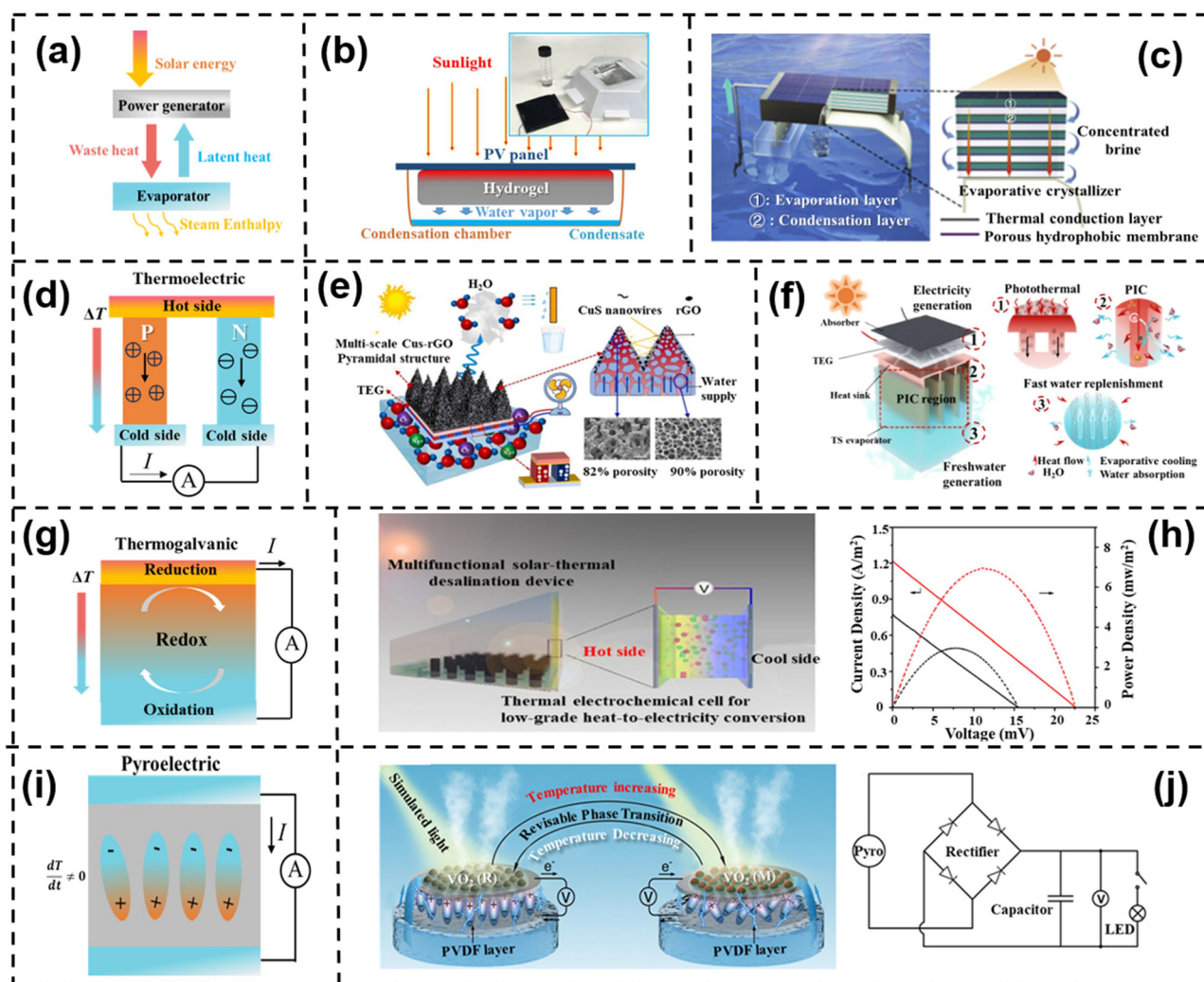

Fig. 34 Temperature-gradient induced water-electricity cogeneration during the ISVG process. (a) Mechanism diagram of waste heat recovers from the power generation module for evaporation. (b) Schematic diagram and photographic of the PV panel cooling and water harvesting test apparatus. Reprinted with permission.[271] Copyright 2020, Springer Nature; (c) schematic illustration of the PME system for simultaneous PV panel cooling and freshwater generation. Reprinted with permission.[272] Copyright 2021, Elsevier; (d) schematic illustration of thermal-electric conversion mechanisms based on the thermoelectric effect; (e) schematic diagram and performance of the multi-scale CuS-rGO pyramidal photothermal structure for integrated solar-driven water evaporation and thermoelectric power generation. Reprinted with permission.[273] Copyright 2021, Elsevier; (f) schematic diagram of the structure and heat flow for the PIC generator. Reprinted with permission.[274] Copyright 2024, Springer Nature; (g) schematic diagram of thermal-electric conversion mechanisms based on the thermos galvanic effect; (h) schematic illustration and output power density of an integrated ISVG device and thermos galvanic (TG) cell. Reproduced with permission.[275] Copyright 2023, Wiley-VCH; (i) schematic illustration of thermal-electric conversion mechanisms based on the pyroelectric effect; (j) working principle and circuit diagram of the power management system for the pyroelectric generation of the bioinspired interfacial evaporation system. Reproduced with permission.[276] Copyright 2020, Wiley-VCH.

This journal is © The Royal Society of Chemistry 2025

Energy Environ. Sci., 2025, **18**, 6366–6437 | **6421**

both winter and summer across commercial PV installations in Saudi Arabia revealed a 13–19% increase in electricity generation relative to uncooled controls. In fact, the concurrent production of freshwater and electricity using solar energy is emerging as a viable strategy for managing the water-energy nexus. To date, numerous technologies have been proposed, among which the utilization of "waste heat" from solar cells for desalination demonstrates significant promise. However, most approaches that achieve high freshwater production rates often incur a penalty in terms of elevated solar cell temperatures, which adversely affect PV efficiency. To address this challenge, their groups subsequently developed a PV membrane distillation-evaporative crystallizer (PME) system that couples an evaporator beneath a PV panel to harness waste heat for freshwater generation. Simultaneously, the latent heat released during evaporation cools the PV panel, thereby enhancing its power output (Fig. 34c).[272] This innovative design enables the simultaneous realization of efficient desalination, electricity generation, PV cooling, and zero liquid discharge within a single device.

To date, three primary thermal energy harvesting mechanisms have been extensively investigated: thermoelectric (TE), thermogalvanic (TG), and pyroelectric (PE) effects. A conventional TE generator module comprises alternating n-type and p-type thermoelectric legs interconnected by conductive tabs, as illustrated in Fig. 34d. When a temperature gradient is established across its junctions, the TE generator converts thermal energy into electricity *via* the Seebeck effect. Recent advances demonstrate that thermoelectric systems can be directly integrated with solar evaporators to recover low-grade waste heat for power generation.[277–280] Furthermore, thermoelectric modules exhibit dual functionality by serving as thermal insulators, thereby minimizing parasitic heat transfer from the evaporative interface to bulk water. In 2021, Li and co-workers reported a donor–acceptor-structured small-molecule organic solar absorber (DDPA-PDN) exhibiting broadband spectral absorption and outstanding photothermal conversion efficiency in the solid state (Fig. 34e).[273] To maximize thermal energy utilization, the researchers engineered a multifunctional hybrid device through integration of DDPA-PDN-impregnated cellulose paper with a thermoelectric module. Under one-sun irradiation (1 kW m^{-2}), this integrated system achieved a water evaporation rate of 0.89 kg m^{-2} h^{-1} while simultaneously generating a substantial output voltage of 43 mV. Recently, Lu and co-workers demonstrated a hybrid system incorporating a passive interfacial cooling (PIC) strategy (Fig. 34f),[274] which synergistically optimizes energy interplay between electricity generation and water modules. This design enables efficient cross-modular energy transfer while suppressing parasitic thermal losses by 62% compared to conventional configurations. The PIC architecture critically enhances system-level energy efficiency ($>$85%) through multiscale thermal management and near-complete utilization ($>$92%) of incident solar energy. Under standardized one-sun irradiation (1 kW m^{-2}), the system achieves a breakthrough power density of 1.5 W m^{-2} alongside a water evaporation rate of 2.81 kg m^{-2} h^{-1}, representing remarkable 328% and 158% enhancements respectively over PIC-free controls. These metrics

establish new benchmarks for co-generation systems, resolving the longstanding trade-off between photothermal and electrical outputs.

In addition, thermogalvanic cells (TG cells) are non-isothermal electrochemical systems comprising two electrodes interconnected by an electrolyte, where temperature differentials induce distinct redox reactions and establish a potential gradient between the electrodes (Fig. 34g). When integrated with an external circuit, these devices generate electrical current, effectively converting low-grade thermal energy ($<$100 °C) into electricity.[281] Notably, TG cells exhibit a high intrinsic Seebeck coefficient of $\approx$1 mV K^{-1}, an order of magnitude greater than conventional solid-state thermoelectric materials. Their unique advantages, including cost-effectiveness, mechanical flexibility, and scalable fabrication, position them as viable alternatives to solid-state TE generators for harvesting distributed low-grade heat sources. Xu's group developed a thermogalvanic cell featuring a hierarchically structured porous cellulose aerogel matrix infused with liquid electrolyte, reduced graphene oxide (rGO) photothermal absorbers, and carbon nanotube (CNT) electrodes, engineered for efficient low-grade thermal energy conversion (Fig. 34h).[275] The aerogel's ultralow thermal conductivity (0.032 W m^{-1} K^{-1}) minimizes transverse heat transfer between thermal electrodes while enabling longitudinal phonon scattering, achieving a record 89% reduction in parasitic thermal losses compared to conventional metallic heat spreaders. This architecture sustains an optimal temperature gradient ($\Delta T \approx$ 15.3 K) under natural solar irradiation (1 kW m^{-2}), yielding a peak output power density of 6.94 mW m^{-2} and surpassing existing thermos electrochemical systems by 2.7-fold. Furthermore, the cells were integrated into a closed-loop interfacial solar evaporation system, where latent heat recovery from vapor condensation contributed an additional 22% enhancement in continuous power generation. Pyroelectric materials, defined as ferroelectric substances capable of spontaneous polarization (Ps) without requiring external electric fields, convert thermal waste into electricity through their intrinsic temperature-dependent polarization dynamics (Fig. 34i). Upon heating (dT/d$t > 0$), thermal agitation disrupts dipole alignment within the material, reducing spontaneous polarization and consequently depleting bound surface charges. Under short-circuit conditions, this polarization decay drives transient current flow between electrode surfaces. Conversely, during cooling phases (dT/d$t < 0$), lattice contraction restores dipole alignment, enhancing polarization and generating reverse current flow. Unlike steady-state thermoelectric generators or thermogalvanic cells, pyroelectric systems uniquely transform oscillating thermal environments into pulsed electrical outputs. Deng and co-workers engineered a self-regulating thermal interface system through the integration of tungsten-doped VO$_2$ nanoparticles with poly(vinylidene fluoride) (PVDF) thin films (Fig. 34j).[276] This configuration induces autonomous temperature oscillations when incorporated into interfacial solar vapor generation (ISVG) systems, enabling concurrent pyroelectric power generation during solar-driven evaporation. Under simulated solar irradiation (1.1 kW m^{-2}), the system sustains periodic temperature fluctuations with a maximum $\Delta T \approx$ 7 °C

6422 | *Energy Environ. Sci.*, 2025, **18**, 6366–6437

This journal is © The Royal Society of Chemistry 2025

with a peak power density of 104 μW m^{-2}. The VO$_2$ phase-change component dynamically modulates thermal conductivity through metal–insulator transitions, maintaining 91% polarization stability over 10 000 thermal cycles while operating at 65% Carnot efficiency relative to the temperature gradient.

In summary, the innovative coupling of thermal, electrochemical, and ISVG technology enables simultaneous electricity generation and freshwater production. Breakthroughs include hybrid photovoltaic-thermal architectures achieving dual-output enhancement through passive interfacial cooling, thermogalvanic cells with exceptional low-grade heat conversion efficiency and self-regulating pyroelectric systems that harness temperature oscillations for pulsed power generation. These systems collectively address the critical energy-water nexus by maximizing solar utilization, minimizing parasitic losses and maintaining operational stability. The integration of phase-change materials, nanostructured absorbers, and hierarchical thermal management strategies establishes new paradigms for sustainable cogeneration, resolving longstanding efficiency trade-offs while enabling scalable deployment in diverse environments.

3.4 Practical engineering application of ISVG technology

Building on the fundamental principles and recent advancements in interfacial evaporation technology, it is essential to explore its practical applications, which hold significant promise for addressing critical challenges in sustainable energy and water resource management. In this section, we will introduce two ISVG engineering cases toward high-salinity wastewater purification and desalination, as well as putting forward the prospects of ISVG technology in future engineering applications.

3.4.1 Condensate water collection-oriented practical applications. Effective water collection is one of the crucial aspects of interface evaporation technologies, enabling the practical realization of efficient desalination and water purification processes. However, most of the water-salt separation devices discussed earlier remain in the experimental phase and are not yet fully suitable for practical deployment. This section presents several engineering cases that demonstrate the feasibility of using such systems for wastewater purification and seawater desalination. Among these, the Aquamate distiller (Fig. 35a) stands out as a commercially available solution. After mass production, it was introduced to the market as a light-weight, gas-filled solar still that can be easily operated by inflating it manually and securing it with a rope.

The evaporator of the distiller utilizes solar energy to extract potable water from seawater or contaminated sources. With a daily production capacity between 250 and 1800 mL, the Aquamate has been widely deployed by military and civilian sectors as a critical emergency water supply solution. During operation, solar irradiation drives the vaporization of water, while internal diffusion forces regulate the re-dissolution and precipitation of salt ions. This self-regulating mechanism effectively mitigates salt accumulation on the evaporative surface, thereby improving system solar-to-water efficiency and enabling prolonged, stable operation. Furthermore, the array-based vacuum heat pipe desalination system developed by Xi'an Qinshengfeng Technology Co. is capable of achieving efficient freshwater collection (Fig. 35b). In this solar evaporator, each module consists of an outer glass shell and dual inner stainless-steel tubes, both of which are wrapped with coconut shell fabric.

Fig. 35 Commercially available vapor collection-oriented devices based on ISVG technology. (a) Aquamate self-floating solar still (Copyright@Ecomax Tech. Co. Ltd.); (b) conventional solar vacuum tube desalination system; (c) rapid heating vacuum tube desalination system. Our group work, Product Copyright@Xi'an Qinshengfeng Tech. Co. Ltd., Photo copyright@author Yawei Yang, All rights reserved.

This journal is © The Royal Society of Chemistry 2025

Energy Environ. Sci., 2025, **18**, 6366–6437 | **6423**

Water is delivered upward through a central manifold *via* an electric pump. Similar to the Aquamate distiller, the evaporation process is assisted by diffusion forces that modulate the dynamic equilibrium between salt ion re-dissolution and crystallization. This mechanism effectively prevents salt deposition on the evaporative surface, ensuring sustained system performance and operational stability over extended periods. Currently, a single pipe unit can produce over 1 L of desalinated water per day, demonstrating excellent potential for engineering applications. This integrated design leverages the superior thermal conductivity of the heat pipes to achieve water-salt separation, with the generated steam condensing along the inner walls of the pipes, ensuring an efficient and scalable desalination process. Furthermore, to enhance the working efficiency of vacuum heat collection, an innovative mirror-enhanced vacuum heat pipe system has been developed, which is built upon the operational principles of conventional vacuum heat pipes while introducing significant advancements (Fig. 35c). Unlike traditional designs, the light concentrating device incorporates reflective surfaces that concentrate solar radiation onto the heat pipe more effectively, maximizing the absorption of solar energy. Specifically, this system integrates multiple components to enhance evaporation and condensation processes. At the top, a light concentrating device focuses sunlight onto the core region, maximizing solar energy utilization. The concentrated energy heats the multilayer evaporation surface, where saline water flows through a brine transport mechanism. The multilayer structure increases the effective evaporation surface area, thereby improving the evaporation rate. A thick tube evaporator further enhances heat transfer efficiency, ensuring that the system effectively utilizes the absorbed thermal energy. The generated vapor rises and condenses on a cooler collecting device, where it transitions back into liquid water. This condensed freshwater is collected and stored in containers positioned below the system. By combining solar energy concentration, multilayer evaporation, and optimized condensation, this system achieves a high freshwater yield, making it a promising and practical solution for solar-driven seawater desalination. Notably, due to the considerable technical challenges involved in device development and the currently low collection efficiency, no systems have yet been reported that can simultaneously collect both water and salt. As a result, the primary functions of existing devices are either focused on collecting condensate water (with salt ions returning to the bulk water) or salt extraction (where the vapor escaped without condensation).

In this collector tube system, solar radiation was adsorbed and converted into thermal energy, further enhancing the evaporation efficiency of water. By optimizing the structure and surface properties of these materials, weak interactions between water molecules and the surface can be promoted, thereby reducing the energy required for the evaporation process. Moreover, the thermal conductivity of the collector tube system is crucial for the overall performance of the system. The efficiency of heat conduction can be described by the following heat conduction equation:

$$Q = \frac{kA\Delta T}{L} \qquad (70)$$

where Q is the heat flux, k is the thermal conductivity of the material, A is the cross-sectional area of the collector tube, ΔT is the temperature difference between the evaporator surface and surrounding environment, and L is the length of the collector tube. Mirror-enhanced collector tubes (such as the mirror-enhanced vacuum heat pipe system) further improve thermal efficiency by concentrating solar radiation, thereby increasing the evaporation rate and salt separation efficiency. The mirror-enhanced system primarily impacts several key parameters in the related equations by altering the amount of solar energy absorbed and the transmission efficiency. First, the mirror-enhanced collector tube increases the incident solar radiation on the system's surface by reflecting and focusing sunlight. The reflective design significantly increases the optical concentration (C_{opt}), which represents the degree of solar energy concentration on the system's surface. The increase in optical concentration directly enhances the amount of solar energy absorbed by the system, thereby increasing the evaporation rate. Meanwhile, the mirror-enhanced system further optimizes the evaporation process by improving the thermal conductivity. The design of the heat pipe system and the mirror enhancement improve the thermal transfer efficiency within the collector tube, reducing thermal energy loss and thereby enhancing the efficiency with which water molecules are heated. By increasing the amount of solar energy absorbed (*via* mirror enhancement), the temperature difference (ΔT) within the collector tube increases, allowing thermal energy to be more effectively transferred to the water molecules, which accelerates the evaporation process.

3.4.2 Salt collection-oriented practical application. Current approaches for treating pharmaceutical high-salinity wastewater primarily include reverse osmosis, electrodialysis, and evaporation crystallization. While these technologies can achieve a certain degree of wastewater treatment and salt removal, they also exhibit significant drawbacks, including high costs, complex processes, and substantial energy consumption. To address these challenges, a high-salinity wastewater treatment platform based on interfacial evaporation was set up (Fig. 36a). This system consists of a conical evaporator (the photothermal layer of the prototype) and a salt-extraction rope (Fig. 36b). High-salinity wastewater is pumped into the conical evaporator using an electromagnetic valve (Fig. 36c and d). As the solution evaporates, the resulting supersaturated brine flows along the bottom guide line of the cone into the lower salt-extraction rope and container, where it precipitates. By collecting the crystallized salts on the extraction rope, effective water–salt separation is achieved (Fig. 36e). Currently, under adequate sunlight conditions, a single unit can treat approximately 15 L of high-salinity wastewater per day, extracting over 3 kg of crystalline salt. This process is currently in the pilot phase within the chemical industry, with the potential for further market entry upon successful testing. Meanwhile, the demonstration project of an interface evaporation system for high-salinity wastewater desalination, based on the complementary use of solar and wind energy, has been successfully applied to treat the high-salinity wastewater discharged at Ningxia, China. In this system, multiple tracks are arranged between two rollers, and rotation of the upper shaft in a counterclockwise direction drives the

6424 | *Energy Environ. Sci.*, 2025, **18**, 6366–6437

This journal is © The Royal Society of Chemistry 2025

Fig. 36 Commercially available salt collection-oriented devices based on ISVG technology. (a) Comprehensive view of the conical high-salinity desalination device; (b) Diagram showing the salt extraction rope and conical evaporator; (c) and (d) high-salinity wastewater being pumped into the conical evaporator; (e) collection of crystalline salt after evaporation; (f) comprehensive view of the solar-wind complementary system equipment; (g) day-time and (h) night-time operation state of a single unit; (i) high-salinity wastewater concentration operation state of a single unit (insert: salt crystals collected by the equipment after concentrating high-salinity wastewater); (j) Comprehensive view of the zero-liquid discharge equipment for high-salinity mining wastewater treatment. (k) and (l) Diagram of the graphene black crystal membrane for solar evaporation. Our group work, Product Copyright @ Xi'an Qinshengfeng Tech. Co. Ltd, Photo copyright @ author Yawei Yang, All rights reserved; (j)–(l) Copyright from Jiangsu Juzhilan Technology Co., Ltd, all rights reserved.

tracks upward, carrying saltwater with them. The black-coloured tracks, featuring excellent solar absorption properties, facilitate efficient evaporation under sunlight, progressively increasing the saltwater concentration. Upon reaching the stop rod, the upward movement is halted, and the concentrated brine flows back into the collection pool under gravity. During this circulation, the brine concentration continually rises, eventually achieving saturation and promoting salt crystallization and recovery. Notably, the evaporator is capable of continuous operation even during nighttime; while solar energy drives daytime evaporation, nocturnal operation can be supplemented by ambient wind. Over prolonged use, the saltwater in the lower pool transitions from an initially transparent state to a salt-enriched yellow hue, signifying successful concentration and salt harvesting. Throughout this process, the removal of water vapor leaves behind solid salt, with natural convection enhancing the evaporation rate as the solar-heated brine moves along the tracks. The evaporation rate of high-salinity wastewater using this technology ranges from 0.03 to 0.05 tons per day per square meter, with a near-perfect salt recovery rate, enabling the treatment of nearly saturated brine

(Fig. 34f–i). By incorporating specific algorithms, the system can be equipped with real-time sensors for temperature, humidity, and light intensity. Based on the acquired data, the water supply rate and operational speed of the system can be controlled dynamically, ensuring optimal performance across varying operational conditions. This desalination system, based on advanced interfacial evaporation technology, consumes only 17.5 kW h of electricity per ton of wastewater, resulting in a reduction of over $20 per ton in electricity costs compared to conventional triple-effect desalination systems. Notably, the equipment procurement costs are reduced by more than $140 000. The system is driven entirely by solar and wind energy, requiring no additional external energy input, thus providing a highly environmentally sustainable solution. Importantly, the salt crystals generated during the desalination process can be recovered and repurposed as raw materials for de-icing agents, facilitating resource recycling and promoting circular economy principles.

In salt collection systems, the separation of water and salt is fundamentally driven by multi-physical coupling phenomena at the interface, including concentration-gradient-driven diffusion,

This journal is © The Royal Society of Chemistry 2025

Energy Environ. Sci., 2025, **18**, 6366–6437 | **6425**

evaporation-induced capillary flow, and thermocapillary convection within the liquid. The efficiency of salt removal and crystallization is jointly governed by the synergistic interaction between ion transport rates and evaporation kinetics. Specifically, the local transport of salt ions can be described by the coupled advection–diffusion–capillarity equation:

$$\frac{\partial C}{\partial t} + v_{adv} \cdot \nabla C + v_{cap} \cdot \nabla C = D_{eff} \nabla^2 C \qquad (71)$$

where C is the local salt ion concentration (mol m^{-3}), v_{adv} is the bulk advection velocity field induced by evaporation, v_{cap} is the capillary-driven velocity field, and D_{eff} is the effective diffusivity of salt ions, incorporating corrections due to liquid viscosity and porous structure effects. During the evaporation process, the local concentration of salt near the evaporative interface increases, establishing a steep concentration gradient (∇C) that promotes diffusion toward regions of lower concentration. Simultaneously, capillary forces induce an upward liquid flow along the salt-extraction rope and the conical surface, continuously supplying fresh liquid and preventing surface desiccation and fouling. Notably, the conical architecture enhances the capillary gradient geometrically, thereby significantly improving the vertical transport capacity of salt ions. Meanwhile, the overall energy balance of the system follows a multi-energy coupling framework, expressed as:

$$Q_{input} = Q_{solar} + Q_{wind} \qquad (72)$$

where Q_{solar} represents the absorbed solar irradiation flux, Q_{wind} denotes the convective heat transfer flux induced by ambient wind. The hybrid solar-wind complementary system effectively enhances convective heat transfer, particularly under nocturnal or low-solar-irradiance conditions, thus maintaining a strong evaporation driving force and sustaining continuous ion migration and crystallization. As the solution concentrates during evaporation, the water activity (a_w) decreases, following Raoult's law:

$$a_\omega = \exp\left(-\frac{\nu m_s}{M_\varpi}\right) \qquad (73)$$

where ν is the van 't Hoff factor, m_s is the molality of the salt, and M_w is the molar mass of water. Upon reaching supersaturation, the system minimizes its local Gibbs free energy by precipitating solid salt, establishing a steady-state coexistence of solid and liquid phases. Through the rational design of the conical salt-extraction architecture, the system effectively regulates the spatial migration of salt ions and the selection of crystallization sites at the microscale, while maintaining continuous and stable evaporation dynamics at the macroscale. This coordination significantly enhances the operational efficiency and durability of the conical solar evaporator.

Additionally, the graphene black crystal membrane-based solar-driven photothermal evaporation technology represents a significant breakthrough in achieving zero-liquid discharge for high-salinity wastewater treatment (Fig. 36j–l). By capitalizing on the unique properties of graphene—such as exceptional mechanical strength, outstanding oxidation resistance, high-efficiency photothermal conversion, and superior thermal conductivity—this revolutionary solar-driven photothermal evaporation process

enables highly efficient treatment of high-salinity wastewater with zero discharge. In operation, an electric motor pumps the high-salinity wastewater from a reservoir beneath the evaporator into a supply pipe, from which the water flows through the upper edge into a hollow evaporator tube. A thin film of water forms on the outer surface of the evaporator, where it evaporates rapidly under natural wind and sunlight. Concurrently, some salt ions migrate to the exterior surface of the tube. To prevent salt crystallization on the evaporation surface, the system employs precise flow rate control and incorporates strategically placed small holes at the upper edge of the tube to periodically flush the surface, ensuring no salt accumulation. As evaporation progresses, the remaining wastewater moves along the evaporation interface to the lower edge of the evaporator, where it flows back through an outlet pipe and returns to the high-salinity reservoir for recirculation. This technology offers a significant reduction in energy consumption compared to traditional mechanical vapor recompression (MVR) crystallization evaporation processes, lowering the operational cost of treating high-salinity wastewater from $10.00 per ton to effectively zero. It provides an innovative and highly effective approach to realizing zero-liquid discharge for high-salinity wastewater through interfacial evaporation technology, paving the way for its commercial application in industrial wastewater management. Due to the considerable technical challenges involved in device development and the currently low collection efficiency, no systems have yet been reported that can simultaneously collect both water and salt. As a result, the primary functions of existing devices are either focused on collecting condensate water (with salt ions returning to the bulk water) or salt extraction (where the vapor escaped without condensation).

In summary, to better illustrate the key performance metrics of various solar-driven photothermal evaporation systems, including energy efficiency, material durability, and challenges in wastewater treatment, we have included a table summarizing the advantages and limitations of each approach. Table 2 below offers a comparative analysis to enhance the clarity and insight into the current state and future potential of these technologies.

3.5 Practicability and feasibility analysis of ISVG technology

To assess the feasibility and potential of ISVG technology in real-world applications, it is crucial to conduct a detailed technoeconomic analysis, which can demonstrate how ISVG systems compare to conventional desalination methods. The following analysis provides a comparison of traditional solar-thermal desalination methods with ISVG technology, highlighting key technoeconomic factors such as production costs, scalability, and solar-to-water efficiency. By evaluating these factors, we can better understand the practical viability of ISVG systems in large-scale, sustainable water purification applications. In previous studies, technoeconomic models have been proposed by Hatzell's group to assess the feasibility of coupling solar collectors with thermal desalination systems, specifically focusing on the solar multi-stage flash distillation system (Fig. 37a).[282] One key finding from these models is that the specific discounted water production cost (SDWPC) for a plant

6426 | *Energy Environ. Sci.*, 2025, **18**, 6366–6437

This journal is © The Royal Society of Chemistry 2025

Table 2 Summary of advantages and limitations of practical ISVG systems

Application types	Application system	Energy efficiency	Material durability	Advantages	Limitations
Condensate water collection-oriented applications	Conventional self-floating solar still	30–50% (solar-to-water)	~Two months	Simple water supply, evaporation, and collection structures	Sunlight scattering by transparent cover, short daily sunlight utilization
	Vacuum tube solar still	40–70% (solar-to-water)	>One year	Multi-angle sunlight absorption, high-efficiency daily sunlight utilization, robust and stable architecture	Difficult for water condensation design, requiring additional water supply control system
Salt collection-oriented practical application	Conical evaporation desalination system	60–80% (solar-to-vapor)	~One month	Outstanding wastewater treatment capability and environmental sustainability, high salt harvesting rate	Non-operational at night, Requiring effective rain and dust protection in engineering application
	Solar–wind complementary desalination system	>80% (solar-to-vapor)	>One year	Low salt accumulation on evaporation area, all weather operation, ultrahigh salt harvesting rate	Requiring additional water supply control system; rain and dust protection requirements for practical application
	Black polymer tube array membrane-based desalination system	60–70% (solar-to-vapor)	>Two months	Low salt accumulation on evaporation area;	Complex design process and high fabrication cost

Note that in "condensate water collection-oriented applications", energy efficiency refers to the solar-to-water efficiency, which represents the fraction of solar energy converted into useful thermal energy for water evaporation and condensation processes. In contrast, in "salt collection-oriented practical applications", energy efficiency pertains to the efficiency of salt extraction, specifically focusing on the effectiveness with which solar energy drives the crystallization of salts and the removal of salt ions from the solution.
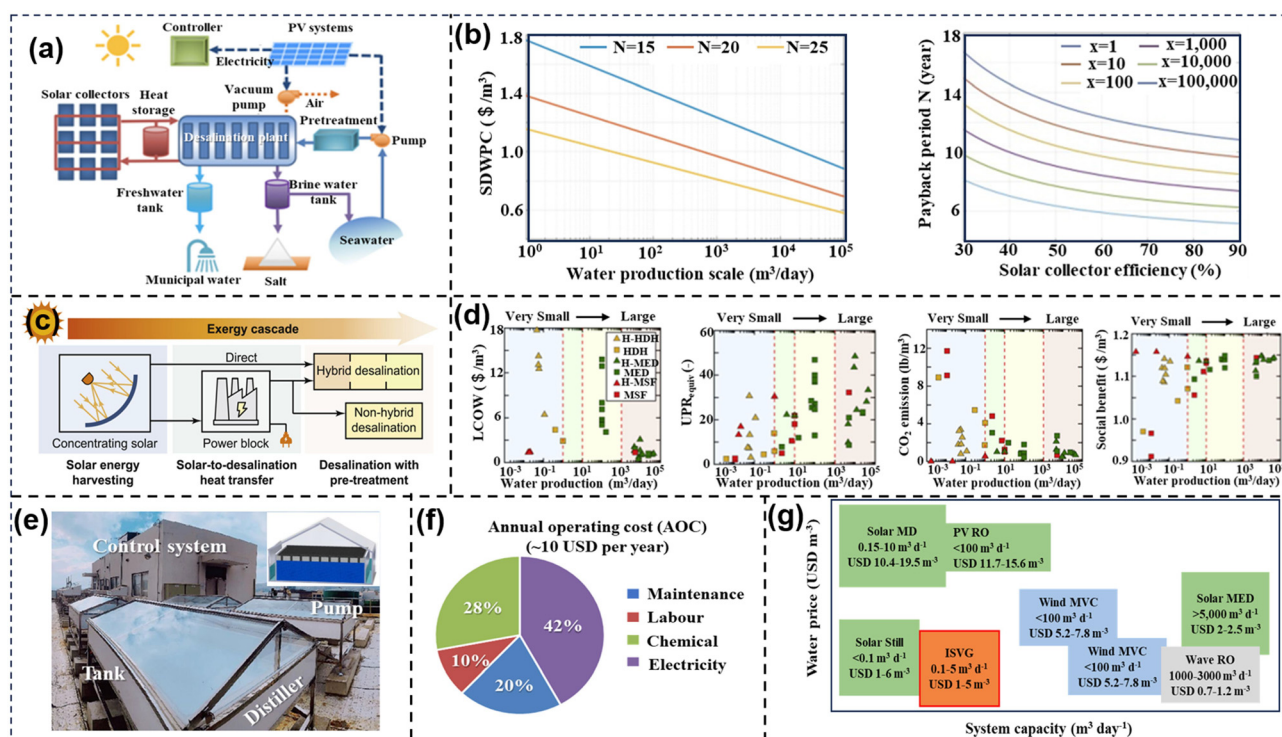

Fig. 37 Practicability and feasibility analysis of conventional solar-thermal desalination technology and ISVG technology. (a) Schematic diagram of the solar desalination system with solar energy harvesting, heat storage, and desalination units; (b) technoeconomic analysis of the relationship between specific discounted water production cost (SDWPC) and water production scale (m³ per day) for desalination systems with varying operational lifetimes (N = 15, 20, and 25 years); (a) and (b) reprinted with permission.[282] Copyright 2020, Elsevier. (c) Energy utilization cascade systems for conventional solar-thermal desalination devices; (d) technoeconomic performance and environmental impact of solar-driven thermal desalination systems. Abbreviations are as follows: MED, multi-effect distillation; HDH, humidification–dehumidification; MSF, multi-stage flash. The prefix "H" represents this solar-thermal desalination systems operating in a hybrid manner; (c) and (d) reprinted with permission.[283] Copyright 2020, Elsevier. (e) Overview of a SID desalination platform; (f) evaluation of annual operating costs; (g) trade-offs between water cost and system capacity for SID and other solar-thermal and reverse osmosis desalination technologies; (e)–(g) reprinted with permission.[284] Copyright 2025, Springer Nature.

This journal is © The Royal Society of Chemistry 2025

Energy Environ. Sci., 2025, **18**, 6366–6437 | **6427**

producing 1000 m^3 per day is \$0.97 per m^3, assuming the solar collector unit cost is \$100 per m^2 and operates at 40% efficiency. This model also highlights the relationship between the scale of the plant and the SDWPC, showing that the SDWPC decreases logarithmically with plant scale (Fig. 37b). This reduction is due to the assumption that both unit construction costs and maintenance costs decrease linearly with the logarithm of the plant scale, which results in lower costs per unit of water produced as the system size increases. Additionally, the longevity of the plant plays a crucial role in reducing the SDWPC. For plants with a typical lifetime of 15 to 25 years, the SDWPC is significantly lower for plants with longer lifetimes. For instance, for a plant producing approximately 1000 m^3 per day, the SDWPC decreases from \$1.24 per m^3 to \$0.81 per m^3 when the system's lifespan is extended from 15 years to 25 years. This is primarily because systems with longer operational lifespans can produce more water, thereby spreading out the initial capital costs. Furthermore, the efficiency of solar collectors is also a key factor influencing the economics of solar desalination. More efficient solar collectors, such as those using one-axis tracking, can significantly improve daily efficiency, thus reducing the payback period. However, this efficiency comes at a higher cost, as the installation and operation of tracking systems require more advanced technology and manufacturing processes. While higher collector efficiency can lower the payback period, the impact of increasing efficiency on payback period reduction becomes less pronounced as efficiency levels rise.

Building on this foundation, Hatzell and co-workers further quantified the technoeconomic opportunities and challenges associated with large-scale solar-thermal desalination systems (Fig. 37c).[283] Their analysis revealed that even under optimized conditions, the levelized cost of water (LCOW) for MED remains between \$1.5 and \$2.5 per m^3, depending on solar field costs and system efficiency (Fig. 37d). Although scaling up plant capacity (e.g., >10 000 m^3 per day) helps reduce the LCOW, it also significantly increases capital investment, particularly for solar collector fields, which currently cost approximately \$100–\$300 per m^2. Moreover, conventional solar thermal desalination operates at relatively low temperatures (70–90 °C), leading to substantial exergy losses and limiting the overall system energy utilization to 30–50%. To address these challenges, this study proposed advanced strategies such as exergy cascade utilization, hybridization with power generation cycles, and enhanced thermal storage integration, potentially lowering the LCOW by up to 30%. However, the inherent inefficiencies

of traditional large-scale solar thermal desalination underscore the need for alternative strategies. In this context, ISVG technology offers a promising pathway, leveraging localized photothermal conversion, efficient interfacial evaporation, and reduced thermal losses. Notably, recent engineering-scale studies have introduced the equivalent universal performance ratio (UPR$_{equiv}$) as a unified metric to benchmark the energy efficiency of solar desalination systems. For example, pilot-scale ISVG devices have demonstrated UPR$_{equiv}$ values approaching 0.85, indicating that 85% of the absorbed solar energy is effectively utilized for vapor production. Such high efficiency, combined with the modularity, scalability, and relatively low capital intensity of ISVG systems, highlights their strong potential for practical deployment, particularly in decentralized and resource-constrained settings.

Recent advances have further substantiated the practical feasibility of ISVG technology. A notable study demonstrated a large-scale solar interfacial desalination (SID) platform with a total area of 150 m^2, achieving a fresh-water production rate of 300 kg day^{-1} over four months of continuous outdoor operation (Fig. 37e).[284] Importantly, the system maintained an average daily water production rate of 2.52 kg m^{-2} d^{-1}, peaking at over 4.5 kg m^{-2} d^{-1} under favorable conditions. These results underscore the robustness and scalability of ISVG systems under real-world environmental fluctuations. From an economic perspective, cost evaluation revealed that the annualized capital investment (ACI) was approximately \$27 930 per year, while the annual operating cost (AOC) remained exceptionally low at about \$10 per year, benefiting from the nearly passive operation of the SID platform (Fig. 37f). Although the upfront capital cost is substantial—mainly due to structural, distillation unit, and control system expenses—the low operational costs offer significant advantages for long-term deployments, especially in off-grid or decentralized applications. Furthermore, technoeconomic projections indicated that with design optimizations (such as modular multistage structures and new low-cost materials), the total water production cost could be reduced to approximately \$1.78 m^{-3}, which is lower than typical tap water costs in many regions (Fig. 37g). Regarding system stability, the platform demonstrated strong long-term durability across more than 110 days of field operation with minimal fouling, salt accumulation, or efficiency degradation. This durability stems from the use of commercially available, robust evaporator materials and an optimized thermal design that minimizes energy loss and enhances system resilience. The following table (Table 3) provides a detailed comparison of

Table 3 TEA factors comparison of solar-thermal desalination and ISVG technology

Desalination technology	Key TEA metrics	Detailed insights
Conventional solar-thermal desalination	SDWPC	\$0.97 per m^3 for a 1000 m^3 per day plant
	Operation efficiency	30–50%
	LCOW	\$1.5–2.5 per m^3 for MED
	Plant lifetime impact	\$0.81 per m^3 to \$1.24 per m^3
ISVG technology	Operation efficiency	60–85%
	ACI	\$27 930 per year
	AOC	\$10 per year
	Water production cost	\$1.78 per m^3 (10 years)

6428 | Energy Environ. Sci., 2025, **18**, 6366–6437

This journal is © The Royal Society of Chemistry 2025

ISVG technology and conventional solar-thermal desalination systems, highlighting their respective strengths and challenges. By evaluating these technoeconomic indicators, we can better assess the potential of ISVG for large-scale, sustainable water treatment solutions.

Overall, in comparison to traditional solar-thermal desalination technologies, such as MSF or MED, ISVG technology presents several significant advantages. The localized heating process in ISVG results in higher energy utilization efficiency, with equivalent UPR$_{equiv}$ reaching up to 0.85 in engineering applications. This performance substantially outperforms conventional methods, where energy efficiency often falls below 50%. Furthermore, the passive operation of ISVG systems reduces maintenance and energy costs considerably, offering a more cost-effective alternative to the energy-intensive nature of traditional desalination technologies. ISVG systems also excel in scalability and modularity, allowing for flexible deployment across a wide range of scales. This makes them particularly suited for small- to medium-scale applications in remote or decentralized areas with limited infrastructure. In addition, real-world testing has shown that ISVG systems are highly resilient to environmental challenges, such as fluctuating solar irradiance and biofouling, which are significant obstacles for conventional desalination systems. Collectively, these advantages demonstrate that ISVG technology is a promising, economically viable, and environmentally sustainable solution for addressing the growing global demand for decentralized water purification, making it an attractive option compared to traditional desalination methods.

4 Conclusions and perspectives

4.1 Conclusions

This review has provided a comprehensive analysis of recent advancements in ISVG technology, addressing the critical aspects of fundamental principles, device optimization, and engineering implementation. The key findings are summarized as follows.

Elucidating fundamental principles. A thorough examination of the fundamental physical and chemical processes underpinning ISVG has been presented, focusing on the mechanisms governing vapor generation and condensation. By leveraging established principles of heat transfer, phase change dynamics, and surface chemistry, a detailed understanding of each stage of the ISVG process has been derived. This foundational insight is pivotal for the rational design of devices optimized for enhanced energy efficiency and condensate collection. The interplay of solar energy absorption, thermal management, and vapor transport has been critically analyzed, providing a scientific basis for the development of more efficient and stable ISVG systems.

Optimizing device performance. Building upon the principles established in the previous section, this review has detailed the design considerations that enhance the performance of ISVG systems. Through the integration of advanced

materials, innovative structural configurations, and optimized geometries, significant improvements in solar-to-vapor conversion efficiency have been achieved. The review emphasizes the importance of key design elements such as porous materials, photothermal coatings, and hierarchical structures, which serve to maximize solar absorption and minimize thermal losses. Furthermore, the impact of various design strategies on critical performance metrics, including evaporation rate, energy conversion efficiency, and long-term stability, has been thoroughly assessed, facilitating the translation of theoretical principles into practical, high-performance devices.

Assessing engineering applications. Several case studies have been presented to illustrate the practical implementation of ISVG technology, encompassing applications such as water desalination, waste heat recovery, and industrial cooling. These cases serve to demonstrate the versatility and potential of ISVG systems in addressing critical global challenges. By applying the fundamental principles and device optimization strategies discussed earlier, the functionality and performance of real-world devices have been evaluated in detail. Additionally, the scalability of ISVG systems has been explored, with particular attention given to factors such as material availability, cost-effectiveness, and integration with existing infrastructure. This comprehensive evaluation underscores the importance of aligning theoretical designs with the specific demands of engineering applications to achieve optimal system performance.

In conclusion, the integration of fundamental scientific principles with advanced device design strategies has significantly advanced the field of ISVG technology. These developments hold considerable promise in addressing the pressing global issues of water scarcity and energy efficiency. Future progress in this field will depend on the continued refinement of both the underlying mechanisms and the engineering designs, paving the way for large-scale, practical applications of ISVG systems.

4.2 Perspectives

Looking ahead, the development of ISVG technology must address specific challenges in the areas of long-term operational stability, environmental adaptability, and manufacturing cost reduction. Below are specific, actionable strategies to guide future research and ensure the successful commercialization of ISVG systems.

Improving long-term operational stability. The long-term stability of ISVG systems is critical for their adoption, especially under harsh conditions such as high salinity and polluted water. To ensure sustained performance, the following strategies should be prioritized: (1) development of anti-fouling and corrosion-resistant materials: Researchers should explore advanced coatings and corrosion-resistant materials (*e.g.* high-strength alloy) for structural components to prevent degradation and extend the system's operational lifespan. (2) Regular maintenance and adaptive system design: Research into self-monitoring and adaptive control systems can help predict and address performance declines due to fouling or corrosion. The development of low-cost sensors to monitor the system's

This journal is © The Royal Society of Chemistry 2025

Energy Environ. Sci., 2025, **18**, 6366–6437 | **6429**

performance in real-time (*e.g.*, salt buildup, temperature fluctuations) could provide valuable feedback, enabling automatic adjustments or notifications for maintenance. (3) Optimization of salt collection area: Robust and durable materials were employed, and a precisely designed control system was implemented to prevent unintended salt precipitation in undesired regions, by carefully regulating parameters such as temperature, humidity, and ion concentration to maintain a stable crystallization environment.

Adapting to varying environmental conditions. ISVG systems must be able to perform efficiently across diverse climates, including areas with fluctuating solar radiation, high humidity, and polluted water. To enhance the adaptability of ISVG technology, the following strategies can be implemented: (1) stable multi-energy-coupled evaporation systems. To improve performance in low-solar irradiation conditions (*e.g.*, cloudy days or nighttime), research should focus on integrating wind energy or low-grade waste heat recovery systems to complement solar power. A hybrid system could automatically switch between solar and wind energy depending on availability, ensuring consistent performance under various conditions. (2) Flexible, modular system designs: instead of a one-size-fits-all approach,

ISVG systems should be designed to be modular and customizable based on local environmental conditions. For example, modular evaporators could be deployed in regions with high salinity, while smaller, more compact systems could be tailored to handle wastewater with varying levels of contamination. (3) Adaptive control algorithms: Implementing AI-driven control systems can allow the system to adjust operational parameters (*e.g.*, evaporation rates, temperature, surface image) based on real-time environmental data, optimizing efficiency across varying weather patterns and water qualities. (4) Engineering design for operation stability: Rainproof and dustproof measures for the salt extraction and evaporation unit, as well as vibration-resistant mounting structures to ensure the stability of the desalination module under offshore conditions. (5) Integrated recovery of water and salt: To date, most reported engineering applications have treated freshwater extraction and salt harvesting as separate processes. However, in practical scenarios such as seawater desalination and high-salinity wastewater treatment, there is a concurrent demand for both freshwater and salt. Despite this, no practical system capable of simultaneously recovering both products has been reported. Based on our prior studies and pilot-scale applications, we have identified that the
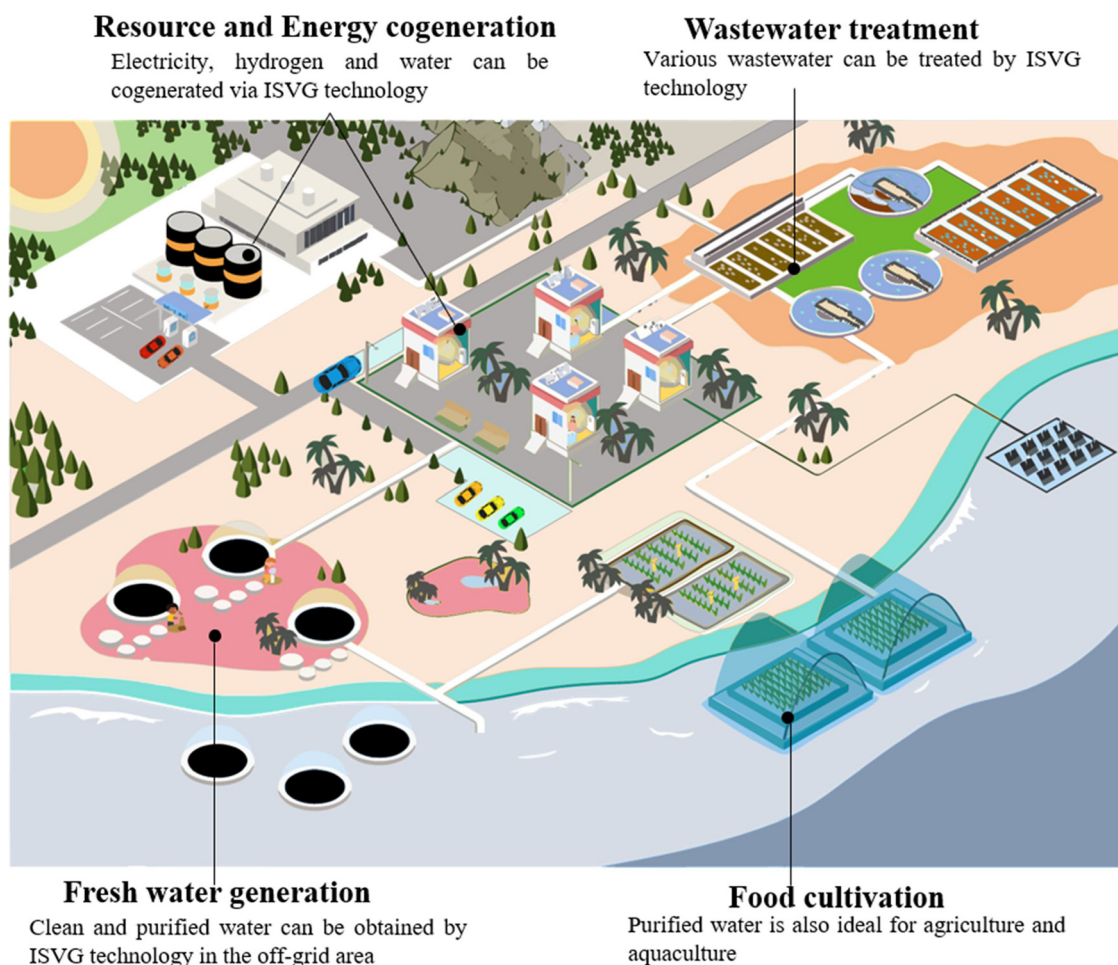

Fig. 38 Application framework of ISVG technology in a comprehensive community.

6430 | *Energy Environ. Sci.*, 2025, **18**, 6366–6437

This journal is © The Royal Society of Chemistry 2025

bottleneck in achieving such dual recovery lies in the limited efficiency at the condensate collection stage. Therefore, enhancing the rate and efficiency of condensate harvesting is critical.

Reducing manufacturing costs to facilitate commercialization. The successful commercialization of ISVG systems requires the development of cost-effective, scalable manufacturing processes. Specific strategies to reduce costs while maintaining high performance include: (1) Cost-efficiency considering: Economic considerations were integrated into the material selection and structural design, with the use of low-cost standardized components and compatibility with automated assembly processes to facilitate large-scale manufacturing. (2) Scalable production techniques: To reduce production costs, scalable manufacturing techniques such as 3D printing, roll-to-roll processing, or spray deposition could be employed for mass production of photothermal materials. These techniques would reduce the reliance on expensive fabrication methods and allow for large-scale production at a fraction of the cost. (3) Simplifying system design: Future research should focus on reducing the complexity of ISVG systems without sacrificing performance. By streamlining components and removing unnecessary parts, the manufacturing process can be made more efficient. For example, minimizing the number of moving parts or using fewer specialized components could reduce both material and labor costs. (4) Accurate identification of application markets and end-user needs: Potential commercial applications include portable seawater desalination units for offshore platforms, islands, and vessels; large-scale salt extraction systems for use in marine and salt-lake mining operations; and high-salinity wastewater treatment systems for the desalination and recycling of water in chemical industries.

In summary, the future of ISVG technology hinges on addressing these concrete challenges through targeted research and innovation. By focusing on improving long-term operational stability, enhancing adaptability to environmental conditions, and reducing manufacturing costs, ISVG systems can become viable, cost-effective solutions for addressing global water scarcity (Fig. 38). These research directions will drive the technological maturation of ISVG, paving the way for its large-scale deployment in desalination, wastewater treatment, and other critical applications.

Data availability

No primary research results, software or code have been included and no new data were generated or analysed as part of this review.

Conflicts of interest

The authors declare no conflicts of interest.

Acknowledgements

References

1 F. Nawaz, Y. Yang, Q. Zhao, Y. Mo, Z. Jiang, J. Wu, Y. Liu, B. Liu, B. Gao and W. Que, *Adv. Energy Mater.*, 2024, **14**, 2400135.

2 M. Li, M. Yang, B. Liu, H. Guo, H. Wang, X. Li, L. Wang and T. D. James, *Chem. Eng. J.*, 2022, **431**, 134245.

3 X. Li, M. Li, Q. Shi, H. Guo, L. Wang, X. Guo, Z. Chen, J. L. Sessler, H. Xiao and T. D. James, *Small*, 2022, **18**, 2201949.

4 M. Li, H. Guo, Y. Xiao, S. Liu, Y. Lu, L. Wang and T. D. James, *Environ. Sci.:Nano*, 2024, **11**, 1271–1282.

5 M. Li, M. Xu, Q. Shi, H. Wang, H. Guo, L. Wang and T. D. James, *Environ. Sci.:Nano*, 2022, **9**, 2559–2571.

6 Y. Xiao, H. Guo, M. Li, J. He, X. Xu, S. Liu, L. Wang and T. D. James, *Coord. Chem. Rev.*, 2025, **527**, 216378.

7 Y. Wei, Y. Yang, Q. Zhao, Y. Ma, M. Qiang, L. Fu, Y. Liu, J. Zhang, Z. Qu and W. Que, *Small*, 2024, **20**, 2312241.

8 H. Hu, J. Wang, Q. Zhao, M. Qiang, Q. Li, L. Guo and Y. Yang, *Desalination*, 2024, **592**, 118129.

9 J. Zhao, Y. Yang, C. Yang, Y. Tian, Y. Han, J. Liu, X. Yin and W. Que, *J. Mater. Chem. A*, 2018, **6**, 16196–16204.

10 M. W. Shahzad, M. Burhan, L. Ang and K. C. Ng, *Desalination*, 2017, **413**, 52–64.

11 Y. Zheng, R. A. C. Gonzalez, K. B. Hatzell and M. C. Hatzell, *Joule*, 2021, **5**, 1971–1986.

12 H. Ghasemi, G. Ni, A. M. Marconnet, J. Loomis, S. Yerci, N. Miljkovic and G. Chen, *Nat. Commun.*, 2014, **5**, 4449.

13 Y. Wang, L. Zhang and P. Wang, *ACS Sustainable Chem. Eng.*, 2016, **4**, 1223–1230.

14 G. Liu, J. Xu and K. Wang, *Nano Energy*, 2017, **41**, 269–284.

15 B. Yu, Y. Zhang, Y. Wang and Z. Zhang, *Adv. Funct. Mater.*, 2023, **33**, 2307533.

16 S. Li, P. Xiao and T. Chen, *Adv. Mater.*, 2024, **36**, 2311453.

17 H.-C. Yang, F. Lu, H.-N. Li, C. Zhang, S. B. Darling and Z.-K. Xu, *Adv. Funct. Mater.*, 2023, **33**, 2304580.

18 X. Li, W. Xie and J. Zhu, *Adv. Sci.*, 2022, **9**, 2104181.

19 J. Wang, X. Cao, X. Cui, H. Wang, H. Zhang, K. Wang, X. Li, Z. Li and Y. Zhou, *Adv. Mater.*, 2024, **36**, 2311151.

20 P. Zhang, H. Wang, J. Wang, Z. Ji and L. Qu, *Adv. Mater.*, 2024, **36**, 2303976.

21 M. Ebrahimian Mashhadi, M. M. Hassan, R. Yang and Q. Lu, *Adv. Funct. Mater.*, 2025, **35**, 2412870.

22 Q. Zhao, Y. Yang, Z. Qiu, M. Qiang, X. Xu, Y. Ma, Y. Liu, B. Liu, C. Sun and W. Que, *Sep. Purif. Technol.*, 2025, **361**, 131249.

23 Q. Zhao, Y. Wei, Y. Yang, M. Qiang, L. Fu, Y. Ma, B. Liu, Y. Liu, X. He and W. Que, *Renewable Energy*, 2025, **244**, 122660.

24 C. Du, X. Zhao, X. Qian, C. Huang and R. Yang, *Nano Energy*, 2023, **107**, 108086.

25 C. Onggowarsito, S. Mao, X. S. Zhang, A. Feng, H. Xu and Q. Fu, *Energy Environ. Sci.*, 2024, **17**, 2088–2099.

26 L. Zhu, L. Tian, S. Jiang, L. Han, Y. Liang, Q. Li and S. Chen, *Chem. Soc. Rev.*, 2023, **52**, 7389–7460.

27 Y. Liu, Y. Yang, B. Liu, Q. Zhao, Y. Shen, M. Qiang, Y. Ma and W. Que, *Desalination*, 2025, **608**, 118854.

28 C. Chen, Y. Kuang and L. Hu, *Joule*, 2019, **3**, 683–718.

29 F. Zhao, Y. Guo, X. Zhou, W. Shi and G. Yu, *Nat. Rev. Mater.*, 2020, **5**, 388–401.

30 D. Wei, C. Wang, J. Zhang, H. Zhao, Y. Asakura, M. Eguchi, X. Xu and Y. Yamauchi, *Adv. Mater.*, 2023, **35**, 2212100.

31 X. Wu, Y. Lu, X. Ren, P. Wu, D. Chu, X. Yang and H. Xu, *Adv. Mater.*, 2024, **36**, 2313090.

32 N. Xu, J. Li, C. Finnerty, Y. Song, L. Zhou, B. Zhu, P. Wang, B. Mi and J. Zhu, *Nat. Water*, 2023, **1**, 494–501.

33 C. Dang, Y. Cao, H. Nie, W. Lang, J. Zhang, G. Xu and M. Zhu, *Nat. Water*, 2024, **2**, 115–126.

34 J. Wang, Y. Kong, Z. Liu and H. Wang, *Nano Energy*, 2023, **108**, 108115.

35 M. S. Irshad, N. Arshad, M. S. Asghar, Y. Hao, M. Alomar, S. Zhang, J. Zhang, J. Guo, I. Ahmed, N. Mushtaq, M. A. K. Y. Shah, L. Noureen, S. Wageh, O. A. Al-Hartomy, A. Kalam, V.-D. Dao, H. Wang, X. Wang and H. Zhang, *Adv. Funct. Mater.*, 2023, **33**, 2304936.

36 Y. Yuan, C. Dong, J. Gu, Q. Liu, J. Xu, C. Zhou, G. Song, W. Chen, L. Yao and D. Zhang, *Adv. Mater.*, 2020, **32**, 1907975.

37 G. Li, L. Wang, X. Ji and X. Zhang, *Adv. Mater.*, 2025, **37**, 2412385.

38 H. Yang, D. Li, X. Zheng, J. Zuo, B. Zhao, D. Li, J. Zhang, Z. Liang, J. Jin, S. Ju, M. Peng, Y. Sun and L. Jiang, *Adv. Mater.*, 2023, **35**, 2304699.

39 C. Dai, Z. Li, K. Zheng, J.-H. Zhang, R. Dai, D. Luo, H. Gao, H. K. Thabet, Z. M. El-Bahy, L. Pan, Y. Mai, Y. Yamauchi and X. Xu, *Nano Energy*, 2024, **131**, 110244.

40 B. Wang, X. Huang, Z. Liu, J. Zhang, C. Wei, B. Cai, P. Xie and A. Zhou, *Energy Environ. Sci.*, 2024, **17**, 7600–7626.

41 Q. Zhao, Y. Yang, C. Pan, B. Zhu, Z. Sha, Y. Wei and W. Que, *Sol. Energy*, 2023, **266**, 112187.

42 Q. Zhao, Y. Yang, B. Zhu, Z. Sha, H. Zhu, Z. Wu, F. Nawaz, Y. Wei, L. Luo and W. Que, *Desalination*, 2023, **568**, 116999.

43 S. Li, Z. Xi, L. Yu, H. Yan and M. Chen, *Langmuir*, 2023, **39**, 8900–8907.

44 Y. Pang, J. Zhang, R. Ma, Z. Qu, E. Lee and T. Luo, *ACS Energy Lett.*, 2020, **5**, 437–456.

45 Y. Wang, X. Wu, P. Wu, J. Zhao, X. Yang, G. Owens and H. Xu, *Sci. Bull.*, 2021, **66**, 2479–2488.

46 Y. Wang, X. Wu, X. Yang, G. Owens and H. Xu, *Nano Energy*, 2020, **78**, 105269.

47 Y. Gao, Q. Sun, Y. Chen, X. Zhou, C. Wei and L. Lyu, *Chem. Eng. J.*, 2023, **455**, 140500.

48 Z. Xu, X. Ran, Z. Zhang, M. Zhong, D. Wang, P. Li and Z. Fan, *Mater. Horiz.*, 2023, **10**, 1737–1744.

49 X. Zhou, F. Zhao, Y. Guo, Y. Zhang and G. Yu, *Energy Environ. Sci.*, 2018, **11**, 1985–1992.

50 R. Zhang, B. Xiang, Y. Wang, S. Tang and X. Meng, *Mater. Horiz.*, 2022, **9**, 1232–1242.

51 Y. Ji, M. Qiang, Q. Zhao, Y. Mo, L. Fu, Z. Lin, H. Yang, Y. Xing, G. Ni and Y. Yang, *Small*, 2024, **20**, 2403606.

52 M. Sheng, Y. Yang, X. Bin, S. Zhao, C. Pan, F. Nawaz and W. Que, *Nano Energy*, 2021, **89**, 106468.

53 F. Nawaz, Y. Yang, S. Zhao, M. Sheng, C. Pan and W. Que, *J. Mater. Chem. A*, 2021, **9**, 16233–16254.

54 P. Wu, X. Wu, Y. Wang, H. Xu and G. Owens, *Water Res.*, 2022, **212**, 118099.

55 H. Zhou, L. Han, M. Yang, X. Wu, J. Li, H. Ma and B. Zhang, *Desalination*, 2023, **556**, 116567.

56 Y. Li, T. Gao, Z. Yang, C. Chen, W. Luo, J. Song, E. Hitz, C. Jia, Y. Zhou, B. Liu, B. Yang and L. Hu, *Adv. Mater.*, 2017, **29**, 1700981.

57 L. Zhang, G. Liu, L. Wu, Z. Chen, Z. Dai, F. Yu and X. Wang, *Chem. Eng. J.*, 2023, **454**, 140298.

58 L. Zhou, Y. Tan, J. Wang, W. Xu, Y. Yuan, W. Cai, S. Zhu and J. Zhu, *Nat. Photonics*, 2016, **10**, 393–398.

59 Y. Zhang, Y. Wang, B. Yu, K. Yin and Z. Zhang, *Adv. Mater.*, 2022, **34**, 2200108.

60 Y. Zhou, Q. Lu, Q. Liu, H. Yang, J. Liu, J. Zhuang, W. Shi and X. Wang, *Adv. Funct. Mater.*, 2022, **32**, 2112159.

61 X. Geng, P. Yang and Y. Wan, *Nano Energy*, 2024, **123**, 109434.

62 A. Caratenuto and Y. Zheng, *Sci. Adv.*, 2024, **10**, eadn6368.

63 Z. Xu, J. Yu, H. Shan, J. Wang, J. Gao, Z. Ye and R. Wang, *Energy Environ. Sci.*, 2023, **16**, 5325–5338.

64 Z. Yang, D. Li, Y. Zhu, X. Zhu, W. Yu, K. Yang and B. Chen, *Environ. Sci. Technol.*, 2024, **58**, 8610–8630.

65 X. Li, G. Ni, T. Cooper, N. Xu, J. Li, L. Zhou, X. Hu, B. Zhu, P. Yao and J. Zhu, *Joule*, 2019, **3**, 1798–1803.

66 J. H. Zhang, R. Mittapally, G. Lv and G. Chen, *Energy Environ. Sci.*, 2025, **18**, 1707–1721.

67 Y. Shi, R. Li, Y. Jin, S. Zhuo, L. Shi, J. Chang, S. Hong, K.-C. Ng and P. Wang, *Joule*, 2018, **2**, 1171–1186.

68 W. Li, Z. Li, K. Bertelsmann and D. E. Fan, *Adv. Mater.*, 2019, **31**, 1900720.

69 H. Wang, C. Zhang, Z. Zhang, B. Zhou, J. Shen and A. Du, *Adv. Funct. Mater.*, 2020, **30**, 2005513.

70 Y. Geng, W. Sun, P. Ying, Y. Zheng, J. Ding, K. Sun, L. Li and M. Li, *Adv. Funct. Mater.*, 2021, **31**, 2007648.

71 Z. Liu, Z. Zhou, N. Wu, R. Zhang, B. Zhu, H. Jin, Y. Zhang, M. Zhu and Z. Chen, *ACS Nano*, 2021, **15**, 13007–13018.

72 G. Ni, G. Li, S. V. Boriskina, H. Li, W. Yang, T. Zhang and G. Chen, *Nat. Energy*, 2016, **1**, 16126.

73 X. Li, R. Lin, G. Ni, N. Xu, X. Hu, B. Zhu, G. Lv, J. Li, S. Zhu and J. Zhu, *Natl. Sci. Rev.*, 2018, **5**, 70–77.

74 T. A. Cooper, S. H. Zandavi, G. W. Ni, Y. Tsurimaki, Y. Huang, S. V. Boriskina and G. Chen, *Nat. Commun.*, 2018, **9**, 5086.

75 X. Wu, Z. Wu, Y. Wang, T. Gao, Q. Li and H. Xu, *Adv. Sci.*, 2021, **8**, 2002501.

76 M. Li, B. Liu, Z. Liu, Y. Xiao, H. Guo, Z. An, L. Wang and T. D. James, *Adv. Funct. Mater.*, 2023, **33**, 2209987.

77 Y. Yang, W. Que, J. Zhao, Y. Han, M. Ju and X. Yin, *Chem. Eng. J.*, 2019, **373**, 955–962.

6432 | *Energy Environ. Sci.*, 2025, **18**, 6366–6437

This journal is © The Royal Society of Chemistry 2025

78 S. C. Singh, M. ElKabbash, Z. Li, X. Li, B. Regmi, M. Madsen, S. A. Jalil, Z. Zhan, J. Zhang and C. Guo, *Nat. Sustain.*, 2020, **3**, 938–946.

79 B. Shao, Y. Wang, X. Wu, Y. Lu, X. Yang, G. Y. Chen, G. Owens and H. Xu, *J. Mater. Chem. A*, 2020, **8**, 11665–11673.

80 Y. Guo, X. Zhao, F. Zhao, Z. Jiao, X. Zhou and G. Yu, *Energy Environ. Sci.*, 2020, **13**, 2087–2095.

81 N. Xu, X. Hu, W. Xu, X. Li, L. Zhou, S. Zhu and J. Zhu, *Adv. Mater.*, 2017, **29**, 1606762.

82 X. Li, W. Xu, M. Tang, L. Zhou, B. Zhu, S. Zhu and J. Zhu, *Proc. Natl. Acad. Sci. U. S. A.*, 2016, **113**, 13953–13958.

83 H. Shan, Z. Ye, J. Yu, R. Wang and Z. Xu, *Device*, 2023, **1**, 100065.

84 S. Liu, C. Huang, Q. Huang, F. Wang and C. Guo, *J. Mater. Chem. A*, 2019, **7**, 17954–17965.

85 H. Liang, Q. Liao, N. Chen, Y. Liang, G. Lv, P. Zhang, B. Lu and L. Qu, *Angew. Chem., Int. Ed.*, 2019, **58**, 19041–19046.

86 Y. Wang, W. Zhao, Y. Lee, Y. Li, Z. Wang and K. C. Tam, *Nat. Commun.*, 2024, **15**, 6157.

87 D. Wei, C. Wang, G. Shi, J. Zhang, F. Wang, P. Tan, Z. Zhao and Y. Xie, *Adv. Mater.*, 2024, **36**, 2309507.

88 G. Parisi, A. Lopez and S. Narayan, *ACS Appl. Eng. Mater.*, 2023, **1**, 408–416.

89 V. Kashyap and H. Ghasemi, *J. Mater. Chem. A*, 2020, **8**, 7035–7065.

90 J. Wang and T. Hou, *J. Chem. Theory Comput.*, 2011, **7**, 2151–2165.

91 C. Jia, Y. Li, Z. Yang, G. Chen, Y. Yao, F. Jiang, Y. Kuang, G. Pastel, H. Xie and B. Yang, *Joule*, 2017, **1**, 588–599.

92 X. Zhou, F. Zhao, Y. Guo, B. Rosenberger and G. Yu, *Sci. Adv.*, 2019, **5**, eaaw5484.

93 Y. Zheng, R. Huang, Y. Yu, X. Wei, J. Yin and S. Zhang, *Water Res.*, 2024, **257**, 121707.

94 L. Hou, S. Li, Y. Qi, J. Liu, Z. Cui, X. Liu, Y. Zhang, N. Wang and Y. Zhao, *ACS Nano*, 2025, **19**, 9636–9683.

95 H. Yu, H. Jin, Y. Liang, D. Wang, Y. Lu, X. Yang and H. Xu, *ACS Energy Lett.*, 2025, **10**, 1192–1215.

96 B. Fu, X. Zhang, N. Robinson, Z. Zhang, J. Zhang, J. Ji, Y. Xu, K. Zhang, M. Dong, J. Kang, L. Zhang, L. Wang, Y. Zou, M. Zhou, S. Chen, H. Yin, H. Xu, P. Liu and H. Zhao, *Nano Energy*, 2024, **129**, 110054.

97 C. Gao, Y. Li, L. Lan, Q. Wang, B. Zhou, Y. Chen, J. Li, J. Guo and J. Mao, *Adv. Sci.*, 2024, **11**, 2306833.

98 J. Jin, C. Wang, D. Wei, B. Wang, X. Lin, W. Zhang, C. Shi, Z. Zhao, L. Wang and F. Wang, *Small*, 2025, **21**, 2411624.

99 M. Wu, Y. Wei, Y. Zhu, Y. Bai, Y. Wang, X. Wang, S.-H. Ho, W. Wang and R. Li, *Adv. Funct. Mater.*, 2024, **34**, 2410729.

100 H. Yu, H. Jin, M. Qiu, Y. Liang, P. Sun, C. Cheng, P. Wu, Y. Wang, X. Wu, D. Chu, M. Zheng, T. Qiu, Y. Lu, B. Zhang, W. Mai, X. Yang, G. Owens and H. Xu, *Adv. Mater.*, 2024, **36**, 2414045.

101 B. Wang, H. Cheng, H. Zhu and L. Qu, *Adv. Funct. Mater.*, 2025, 2500459.

102 Z.-F. Zeng, Y.-Q. Yang, X.-W. Pang, B. Jiang, L.-X. Gong, Z. Liu, L. Peng and S.-N. Li, *Adv. Funct. Mater.*, 2024, **34**, 2409855.

103 F. Lv, J. Miao, Z. Wang, J. Hu and D. Orejon, *Adv. Mater.*, 2025, **37**, 2410290.

104 X. Meng, X. Wang, K. Yin, Y. Jing, L. Gu, Z. Tao, X. Ren, M. Tang, X. Shao, L. Sun, Y. Sun, Y. Dai and Y. Xiong, *Proc. Natl. Acad. Sci. U. S. A.*, 2024, **121**, e2317192121.

105 Z. Cui, J. Wu, C. Zhou, S. Ai, H. Zhou, F. Kang, Q. Huang, L. Kang, Q. Zhang and D. Tian, *Adv. Funct. Mater.*, 2025, 2424565.

106 C. Chen, K. Tian, L. Xiong, Z. Dai, Q. Li, M. Cheng, Q. Fu and H. Deng, *Small*, 2025, **21**, 2411262.

107 H. Zhu, J. Yang, C. Li, Y. Zhong, X. Tian, M. Zhang and W. Huang, *Adv. Mater.*, 2025, 2419243.

108 Y. Qian, G. Xue, L. Chen, G. Xu and G.-E. Wang, *Adv. Mater.*, 2024, **36**, 2310795.

109 L. Liu, H. Liu, Z. Fan, J. Liu, X. Wen, H. Wang, Y. She, G. Hu, R. Niu and J. Gong, *Energy Environ. Mater.*, 2025, **8**, e12812.

110 H. Lu, W. Shi, F. Zhao, W. Zhang, P. Zhang, C. Zhao and G. Yu, *Adv. Funct. Mater.*, 2021, **31**, 2101036.

111 X. Zhou, Y. Guo, F. Zhao and G. Yu, *Acc. Chem. Res.*, 2019, **52**, 3244–3253.

112 L. Zang, L. Sun, S. Zhang, C. Finnerty, A. Kim, J. Ma and B. Mi, *Chem. Eng. J.*, 2021, **422**, 129998.

113 X. Zhou, Y. Guo, F. Zhao, W. Shi and G. Yu, *Adv. Mater.*, 2020, **32**, 2007012.

114 C. Li, S. Cao, J. Lutzki, J. Yang, T. Konegger, F. Kleitz and A. Thomas, *J. Am. Chem. Soc.*, 2022, **144**, 3083–3090.

115 F. Zhao, X. Zhou, Y. Shi, X. Qian, M. Alexander, X. Zhao, S. Mendez, R. Yang, L. Qu and G. Yu, *Nat. Nanotechnol.*, 2018, **13**, 489–495.

116 J. Li, R. Long, B. Zhang, R. Yang, W. Liu and Z. Liu, *J. Phys. Chem. Lett.*, 2020, **11**, 9856–9861.

117 B. Yang, Z. Zhang, P. Liu, X. Fu, J. Wang, Y. Cao, R. Tang, X. Du, W. Chen, S. Li, H. Yan, Z. Li, X. Zhao, G. Qin, X.-Q. Chen and L. Zuo, *Nature*, 2023, **622**, 499–506.

118 Y. Tu, J. Zhou, S. Lin, M. Alshrah, X. Zhao and G. Chen, *Proc. Natl. Acad. Sci. U. S. A.*, 2023, **120**, e2312751120.

119 J. Tang, T. Zheng, Z. Song, Y. Shao, N. Li, K. Jia, Y. Tian, Q. Song, H. Liu and G. Xue, *ACS Appl. Mater. Interfaces*, 2020, **12**, 18504–18511.

120 S. Lei, D. Huang, S. Liu, M. Chen, R. Ma, M. Zeng, D. Li, W. Ma, L. Wang and Z. Cheng, *J. Mater. Chem. A*, 2021, **9**, 15346–15354.

121 Y. Qiu, Z. Zhou, C. Zhang, F. Jiang, Q. Zhang and J. Chen, *ACS Energy Lett.*, 2022, **7**, 3476–3483.

122 J. Li, X. Wang, Z. Lin, N. Xu, X. Li, J. Liang, W. Zhao, R. Lin, B. Zhu, G. Liu, L. Zhou, S. Zhu and J. Zhu, *Joule*, 2020, **4**, 928–937.

123 H. Liu, B. Chen, Y. Chen, M. Zhou, F. Tian, Y. Li, J. Jiang and W. Zhai, *Adv. Mater.*, 2023, **35**, 2301596.

124 P. Xiao, J. Gu, C. Zhang, F. Ni, Y. Liang, J. He, L. Zhang, J. Ouyang, S.-W. Kuo and T. Chen, *Nano Energy*, 2019, **65**, 104002.

125 Y. Wang, X. Wu, T. Gao, Y. Lu, X. Yang, G. Y. Chen, G. Owens and H. Xu, *Nano Energy*, 2021, **79**, 105477.

126 Z. Zhang, W. Xu, J. Wang, M. Hu, D. Zhang, L. Jia, A. Kang, Y. Xi, X. Ye, S. Cheng, E. Sun, Y. Chen, Z. Wang, H. Lin and Q. Xiao, *ACS Energy Lett.*, 2023, **8**, 2276–2283.

This journal is © The Royal Society of Chemistry 2025

Energy Environ. Sci., 2025, **18**, 6366–6437 | **6433**

127 Y. Li, X. Liu, W. Hong, X. Chen and H. Li, *Int. J. Heat Mass Transfer*, 2023, **208**, 124082.

128 J. Lan, H. Li, X. Liu, S. Wang and W. Hong, *Int. J. Heat Mass Transfer*, 2023, **216**, 124506.

129 H. Xie, W. H. Xu, Y. Du, J. Gong, R. Niu, T. Wu and J. P. Qu, *Small*, 2022, **18**, 2200175.

130 C. Zhao, H. Sun, J. Wang and H. Yang, *Appl. Therm. Eng.*, 2024, **240**, 122140.

131 J. B. Boreyko and C.-H. Chen, *Phys. Rev. Lett.*, 2009, **103**, 184501.

132 C. Dang, H. Wang, Y. Cao, J. Shen, J. Zhang, L. Lv, G. Xu and M. Zhu, *Energy Environ. Sci.*, 2022, **15**, 5405–5414.

133 F. Wang, C. Wang, G. Shi, Y. Wang, F. Li, K. Xu and M. Ma, *Desalination*, 2023, **545**, 116157.

134 B. Zhu, H. Kou, Z. Liu, Z. Wang, D. K. Macharia, M. Zhu, B. Wu, X. Liu and Z. Chen, *ACS Appl. Mater. Interfaces*, 2019, **11**, 35005–35014.

135 H. Ren, M. Tang, B. Guan, K. Wang, J. Yang, F. Wang, M. Wang, J. Shan, Z. Chen, D. Wei, H. Peng and Z. Liu, *Adv. Mater.*, 2017, **29**, 1702590.

136 C. Finnerty, L. Zhang, D. L. Sedlak, K. L. Nelson and B. Mi, *Environ. Sci. Technol.*, 2017, **51**, 11701–11709.

137 J. W. Gibbs, *Am. J. Sci.*, 1878, **3**, 441–458.

138 Y. Yang, H. Zhao, Z. Yin, J. Zhao, J. Yin, N. Li, D. Yin, Y. Li, B. Lei, Y. Du and W. Que, *Mater. Horiz.*, 2018, **5**, 1143–1150.

139 W. Xu, X. Hu, S. Zhuang, Y. Wang, X. Li, L. Zhou, S. Zhu and J. Zhu, *Adv. Energy Mater.*, 2018, **8**, 1702884.

140 X. Chen, S. He, M. M. Falinski, Y. Wang, T. Li, S. Zheng, D. Sun, J. Dai, Y. Bian and X. Zhu, *Energy Environ. Sci.*, 2021, **14**, 5347–5357.

141 L. Hou, N. Wang, L.-J. Yu, J. Liu, S. Zhang, Z. Cui, S. Li, H. Li, X. Liu, L. Jiang and Y. Zhao, *ACS Energy Lett.*, 2023, **8**, 553–564.

142 J. Zeng, Q. Wang, Y. Shi, P. Liu and R. Chen, *Adv. Energy Mater.*, 2019, **9**, 1900552.

143 W. Zhao, H. Gong, Y. Song, B. Li, N. Xu, X. Min, G. Liu, B. Zhu, L. Zhou, X.-X. Zhang and J. Zhu, *Adv. Funct. Mater.*, 2021, **31**, 2100025.

144 C. Lei, W. Guan, Y. Guo, W. Shi, Y. Wang, K. P. Johnston and G. Yu, *Angew. Chem., Int. Ed.*, 2022, **61**, e202208487.

145 Q. Xue, P. Xiao, J. Gu, W. Wang, L. Yan and T. Chen, *Water Res.*, 2024, **253**, 121290.

146 Y. Kuang, C. Chen, S. He, E. M. Hitz, Y. Wang, W. Gan, R. Mi and L. Hu, *Adv. Mater.*, 2019, **31**, 1900498.

147 K. Yang, T. Pan, S. Dang, Q. Gan and Y. Han, *Nat. Commun.*, 2022, **13**, 6653.

148 X. Liu, F. Chen, Y. Li, H. Jiang, D. D. Mishra, F. Yu, Z. Chen, C. Hu, Y. Chen, L. Qu and W. Zheng, *Adv. Mater.*, 2022, **34**, 2203137.

149 C. Wang, K. Xu, G. Shi and D. Wei, *Adv. Energy Mater.*, 2023, **13**, 2300134.

150 N. He, Y. Yang, H. Wang, F. Li, B. Jiang, D. Tang and L. Li, *Adv. Mater.*, 2023, **35**, 2300189.

151 Y. Yang, H. Feng, W. Que, Y. Qiu, Y. Li, L. Guo and Q. Li, *Adv. Funct. Mater.*, 2023, **33**, 2210972.

152 D. Fan, Y. Lu, H. Zhang, H. Xu, C. Lu, Y. Tang and X. Yang, *Appl. Catal., B*, 2021, **295**, 120285.

153 J. Wang, M. Sun, C. Liu, Y. Ye, M. Chen, Z. Zhao, Y. Zhang, X. Wu, K. Wang and Y. Zhou, *Adv. Mater.*, 2023, **35**, 2306103.

154 Y. Guo, C. M. Dundas, X. Zhou, K. P. Johnston and G. Yu, *Adv. Mater.*, 2021, **33**, 2102994.

155 H. Xing, Y. Song, H. Xu, S. Chen, K. Li, L. Dong, B. Wang, J. Xue and Y. Lu, *Small*, 2023, **19**, 2206189.

156 A. M. Saleque, M. N. A. S. Ivan, S. Ahmed and Y. H. Tsang, *Chem. Eng. J.*, 2023, **458**, 141430.

157 B. Jin, Y. Lu, X. Zhang, X. Zhang, D. Li, Q. Liu, B. Deng and H. Li, *Chem. Eng. J.*, 2023, **469**, 143906.

158 L. Huang, H. Jiang, Y. Wang, Z. Ouyang, W. Wang, B. Yang, H. Liu and X. Hu, *Desalination*, 2020, **477**, 114260.

159 E. Chiavazzo, M. Morciano, F. Viglino, M. Fasano and P. Asinari, *Nat. Sustain.*, 2018, **1**, 763–772.

160 Q. Xia, Z. Deng, S. Sun, W. Zhao, J. Ding, B. Xi, G. Gao and C. Wang, *Proc. Natl. Acad. Sci. U. S. A.*, 2024, **121**, e2400159121.

161 X. Chen, W. Yu, Y. Zhang, C. Huang, L. Nie, J. Yu, Y. Zhang, C. Zhang, W. Zhai, X. Zhang, Y. Yu and W. Liu, *Adv. Funct. Mater.*, 2024, **34**, 2316178.

162 P. Yang, K. Liu, Q. Chen, J. Li, J. Duan, G. Xue, Z. Xu, W. Xie and J. Zhou, *Energy Environ. Sci.*, 2017, **10**, 1923–1927.

163 L. Zhu, T. Ding, M. Gao, C. K. N. Peh and G. W. Ho, *Adv. Energy Mater.*, 2019, **9**, 1900250.

164 X. Li, X. Min, J. Li, N. Xu, P. Zhu, B. Zhu, S. Zhu and J. Zhu, *Joule*, 2018, **2**, 2477–2484.

165 W. Li, J. Li, L. Ding, X. Zhu, R. Sun and K. Chang, *Adv. Funct. Mater.*, 2024, **34**, 2411387.

166 W. Ma, T. Lu, W. Cao, R. Xiong and C. Huang, *Adv. Funct. Mater.*, 2023, **33**, 2214157.

167 P. Poredoš, J. Gao, H. Shan, J. Yu, Z. Shao, Z. Xu and R. Wang, *Nat. Commun.*, 2024, **15**, 7890.

168 G. Fan, C. Cai, Z. Chen, J. Luo, B. Du, S. Yang and J. Wu, *J. Hazard. Mater.*, 2023, **441**, 129932.

169 M. Wang, J. Chen, Y. Wei, L. Hu, Y. Xu, Y. Liu and R. Wang, *J. Hazard. Mater.*, 2024, **465**, 133273.

170 X. Cao, G. Fan, J. Luo, L. Zhang, S. Wu, Y. Yao and K.-Q. Xu, *J. Hazard. Mater.*, 2024, **478**, 135461.

171 F. Dong, P. Zhang, J. Cheng, J. Chen, T. Liu, X. Ma, S. Song and S. Nie, *Nano Energy*, 2023, **118**, 108977.

172 M. Kong, E. A. Passa, T. Sanan, A. N. Mohammed, A. L. B. Förster, P. T. Justen, A. de la Cruz, J. A. Westrick, K. O'Shea, B. Ren, M. N. Nadagouda, J. S. Yadav, X. Duan, S. D. Richardson and D. D. Dionysiou, *Environ. Sci. Technol.*, 2025, **59**, 1421–1433.

173 W. Xu, Y. Xing, J. Liu, H. Wu, Y. Cui, D. Li, D. Guo, C. Li, A. Liu and H. Bai, *ACS Nano*, 2019, **13**, 7930–7938.

174 Y. Gu, X. Mu, P. Wang, X. Wang, J. Liu, J. Shi, A. Wei, Y. Tian, G. Zhu, H. Xu, J. Zhou and L. Miao, *Nano Energy*, 2020, **74**, 104857.

175 X. Zhao, L.-M. Peng, C.-Y. Tang, J.-H. Pu, X.-J. Zha, K. Ke, R.-Y. Bao, M.-B. Yang and W. Yang, *Mater. Horiz.*, 2020, **7**, 855–865.

176 J. Su, Y. Xie, P. Zhang, R. Yang, B. Wang, H. Zhao, Y. Xu, X. Lin, J. Shi and C. Wang, *Desalination*, 2023, **566**, 116905.

177 H. Xu, H. Xing, S. Chen, Q. Wang, L. Dong, K.-D. Hu, B. Wang, J. Xue and Y. Lu, *Nanoscale*, 2022, **14**, 7493–7501.

178 W. Deng, T. Fan and Y. Li, *Nano Energy*, 2022, **92**, 106745.

179 J. Xu, Z. Wang, C. Chang, B. Fu, P. Tao, C. Song, W. Shang and T. Deng, *Desalination*, 2020, **484**, 114423.

180 H. Bai, N. Liu, L. Hao, P. He, C. Ma, R. Niu, J. Gong and T. Tang, *Energy Environ. Mater.*, 2022, **5**, 1204–1213.

181 B. Gong, H. Yang, S. Wu, G. Xiong, J. Yan, K. Cen, Z. Bo and K. Ostrikov, *Nano-Micro Lett.*, 2019, **11**, 51.

182 H. Yao, P. Zhang, C. Yang, Q. Liao, X. Hao, Y. Huang, M. Zhang, X. Wang, T. Lin and H. Cheng, *Energy Environ. Sci.*, 2021, **14**, 5330–5338.

183 F. Wang, N. Xu, W. Zhao, L. Zhou, P. Zhu, X. Wang, B. Zhu and J. Zhu, *Joule*, 2021, **5**, 1602–1612.

184 G. Xue, Q. Chen, S. Lin, J. Duan, P. Yang, K. Liu, J. Li and J. Zhou, *Glob. Chall.*, 2018, **2**, 1800001.

185 Z. Xu, L. Zhang, L. Zhao, B. Li, B. Bhatia, C. Wang, K. L. Wilke, Y. Song, O. Labban and J. H. Lienhard, *Energy Environ. Sci.*, 2020, **13**, 830–839.

186 W. Wang, Y. Shi, C. Zhang, S. Hong, L. Shi, J. Chang, R. Li, Y. Jin, C. Ong, S. Zhuo and P. Wang, *Nat. Commun.*, 2019, **10**, 3012.

187 Z. Zhu, H. Zheng, H. Kong, X. Ma and J. Xiong, *Nat. Water*, 2023, **1**, 790–799.

188 J. Gao, L. Zhang, J. You, Z. Ye, Y. Zhong, R. Wang, E. N. Wang and Z. Xu, *Joule*, 2023, **7**, 2274–2290.

189 L. Zhang, Z. Xu, B. Bhatia, B. Li, L. Zhao and E. N. Wang, *Appl. Energy*, 2020, **266**, 114864.

190 Y. Xu, B. Lv, Y. Yang, X. Fan, Y. Yu, C. Song and Y. Liu, *Desalination*, 2021, **517**, 115260.

191 Y. Guo, H. Lu, F. Zhao, X. Zhou, W. Shi and G. Yu, *Adv. Mater.*, 2020, **32**, 1907061.

192 H. Geng, Q. Xu, M. Wu, H. Ma, P. Zhang, T. Gao, L. Qu, T. Ma and C. Li, *Nat. Commun.*, 2019, **10**, 1512.

193 M. Li, B. Liu, H. Guo, H. Wang, Q. Shi, M. Xu, M. Yang, X. Luo and L. Wang, *Environ. Sci. Technol.*, 2022, **56**, 11718–11728.

194 X. Hao, H. Yao, P. Zhang, Q. Liao, K. Zhu, J. Chang, H. Cheng, J. Yuan and L. Qu, *Nat. Water*, 2023, **1**, 982–991.

195 X. Wang, Z. Lin, J. Gao, Z. Xu, X. Li, N. Xu, J. Li, Y. Song, H. Fu, W. Zhao, S. Wang, B. Zhu, R. Wang and J. Zhu, *Nat. Water*, 2023, **1**, 391–398.

196 L. Shi, Y. Shi, S. Zhuo, C. Zhang, Y. Aldrees, S. Aleid and P. Wang, *Nano Energy*, 2019, **60**, 222–230.

197 C. Song, D. Qi, Y. Han, Y. Xu, H. Xu, S. You, W. Wang, C. Wang, Y. Wei and J. Ma, *Environ. Sci. Technol.*, 2020, **54**, 9025–9033.

198 D. Qi, Y. Liu, Y. Liu, Z. Liu, Y. Luo, H. Xu, X. Zhou, J. Zhang, H. Yang, W. Wang and X. Chen, *Adv. Mater.*, 2020, **32**, 2004401.

199 W. Cho, D. Lee, G. Choi, J. Kim, A. E. Kojo and C. Park, *Adv. Mater.*, 2022, **34**, 2206982.

200 P. Zhang, F. Zhao, W. Shi, H. Lu, X. Zhou, Y. Guo and G. Yu, *Adv. Mater.*, 2022, **34**, 2110548.

201 D. Xie, M. He, X. Li, J. Sun, J. Luo, Y. Wu and F. Cheng, *Nano Energy*, 2022, **93**, 106802.

202 S. Zhou, R. He, J. Pei, W. Liu, Z. Huang, X. Liu and J. Wang, *Environ. Sci. Technol.*, 2022, **56**, 10474–10482.

203 Y. Song, N. Xu, G. Liu, H. Qi, W. Zhao, B. Zhu, L. Zhou and J. Zhu, *Nat. Nanotechnol.*, 2022, **17**, 857–863.

204 T. Li, T. Yan, P. Wang, J. Xu, X. Huo, Z. Bai, W. Shi, G. Yu and R. Wang, *Nat. Water*, 2023, **1**, 971–981.

205 H. Zhou, L. Yan, D. Tang, T. Xu, L. Dai, C. Li, W. Chen and C. Si, *Adv. Mater.*, 2024, **36**, 2403876.

206 M. Zou, Y. Zhang, Z. Cai, C. Li, Z. Sun, C. Yu, Z. Dong, L. Wu and Y. Song, *Adv. Mater.*, 2021, **33**, 2102443.

207 S. Guo, Y. Zhang, H. Qu, M. Li, S. Zhang, J. Yang, X. Zhang and S. C. Tan, *EcoMat*, 2022, **4**, e12179.

208 D. Zhao, M. Ding, T. Lin, Z. Duan, R. Wei, P. Feng, J. Yu, C.-Y. Liu and C. Li, *Adv. Sci.*, 2024, **11**, 2400310.

209 P. Wu, X. Wu, H. Yu, J. Zhao, Y. Wang, K. Pi, G. Owens and H. Xu, *Chem. Eng. J.*, 2023, **473**, 145452.

210 Y. Bian, Y. Teng, S. Chen, K. Tang, L. Zhao, L. Fu and S. Gu, *Environ. Sci. Technol.*, 2023, **57**, 21104–21112.

211 O. Neumann, C. Feronti, A. D. Neumann, A. Dong, K. Schell, B. Lu, E. Kim, M. Quinn, S. Thompson, N. Grady, P. Nordlander, M. Oden and N. J. Halas, *Proc. Natl. Acad. Sci. U. S. A.*, 2013, **110**, 11677–11681.

212 Y. Zhang, D. Zhao, F. Yu, C. Yang, J. Lou, Y. Liu, Y. Chen, Z. Wang, P. Tao, W. Shang, J. Wu, C. Song and T. Deng, *Nanoscale*, 2017, **9**, 19384–19389.

213 J. Li, M. Du, G. Lv, L. Zhou, X. Li, L. Bertoluzzi, C. Liu, S. Zhu and J. Zhu, *Adv. Mater.*, 2018, **30**, 1805159.

214 L. Zhao, B. Bhatia, L. Zhang, E. Strobach, A. Leroy, M. K. Yadav, S. Yang, T. A. Cooper, L. A. Weinstein and A. Modi, *Joule*, 2020, **4**, 2733–2745.

215 A. M. Saleque, S. Ahmed, M. N. A. S. Ivan, M. I. Hossain, W. Qarony, P. K. Cheng, J. Qiao, Z. L. Guo, L. Zeng and Y. H. Tsang, *Nano Energy*, 2022, **94**, 106916.

216 X. Guan, P. Kumar, Z. Li, T. K. A. Tran, S. Chahal, Z. Lei, C.-Y. Huang, C.-H. Lin, J.-K. Huang, L. Hu, Y.-C. Chang, L. Wang, J. S. J. Britto, L. Panneerselvan, D. Chu, T. Wu, A. Karakoti, J. Yi and A. Vinu, *Adv. Sci.*, 2023, **10**, 2205809.

217 A. Cheskidov and X. Luo, *Invent. Math.*, 2022, **229**, 987–1054.

218 R. R. Meo, M. Provenzano and M. Morciano, *Int. Commun. Heat Mass Transfer*, 2023, **148**, 106998.

219 X. Liu, F. Chen, Y. Li, H. Jiang, D. D. Mishra, F. Yu, Z. Chen, C. Hu, Y. Chen, L. Qu and W. Zheng, *Adv. Mater.*, 2022, **34**, e2203137.

220 L. Wu, Z. Dong, Z. Cai, T. Ganapathy, N. X. Fang, C. Li, C. Yu, Y. Zhang and Y. Song, *Nat. Commun.*, 2020, **11**, 521.

221 Z. Huang, J. Wei, Y. Wan, P. Li, J. Yu, J. Dong, S. Wang, S. Li and C.-S. Lee, *Small*, 2021, **17**, 2101487.

222 Y. Xia, Q. Hou, H. Jubaer, Y. Li, Y. Kang, S. Yuan, H. Liu, M. W. Woo, L. Zhang and L. Gao, *Energy Environ. Sci.*, 2019, **12**, 1840–1847.

223 C. Zhang, Y. Shi, L. Shi, H. Li, R. Li, S. Hong, S. Zhuo, T. Zhang and P. Wang, *Nat. Commun.*, 2021, **12**, 998.

224 Z. Wang, J. Gao, J. Zhou, J. Gong, L. Shang, H. Ye, F. He, S. Peng, Z. Lin, Y. Li and F. Caruso, *Adv. Mater.*, 2023, **35**, 2209015.

225 X. Ma, X. Jia, G. Yao and D. Wen, *ACS Sustainable Chem. Eng.*, 2022, **10**, 12843–12851.

226 H. Peng, D. Wang and S. Fu, *ACS Appl. Mater. Interfaces*, 2021, **13**, 38405–38415.

This journal is © The Royal Society of Chemistry 2025

Energy Environ. Sci., 2025, **18**, 6366–6437 | **6435**

227 Y. Li, R. Wang, L. Zhang, X. Wang, K. Zhang, W. Shou and J. Fan, *Adv. Funct. Mater.*, 2024, **34**, 2312613.

228 C. Zhang, Y. Shi, L. Shi, H. Li, R. Li, S. Hong, S. Zhuo, T. Zhang and P. Wang, *Nat. Commun.*, 2021, **12**, 998.

229 H.-N. Li, C. Zhang, J.-H. Xin, Y.-W. Liu, H.-C. Yang, C.-Y. Zhu, C. Liu and Z.-K. Xu, *ACS Nano*, 2024, **18**, 2434–2445.

230 K. Chen, L. Li, B. Li, Y. Yang, K. Zhu and J. Zhang, *Adv. Funct. Mater.*, 2024, **34**, 2402221.

231 X. Chen, M. Yang, S. Zheng, F. Temprano-Coleto, Q. Dong, G. Cheng, N. Yao, H. A. Stone, L. Hu and Z. J. Ren, *Nat. Water*, 2023, **1**, 808–817.

232 S. Zhang, X. Wei, X. Cao, M. Peng, M. Wang, L. Jiang and J. Jin, *Nat. Commun.*, 2024, **15**, 238.

233 Y. Song, S. Fang, N. Xu, M. Wang, S. Chen, J. Chen, B. Mi and J. Zhu, *Science*, 2024, **385**, 1444–1449.

234 N. Wang, X. Zhao, J. Wang, B. Yan, S. Wen, J. Zhang, K. Lin, H. Wang, T. Liu, Z. Liu, C. Ma, J. Li and Y. Yuan, *Adv. Sci.*, 2021, **8**, 2102250.

235 T. Li, X. Lin, Z. Zhang, L. Yang, Y. Qian, L. Fu, S. Zhou, W. Chen, Q. Wang, X. Li, X.-Y. Kong, H. Xiao, L. Jiang and L. Wen, *Adv. Funct. Mater.*, 2023, **33**, 2212819.

236 H. Liang, Y. Mu, M. Yin, P.-P. He and W. Guo, *Sci. Adv.*, 2023, **9**, eadj1677.

237 T. Ding and G. W. Ho, *Joule*, 2021, **5**, 1639–1641.

238 T. Ding, Y. Zhou, W. L. Ong and G. W. Ho, *Mater. Today*, 2021, **42**, 178–191.

239 T. Ding, K. Liu, J. Li, G. Xue, Q. Chen, L. Huang, B. Hu and J. Zhou, *Adv. Funct. Mater.*, 2017, **27**, 1700551.

240 C. Shao, J. Gao, T. Xu, B. Ji, Y. Xiao, C. Gao, Y. Zhao and L. Qu, *Nano Energy*, 2018, **53**, 698–705.

241 X. Li, K. Zhang, A. Nilghaz, G. Chen and J. Tian, *Nano Energy*, 2023, **112**, 108491.

242 Y. Qin, Y. Wang, X. Sun, Y. Li, H. Xu, Y. Tan, Y. Li, T. Song and B. Sun, *Angew. Chem., Int. Ed.*, 2020, **59**, 10619–10625.

243 T. Xu, X. Ding, C. Shao, L. Song, T. Lin, X. Gao, J. Xue, Z. Zhang and L. Qu, *Small*, 2018, **14**, 1704473.

244 L. Li, M. Hao, X. Yang, F. Sun, Y. Bai, H. Ding, S. Wang and T. Zhang, *Nano Energy*, 2020, **72**, 104663.

245 Q. Ma, Q. He, P. Yin, H. Cheng, X. Cui, Q. Yun and H. Zhang, *Adv. Mater.*, 2020, **32**, 2003720.

246 Z. Sun, L. Feng, C. Xiong, X. He, L. Wang, X. Qin and J. Yu, *J. Mater. Chem. A*, 2021, **9**, 7085–7093.

247 M. Li, L. Zong, W. Yang, X. Li, J. You, X. Wu, Z. Li and C. Li, *Adv. Funct. Mater.*, 2019, **29**, 1901798.

248 G. Ren, Q. Hu, J. Ye, X. Liu, S. Zhou and Z. He, *Chem. Eng. J.*, 2022, **441**, 135921.

249 T. G. Yun, J. Bae, H. G. Nam, D. Kim, K. R. Yoon, S. M. Han and I.-D. Kim, *Nano Energy*, 2022, **94**, 106946.

250 S. Yang, X. Tao, W. Chen, J. Mao, H. Luo, S. Lin, L. Zhang and J. Hao, *Adv. Mater.*, 2022, **34**, 2200693.

251 Y. Huang, H. Cheng, C. Yang, H. Yao, C. Li and L. Qu, *Energy Environ. Sci.*, 2019, **12**, 1848–1856.

252 H. Wang, T. He, X. Hao, Y. Huang, H. Yao, F. Liu, H. Cheng and L. Qu, *Nat. Commun.*, 2022, **13**, 2524.

253 J. Bai, Y. Hu, T. Guang, K. Zhu, H. Wang, H. Cheng, F. Liu and L. Qu, *Energy Environ. Sci.*, 2022, **15**, 3086–3096.

254 G. Xue, Y. Xu, T. Ding, J. Li, J. Yin, W. Fei, Y. Cao, J. Yu, L. Yuan, L. Gong, J. Chen, S. Deng, J. Zhou and W. Guo, *Nat. Nanotechnol.*, 2017, **12**, 317–321.

255 L. Li, S. Feng, L. Du, Y. Wang, C. Ge, X. Yang, Y. Wu, M. Liu, S. Wang, Y. Bai, F. Sun and T. Zhang, *Nano Energy*, 2022, **99**, 107356.

256 Y. Chen, J. He, C. Ye and S. Tang, *Adv. Energy Mater.*, 2024, **14**, 2400529.

257 Q. Hu, X. Lin, G. Ren, J. Lü, W. Wang, D. Zhang and S. Zhou, *Nat. Water*, 2024, **2**, 988–998.

258 D. C. Grahame, *Chem. Rev.*, 1947, **41**, 441–501.

259 H. Daiguji, P. Yang, A. J. Szeri and A. Majumdar, *Nano Lett.*, 2004, **4**, 2315–2321.

260 F. H. J. van der Heyden, D. Stein and C. Dekker, *Phys. Rev. Lett.*, 2005, **95**, 116104.

261 M.-S. Chun, M. S. Shim and N. W. Choi, *Lab Chip*, 2006, **6**, 302–309.

262 S. Alkafeef, R. J. Gochin and A. L. Smith, *Colloids Surf., A*, 2001, **195**, 77–80.

263 Y. Jun, L. Fuzhi, W. K. Larry and Y. K. Daniel, *J. Micromech. Microeng.*, 2003, **13**, 963.

264 F. H. J. van der Heyden, D. J. Bonthuis, D. Stein, C. Meyer and C. Dekker, *Nano Lett.*, 2007, **7**, 1022–1025.

265 Q.-Y. Wu, C. Wang, R. Wang, C. Chen, J. Gao, J. Dai, D. Liu, Z. Lin and L. Hu, *Adv. Energy Mater.*, 2020, **10**, 1902590.

266 H. Wang, W. Xie, B. Yu, B. Qi, R. Liu, X. Zhuang, S. Liu, P. Liu, J. Duan and J. Zhou, *Adv. Energy Mater.*, 2021, **11**, 2100481.

267 J. Long, J. Yin, F. Yang, G. Zhou, H.-M. Cheng, W. Guo and L. Qiu, *Adv. Energy Mater.*, 2025, **15**, 2303476.

268 M. Wang, Y. Wei, X. Wang, R. Li, S. Zhang, K. Wang, R. Wang, H. Chang, C. Wang, N. Ren and S.-H. Ho, *Nat. Water*, 2023, **1**, 716–724.

269 N. He, H. Wang, H. Zhang, B. Jiang, D. Tang and L. Li, *Nano-Micro Lett.*, 2023, **16**, 8.

270 L. Li, C. Xue, Q. Chang, X. Ren, N. Li, J. Yang, S. Hu and H. Xu, *Adv. Mater.*, 2024, **36**, 2401171.

271 R. Li, Y. Shi, M. Wu, S. Hong and P. Wang, *Nat. Sustainable*, 2020, **3**, 636–643.

272 W. Wang, S. Aleid, Y. Shi, C. Zhang, R. Li, M. Wu, S. Zhuo and P. Wang, *Joule*, 2021, **5**, 1873–1887.

273 L. Zeng, D. Deng, L. Zhu, Z. Zhang, X. Gu, H. Wang and Y. Jiang, *Nano Energy*, 2024, **125**, 109531.

274 Z. Mao, Y. Yao, J. Shen, J. Liu, Y. Chen, B. Zhou, Y. Chen, Q. Wang and J. Lu, *Nat. Water*, 2024, **2**, 93–100.

275 J. Zhao, X. Wu, H. Yu, Y. Wang, P. Wu, X. Yang, D. Chu, G. Owens and H. Xu, *EcoMat*, 2023, **5**, e12302.

276 M. Jiang, Q. Shen, J. Zhang, S. An, S. Ma, P. Tao, C. Song, B. Fu, J. Wang, T. Deng and W. Shang, *Adv. Funct. Mater.*, 2020, **30**, 1910481.

277 H. Yang, Z. Hu, S. Wu, J. Yan, K. Cen, Z. Bo and G. Xiong, *Adv. Energy Mater.*, 2024, **14**, 2402926.

278 R. Niu, J. Ren, J. J. Koh, L. Chen, J. Gong, J. Qu, X. Xu, J. Azadmanjiri and J. Min, *Adv. Energy Mater.*, 2023, **13**, 2302451.

279 F. Wu, C. Hu, Z. Zhu, J. Zheng, Z. Huang and B. Liu, *J. Colloid Interface Sci.*, 2025, **678**, 720–731.

6436 | *Energy Environ. Sci.*, 2025, **18**, 6366–6437

This journal is © The Royal Society of Chemistry 2025

280 Z. Fu, D. Zhong, S. Zhou, L. Zhang, W. Long, J. Zhang, X. Wang, J. Xu, J. Qin, J. Gong, L. Li, L. Xia, B. Yu and W. Xu, *Adv. Sci.*, 2024, **11**, 2406474.

281 B. Yu, J. Duan, J. Li, W. Xie, H. Jin, R. Liu, H. Wang, L. Huang, B. Hu and J. Zhou, *Research*, 2019, **2019**, 2460953.

282 Y. Zheng and K. B. Hatzell, *Desalination*, 2020, **474**, 114168.

283 Y. Zheng, R. A. Caceres Gonzalez, K. B. Hatzell and M. C. Hatzell, *Joule*, 2021, **5**, 1971–1986.

284 Y. Chen, L. Shen, Z. Qi, Z. Luo, X. Li and H. Bao, *Nat. Sustain.*, 2025, **8**, 162–169.

This journal is © The Royal Society of Chemistry 2025

Energy Environ. Sci., 2025, **18**, 6366–6437 | **6437**